Developments and Applications of Synchrotron Radiation Computed Laminography with Micrometer and Nanometer resolution

Zur Erlangung des akademischen Grades Eines

DOKTORS DER NATURWISSENSCHAFTEN

von der Fakultät Physik des

Karlsruher Instituts für Technologie (KIT)

genehmigte

DISSERTATION

von

MSc. Feng Xu

aus Jiangsu China

Content

1 Introduction

From sketch to photograph, human beings have been interested in capturing images of ideas and existences. Being developed throughout the human history, **imaging**, as one of the fundamental tools in modern science and technology, makes use of numerous probes, from ultrasound to electrons, from magnetic fields to X-rays. Among them, X-ray imaging has achieved significant progress and yet develops with high speed.

X-rays are electromagnetic radiation with wavelength between 0.01 and 10 nm. X-rays have been employed, with great success in various research fields, for scattering[1–3], diffraction[4], spectroscopy[5,6], imaging and more. This thesis focuses on X-ray imaging.

In fact, X-ray imaging was promptly put to application for medical examinations after its discovery in 1895[7]. A classic form of X-ray imaging is radiography using X-rays generated by X-ray tubes. The X-rays pass through the object in question. The transmitted beam containing the information of the object is recorded by photographic plates, photographic films, or rare earth screens. Radiography is a two dimensional (2D) imaging method. Since the 1970s, thanks to the availability of computers, three dimensional (3D) imaging, *i.e.* tomography became one of the pillars in X-ray imaging[8].

Nevertheless, it is not until the 1980s with the advent of digital detectors and computing technology that X-ray imaging got fast development. Nowadays, both scintillating digital detectors[9–12] and direct photon counting detectors[13–16] are hot research topics in many research groups around the world. Detector technology is undoubtedly one of the key elements in X-ray imaging.

The X-ray source is another point of rapid development. Conventional X-ray imaging is done with laboratory based X-ray tubes. X-ray tubes offer a broad spectrum and facilitate both 2D and 3D imaging techniques. One of the benefits of these types of sources is their relatively low cost, which has made them abundant in medical, materials testing and security applications. In the scientific context this allows a setup to be dedicated to particular experiment for extended periods, allowing for example follow up of long term evolution in the systems under study. The main limitation of X-ray tubes is that the low brilliance of the tubes causes them to be unsuitable for some of the cutting edge research that is possible with sources having higher brilliance.

In the context of X-ray imaging the low brilliance is a limitation both for the achievable resolution and availability of different contrast modes. For example modern scientific and technological trends demand the ability to image features of interest whose physical dimensions are shrinking. This gives X-ray imaging new challenges – higher and higher spatial resolution, yet with high time efficiency.

X-ray imaging benefits important advantages from synchrotron radiation compared to laboratory sources. Synchrotron radiation (SR) is the electromagnetic radiation which arises from the movement of relativistic accelerated charged particles (e.g. electrons or positrons) on a curved trajectory[17]. It is a remarkable source of photons in the wavelength range of X-rays and ultraviolet radiation. SR was first observed in 1946 as a byproduct of a particle accelerator, today referred to as first-generation synchrotron. In the 1970s second-generation synchrotrons were constructed and optimized for the emission of SR,

followed by third generation synchrotrons, where the X-rays are not only produced in the bending magnets which keep the electrons on the curved trajectory, but also by insertion devices. Insertion devices can be divided into wigglers and undulators, which force the charged particles on "slalom-like" trajectories.

SR is characterized by several significant properties, such as high intensity, broad spectral range, high polarization, pulsed time structure, natural collimation and small source size. These features enable studies that would be impossible or impractical to realize with X-ray tubes. The next five paragraphs introduce some of the key benefits of SR, compared to the laboratory source, from the point of view of X-ray imaging.

Artifacts due to beam hardening can be avoided. Beam hardening is a phenomenon which occurs, when polychromatic radiation is used, i.e. the X-ray beam has a rather wide energy distribution (spectrum). The spectrum changes as the beam passes through the sample, its maximum being shifted to higher energies as the lower energy photons have a higher absorption coefficient. The X-ray beam is said to be hardened. Beam hardening leads to problems in assigning a value of the absorption coefficient to a defined point in the object, in turn leading to beam hardening artifacts. One way to avoid this is to use monochromatic radiation, possible on synchrotron radiation sources due to the high flux and low divergence of SR.

Because of the high spatial coherence[18,19] of the X-ray beam on third generation synchrotrons it is possible to exploit the phase shift of an X-ray beam passing through an object[20–22]. Imaging with phase contrast is a very useful method for the investigation of light materials since the phase of an X-ray beam is changed more significantly than its amplitude, being exploited in absorption imaging. It can also be used to distinguish areas with similar X-ray attenuation but of different electron density in absorbing samples. Especially, propagation based holography with suitable phase retrieval algorithms is an important tool to image soft materials, e.g. biological samples.

Cone-beam artifacts are avoided. In order to obtain a large coherent cross section an imaging setup working with a synchrotron radiation source has a large distance between source and sample. Therefore it is a non-divergent beam incident on the sample (well approximated by a parallel beam geometry) and to no significant magnification. However, using high resolution (HR) detectors and exploiting the high intensity of SR it is possible to achieve higher spatial resolutions than by laboratory methods. Since the detected intensity scales down with the pixel area, an intense beam is required.

In order to make *in situ* imaging, the measurements must be fast enough to follow the process of the sample i.e. the exposure time is limited. Thanks to the high flux of synchrotron radiation sources, it is feasible to use white beam for fast *in situ* measurements by use of absorption contrast[23]. The limitations on the speed are then mostly determined by the rotation motor turning speed and the detector read-out time.

X-ray fluorescence is widely used for elemental analysis and chemical analysis, particularly in the investigation of metals, glass, ceramics and building materials, and for research in geochemistry, forensic science and archaeology. However, the fluorescence process is inefficient, and the secondary radiation is much weaker than the primary beam. Third generation SR sources can get high energy X-rays with high flux and on a small pencil beam/focal spot which can compensate this negative effect[24].

4

In addition to the beneficial properties of SR sources, improvements in computing technology have contributed greatly to the development of X-ray imaging techniques. It is via computationally intensive calculations, that 3D volumes can be reconstructed based on projection data. The segmentation, analysis and visualization of such 3D volume data depends also on computing technology. The computational power has increased by several orders of magnitude during the past decades (following closely the famous Moore's Law[25]), and the brilliance of X-ray sources has increased even faster than the computational power. X-ray imaging is therefore currently in a situation where more brilliant beams and more computational power are available than ever before, and this progress is likely to continue in the near future. Therefore more elaborate and advanced X-ray imaging techniques can be developed, relying on the technological improvements that these advanced techniques will become practical tools in the near future.

X-ray 3D tomographic imaging techniques are based on obtaining projections around a sample from different angles, and using computational reconstruction techniques to convert these projections into a 3D map of the measured quantity. Traditionally such computed tomography (CT) techniques use a diverging beam from an X-ray tube and utilize the attenuation of X-rays as contrast mechanisms. Synchrotron radiation computed tomography (SRCT) uses the parallel nature of the beam and allows for different contrast mechanisms such as absorption, phase and fluorescence. In addition high resolution can be achieved by using special detector designs or by using X-ray optics.

CT techniques generally require that the sample fits completely in the field of view in every projection. If this is not the case, then some reconstruction artifacts will result from the parts that move in and out of the field of view. An extreme case of this is when the sample is so anisotropic that transmission from certain angles is not possible at all. Then information from these angles cannot be collected, and some of the necessary data for good reconstruction is lost. A specific example of this kind of sample is flat samples, where transmission for most angles is good, but for some angles where the sample surface is close to the beam direction there is no transmission at all.

Computed laminography (CL) is a technique that is especially developed for imaging flat samples. In CL the sample rotation axis is not perpendicular to the incident beam, which allows rotating a flat sample around its surface normal. Thus the transmission remains roughly equal for each projection. CL has been previously established in laboratories as well as at synchrotrons (SRCL). In this work we develop SRCL to provide different contrast modes (phase-contrast, fluorescence), the ability to work on different length scales (from below 100 nm to several micron voxel sizes) and towards time-resolved imaging (for in-situ measurements). The main contributions of this thesis are towards fast and towards high resolution nanolaminography. The rest of the work is structured as follows:

Chapter 2 gives the theoretical basis of SR imaging, giving the necessary background information about X-rays and their interactions with matter. Furthermore CT and CL are introduced and their theory developed, with finally an introduction to the work that has been previously done with SRCL.

Chapter 3 presents a comparison of image quality of CT and CL for a flat sample, and describes the image processing techniques used for SRCL data treatment and analysis

which have been developed during this work.

Chapter 4 details the implementation of SRCL at the nanoscale, where particular attention is given to the design that optimizes the fluorescence contrast while minimizing the scattering contribution. Demonstrations of achieved experimental resolution and capabilities of fluorescence imaging are also shown.

Chapter 5 is dedicated to applications in materials sciences, where *in situ* experiments on an Al alloy and a polymer composite demonstrate ability to follow crack propagation under varying loading conditions. Another aspect under study is microelectronics, where the structural integrity of whole detector chips is studied non-destructively, as well as Pb free solder bumps in *ex situ* and *in situ* current stressing. Finally, correlative studies of structure and elements distributions at the nanoscale are demonstrated.

Chapter 6 shows applications in life sciences, where emphasis is put on biological and medical applications of nanoimaging. Cases covered include toxicology, genetic modifications and biological nanostructures. Many of these results depend on the ability to combine structural and elemental imaging on the same sample. Some applications in microimaging of fossils are also shown.

Chapter 7 presents the conclusions and outlines a future outlook for further development of SRCL.

2 Synchrotron Radiation Imaging

This chapter is devoted to the basics of synchrotron radiation imaging. We will explain how the radiation can be used to produce images of objects. Firstly we introduce the different contrast mechanisms which can be applied with synchrotron radiation. Then we detail the possible geometries, computed tomography and computed laminography, for 3D imaging. In the end, we show practical implementations of CL.

2.1 Imaging Contrast Mechanisms

X-rays interact with materials mainly via the electric field of the X-ray wave field which couples to the electrons in the material. The main interaction mechanisms for photons at the energy range used in this work (10 to 100 keV) are elastic and inelastic (Compton) scattering, and photoelectric absorption[26–28]. These basic interaction mechanisms determine the effect that the material has on the X-rays: attenuation (due to absorption and scattering), X-ray phase shifts and refraction (due to elastic scattering), diffraction (due to elastic scattering from highly ordered materials), and fluorescence (due to absorption followed by an atomic transition). Different materials cause different effect on the X-rays, and observing this difference gives rise to contrast in X-ray imaging techniques.

X-ray interactions with the material can be well described in the wave picture that takes into account the attenuation and phase shift of the waves. Physically the attenuation arises as a combination of photoelectric absorption and both elastic and inelastic scattering. The measured values for attenuation for different elements are tabulated as a function of energy[28]. The phase shift arises from the elastic scattering, and manifests itself in refraction and reflection phenomena. Both of these effects can be summarized by using a complex index of refraction[29].

A plane wave in vacuum (at a given instant of time) can be described mathematically by $e^{i2\pi z/\lambda}$, where z is the position along the direction of travel and λ is the wavelength of the X-rays. If the wave travels inside a material instead, there are additional factors from the material properties that affect both the phase and the amplitude of the wave. Generally these changes are described by the complex index of refraction which can be written as

$$n(x, y, z) = 1 - \delta(x, y, z) + i\beta(x, y, z) \tag{2.1}$$

The refractive index decrement δ corresponds to that the electrons in the material scatter the incident wave to the forward direction. The scattered waves have the same wavelength as the incident wave and they interfere with the incident wave, but with a phase shift of $\pi/2$ and reduced amplitude. This creates a sum wave that is slightly out of phase with the incident wave. The electron density in the material determines the value of δ (which depends on energy as well). The imaginary part of the refractive index β describes the absorption, and in the wave picture corresponds to scattering at a phase difference of π as compared to the incident wave. For X-rays δ and β are small, typically $\delta \sim 10^{-8} - 10^{-5}$ and $\beta \sim 10^{-10} - 10^{6}$.

To proceed, we introduce two additional approximations, specifically paraxial conditions

and projection approximation. The paraxial conditions require that in the ray picture of geometric optics the rays are closely parallel to the optical axis. The projection approximation on the other hand implies that the scattering in the object is weak, so that a wave at the exit surface of the sample is determined by the phase and amplitude shifts that are accumulated along the line of the unscattered beam[30].

The wave traversing an object experiences varying phase shift and attenuation along its path, and thus to take the effect of the object into account we have to integrate over the wave propagation direction to get the total phase and attenuation. If we define that the wave travels into the z direction, the wave at the exit surface of the object can be written as[30]

$$\psi(x,y) = \exp(-i2\pi L/\lambda)\psi_0(x,y)\exp[-i\underbrace{2\pi/\lambda\int_0^L \delta(x,y,z)dz}_{\text{phase shift}}]\exp[-\underbrace{2\pi/\lambda\int_0^L \beta(x,y,z)dz}_{\text{attenuation}}]$$

(2.2)

Here ψ_0 is the incoming wave. The two integrals in the exponentials correspond to phase shift and attenuation, and their meaning will be discussed shortly.

2.1.1 Absorption imaging

X-ray absorption can be understood as a decrease in the amplitude of the X-ray wave as shown in equation (2.2). Equally this can be thought as the loss of intensity via absorption of photons in the material (see Fig. 2.1). The intensity $I(x,y)$ is modulus square of the wave $\psi(x,y)$, i.e. $I(x,y) = \psi(x,y)\overline{\psi(x,y)}$, where $\overline{\psi(x,y)}$ denotes the complex conjugation. Thus in the intensity measurement the information of the phase of the wave is lost (the second last term in equation (2.2)) due to the multiplication by the complex conjugate. The intensity distribution at an object exit surface is then

$$I(x,y) = \left|\psi_0(x,y)\exp[-2\pi/\lambda\int_0^L \beta(x,y,z)dz]\right|^2$$

$$= |\psi_0(x,y)|^2 \exp[-4\pi/\lambda\int_0^L \beta(x,y,z)dz] \qquad (2.3)$$

$$= I_0(x,y)\exp(-\int_0^L \mu(x,y,z)dz)$$

Where $\mu = 4\pi\beta/\lambda$ is the linear coefficient of attenuation, or absorption. The absorption coefficient depends on the material properties and the wavelength of the X-rays (see Fig. 2.2). The absorption coefficient is more or less proportional to λ^3, except near the absorption edges that give jumps at wavelengths that correspond to the binding energies of the atomic electrons. Furthermore μ is proportional to the density of the atoms in the material. This dependence on atomic type and the atomic density gives different μ for different materials. Thus absorption can be used as a contrast mechanism for differentiating between materials. By using wavelengths below and above an absorption edge of an element, it is possible to identify materials.

In the exponent of (2.3) we have a so called line integral, a sum of the *μ(x,y,z)* along a line through the sample. From this equation we can see that the logarithm of the intensity is proportional to the line integral of the absorption coefficient, a property which is essential for 2D and 3D reconstruction techniques.
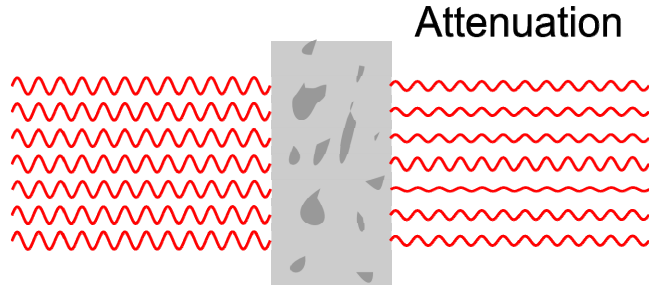
Fig. 2.1 Illustration of X-ray attenuation after sample.
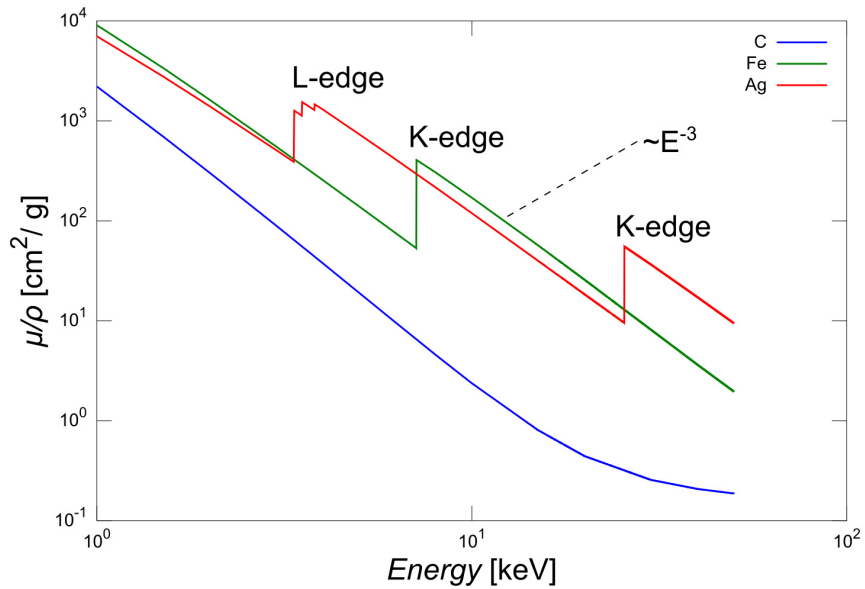
Fig. 2.2 Illustration of the mass absorption coefficients for materials C, Fe and Ag at energies between 1 keV and 50 keV.

2.1.2 Phase shift imaging

While an X-ray wave passes an electron in the material, the electron scatters a small fraction of this wave to the forward direction. Because the scattered wave is out of phase by π with respect to the incident wave, this leads to that the sum wave is slightly shifted in phase as compared to the incoming wave (see Fig. 2.3). This is described by the factor delta in the refractive index. As shown in equation (2.2) a wave traversing a sample experiences the phase shift

$$\phi(x,y) = -(2\pi/\lambda)\int \delta(x,y,z)dz \qquad (2.4)$$

Phase shifts lead to the familiar phenomena of refraction of X-rays at surfaces and to total external reflection at small incidence angles. The change in the X-ray phase is very sensitive to the density variations in the materials. This is shown in the fact that δ is much

larger, even by a factor of 1000, than β for light materials at the X-ray energies of interest. While it is not technically possible to measure directly the X-ray phase, several techniques exist for indirectly obtaining the phase information for the purpose of doing phase contrast imaging.

One method for obtaining phase contrast is to use wave propagation after scattering by an object[31]. When the X-ray wave propagates a distance D in free space before reaching the detector, a diffraction pattern is observed at the detector. Here we remind that the projection approximation is valid for inside the sample (as it is assumed to be throughout this work), and add to that the requirement for the validity of Fresnel approximation for wave propagation after the sample. Sufficient condition for the Fresnel approximation to be valid is that the object that makes the diffraction pattern is much smaller than the distance at which the diffraction pattern is observed. This condition is fulfilled for the imaging techniques described in this work.

Here we are interested in showing how the wave at the sample exit surface propagates to a detector at a given distance D from the sample. In the projection approximation the wave at the exit surface is the product of the incident wave and the sample transmission function, $\psi_0(x,y)T(x,y)$. We assume the incident wave to be uniform, treat the sample transmission function $T(x,y) = \exp[-B(x,y) + i\phi(x,y)]$ as being the wave at the sample exit surface. Here $B(x,y) = \frac{1}{2}\int_0^L \mu(x,y,z)dz$. The intensity recorded at the detector is then given by[32]

$$I(x,y) = |T(x,y) * P_D(x,y)|^2 \tag{2.5}$$

Here * denotes convolution, and $P_D(x,y)$ is the Fresnel propagator, which is given by[32]

$$P_D(x,y) = \frac{1}{i\lambda D}\exp(i\frac{\pi}{\lambda D}(x^2 + y^2)) \tag{2.6}$$

Again, only intensity at the detector can be recorded, but the intensity contains information from the complex sample transmission $T(x,y)$. Thus, with a suitable method, it may be possible to recover $T(x,y)$ and the phase component. The recorded intensity $I(x,y)$ can be converted to Fourier space[33]:

$$\tilde{I}_D(f) = \int T(r_\perp - \frac{\lambda Df}{2})T^*(r_\perp + \frac{\lambda Df}{2})\exp(-i2\pi r_\perp \cdot f)dr_\perp, \tag{2.7}$$

Where $r_\perp = (x,y)$ are the real space coordinates and $f = (f_x, f_y)$ are the spatial frequency coordinates.
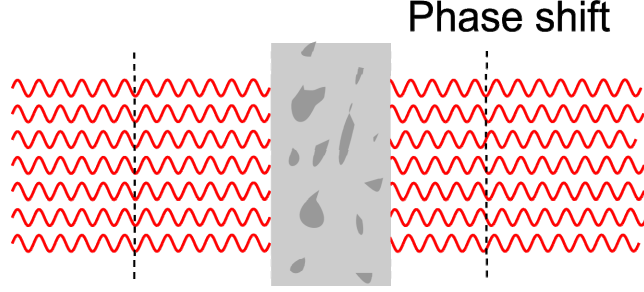
Phase shift

Fig. 2.3 Illustration of X-ray phase shift after sample.

The inverse problem - phase retrieval - can be solved with different methods[34–36]. Equation (2.7) will be the basis for solving the inverse problem. Here we introduce two approaches that are later used to solve practical problems in this thesis.

Phase retrieval from a single image

The complex X-ray wave at the detector plane has *2N* (*N*: number of detector pixels) unknown quantities, twice as many as the number of recorded intensity values. However, by using a relation between the imaginary and real part of the refractive index, δ/β, a solution based on single image can be formulated in case of "homogeneous" samples (where δ/β is constant within the sample). In this case the phase difference and the attenuation experienced by X-rays in the sample are related to each other via the quantity δ/β.

A single distance phase retrieval approach was proposed by Paganin *et al*[34]. In this approach the phase induced by a homogeneous object could be derived based on a single radiograph in terms of δ/β. Their formulation for the phase can be rewritten as

$$\phi = \frac{1}{2}\frac{\delta}{\beta}\log F^{-1}\left\{\frac{\tilde{I}(\mathbf{f})}{D\lambda\pi\frac{\delta}{\beta}|\mathbf{f}|^2+1}\right\} \tag{2.8}$$

Here F^{-1} is the inverse Fourier transform, $\tilde{I}(\mathbf{f})$ is the Fourier transform of the normalized intensity, and $\mathbf{f}$ is the spatial frequency. From this we can see that the method attenuates the higher frequencies according to the parabolic filter in the denominator. In practice the method works remarkably well, if the propagation distance *D* is sufficiently small not to lose too many of the high frequencies. If the term containing the $|\mathbf{f}|^2$ grows larger than 1, then a clear blurring results.

Phase retrieval from multiple distances images

In the more general case, a single value of δ/β cannot be assumed to be valid throughout the sample, and more general approaches have to be used. One of the popular approaches is based on linearizing the sample interaction $T(x,y)$, by assuming weak interaction. From this assumption, a so called contrast transfer function (CTF) approach can be derived. We take the first order of the Taylor expansion of the transmittance function

$$T(x,y) \approx 1 - B(x,y) + i\phi(x,y) \tag{2.9}$$

By inserting this into equation (2.7), the equations can then be solved to get[32]

$$\tilde{I}(\mathbf{f}) = \delta^*(\mathbf{f}) - 2\cos(\pi\lambda D|\mathbf{f}|^2)\tilde{B}(\mathbf{f}) + 2\sin(\pi\lambda D|\mathbf{f}|^2)\tilde{\phi}(\mathbf{f}) \qquad (2.10)$$

Here the term $\delta^*(\mathbf{f})$ is the Dirac delta function (not to be confused with δ in the refractive index), and $\tilde{\phi}(\mathbf{f})$ is the Fourier transform of the phase. Because there are twice as many unknowns as there is data for a single image, multiple images have to be used to obtain a realistic solution. This can be done via a linear least squares fit to the data, giving

$$\tilde{\phi}(\mathbf{f}) = \frac{1}{2\Delta + \alpha}\left[C\sum_D \tilde{I}_D(\mathbf{f})\sin(\pi\lambda D|\mathbf{f}|^2) - A\sum_D \tilde{I}_D(\mathbf{f})\cos(\pi\lambda D|\mathbf{f}|^2) \right] \qquad (2.11)$$

Here $A = \sum_D \sin(\pi\lambda D|\mathbf{f}|^2)\cos(\pi\lambda D|\mathbf{f}|^2)$, $B = \sum_D \sin^2(\pi\lambda D|\mathbf{f}|^2)$, $C = \sum_D \cos^2(\pi\lambda D|\mathbf{f}|^2)$, and $\Delta = BC - A^2$. The solution is ill-conditioned[37] near low frequencies (because Δ approaches 0), which is taken into account by the introduction of the regularizing term α. The assumptions in this derivation are that the attenuation term is weak, and that the phase term is slowly varying. In practice these conditions are sufficiently fulfilled for many types of samples. The method fails if the absorption is too high, or there are abrupt large phase jumps in the specimen.

2.1.3 Fluorescence imaging

X-ray emission from atoms inside the sample is an important source of information concerning the elemental composition of the sample[38]. When an X-ray photon is absorbed, what usually happens at the X-ray energies concerned in this work (below 100 keV) is photoelectric absorption. In this process an electron gets ejected from the atom into the continuum, and the atom is left in an excited state. This process is shown with an example of Fe in Fig. 2.4A. The incoming photon typically loses all of its energy in the process. The hole in the electron shell is eventually filled by an electron from an upper energy level. During this process an X-ray fluorescence photon may be emitted (Fig. 2.4B). The emitted X-ray photons have characteristic energy, depending on the element in question and on the particular electron shell transition that was activated. The energy of the emitted X-rays depends on the two electron shell energy levels involved in the transition. The emitted X-rays are called K-lines, L-lines or M-lines, depending on what is the lower energy level involved in the transition. Each of these lines is further split into multiple sub-lines, depending on the original electron energy level in the transition, giving rise to for example K_α and K_β lines (Fig. 2.4C). As the energy of the incoming photon must exceed the ionization energy needed to remove the electron from the atom, the energy of the fluorescent photon is always smaller than the energy of the absorbed photon.

The fluorescence photons are emitted equally likely to all directions over a solid angle of 4π. The elemental specificity of the fluorescence signal is a clear advantage over phase contrast and absorption that give information only about the materials electron density and linear attenuation coefficient, respectively[39,40]. Scanning fluorescence imaging is attained by scanning the sample with a small beam of X-rays. An energy resolving detector is used to collect the spectrum from each scan point. After data acquisition, the fluorescence spectra can be fitted to get element concentrations at each point. By doing

12

this, 2D images of each elemental concentration in the sample can be built.
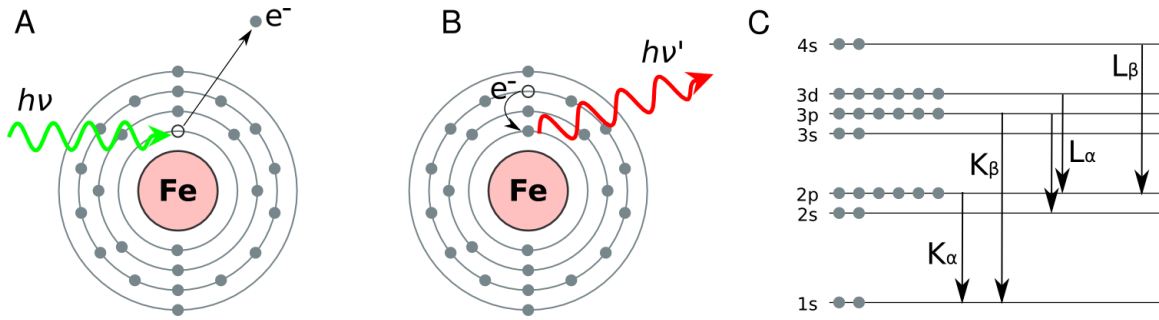
Fig. 2.4 (A) A schematic representation of a Fe atom being ionized via a core-shell excitation by an incoming photon. (B) A schematic representation of Fe ion relaxing towards the ground state by electronic transition accompanied with the emission of a fluorescence photon ($v' < v$). (C) Energy level diagram for Fe atom, showing the possible electronic transitions producing fluorescence.

2.2 Extension to 3D by tomographic techniques

In section 2.1 we introduced different contrast mechanisms which can be applied to get images using synchrotron radiation. Using those contrast mechanisms, 2D pictures of the sample can be formed either by using a 2D detector (for phase and absorption imaging) or by using a scanning probe (for fluorescence). This section explains how the imaging techniques can be extended to 3D. We start by introducing a well established method - computed tomography and then come to the main topic of this thesis - computed laminography.

2.2.1 Computed tomography

Computed tomography (CT) is a non-destructive 3D imaging method. The aim of CT is to achieve cross-sectional images of objects. CT was originally developed for use in medical diagnostics with X-rays[41], and was later adapted for the non-destructive investigation of technical samples[42]. The method is employed to achieve a three-dimensional representation of the inner structure of an object from a set of two dimensional projections. A projection image suitable for tomographic reconstruction is an image of the sample taken from one direction, where the quantity that is imaged can be expressed as a line integral over the sample. Absorption, phase and fluorescence contrast all give such images.
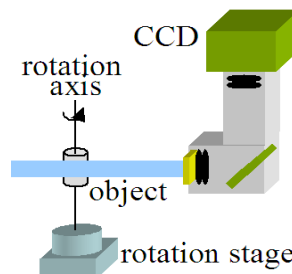
Fig. 2.5 Schematic setup of Synchrotron Radiation Computed Tomography (Image is from Lukas Helfen).

In principle CT involves a data acquisition step (determination of the projections) and a tomographic reconstruction step. Projection images of the sample are recorded from different directions around a rotation axis. Fig. 2.5 shows a schematic setup for SRCT. The sample and the detector are aligned with the beam. Radiographs are taken at different sample rotation angles. As the rotation axis of CT is perpendicular to the beam, a cross section slice of the sample is always imaged to the same line of the detector. Therefore, for CT, it is possible to make fast single slice reconstruction by taking the same lines of all the radiographs.

There exist algebraic and analytic reconstruction methods. Tomographic reconstruction is closely linked to the Radon transform, which is a mathematical formulation explaining the relationship between an object and its projections[43]. The idea of tomographic reconstruction is to calculate the distribution of the unknown object function from the set of known parallel projections from different orientations. Concerning X-ray imaging this unknown object function can e.g. be the spatial distribution of the attenuation coefficient in the case of absorption tomography or the refractive index decrement for quantitative phase contrast tomography.

We now briefly introduce the mathematical principles behind the tomographic reconstruction from parallel projections[44,45]. For parallel beam CT, the incoming beam is perpendicular to the rotation axis. Thus 3D CT can be described as a stack of 2D CT. By looking at Fig. 2.6 we see that the projection of a sample function $f(x,y)$ at rotation angle φ can be written as

$$P_\varphi(t) = \int_{-\infty}^{\infty} f(s,t)\mathrm{d}s \qquad (2.12)$$

Here (s,t) coordinate system is the rotated coordinate system, given by

$$\begin{bmatrix} s \\ t \end{bmatrix} = \begin{bmatrix} \cos\varphi & \sin\varphi \\ -\sin\varphi & \cos\varphi \end{bmatrix} \begin{bmatrix} x \\ y \end{bmatrix} \qquad (2.13)$$

By taking the Fourier transform of (2.12) we get

$$\widetilde{P}_\varphi(w) = \int_{-\infty}^{\infty} \left[\int_{-\infty}^{\infty} f(s,t)\mathrm{d}s \right] \exp(-i2\pi tw)\mathrm{d}t \qquad (2.14)$$

Then by transferring back to the original coordinate system (x,y) we have the result

$$\widetilde{P}_\varphi(w) = \int_{-\infty}^{\infty} \int_{-\infty}^{\infty} f(x,y)\exp[-i2\pi w(y\cos\varphi - x\sin\varphi)]\mathrm{d}x\mathrm{d}y \qquad (2.15)$$

This shows that the Fourier transform of a projection gives a slice through the two dimensional Fourier transform of the object function $f(x,y)$. This is illustrated by Fig. 2.6A and Fig. 2.6B. By taking the projections and their Fourier transforms at many angles φ we can fill the two dimensional Fourier representation of the object, and via this have access to means of reconstructing the original object function $f(x,y)$.

One problem in the direct application of inverse Fourier transform for reconstructing the object is that the projections fill up the Fourier space unevenly. At low frequencies we get

dense information, but at higher frequencies the information becomes sparser, as illustrated in Fig. 2.6C. In order to overcome this problem a filter may be applied to increase the contribution of high frequencies and to reduce the low frequencies. A commonly used algorithm for reconstructing the sample function *f(x,y)* is calld filtered backprojection (FBP). In FBP each projection is weighted in the Fourier space, and then backprojected to real space. The backprojections from each projection are then summed to get the representation of the object. A commonly used filter for weighting the projections is so called Ram Lak filter which can be expressed as $2\pi|w|/N$, where N is the number of projections used and w is the magnitude of the frequency[46]. From Fig. 2.6C, we can also find out that if there are enough projections, the Fourier space is completely filled. It means that we can get complete information of the sample from CT technique.

Due to the working principle of CT, a full access to projections from all directions around sample is needed for good quality reconstruction in the general case. This requirement limits the inspection of some types of samples, especially large or flat objects. If some of the projection angles cannot be measured at all, or the data is of poor quality, reconstruction results in artefacts that deteriorate the image quality. Flat specimens are an important special case, containing for example microelectronic devices, paintings or fossils; samples that have to be tested non-destructively for example to do in-situ measurements or to preserve the potentially valuable and unique sample intact. For flat samples, projections along the sample surface and nearby angles are generally unavailable due to large absorption.
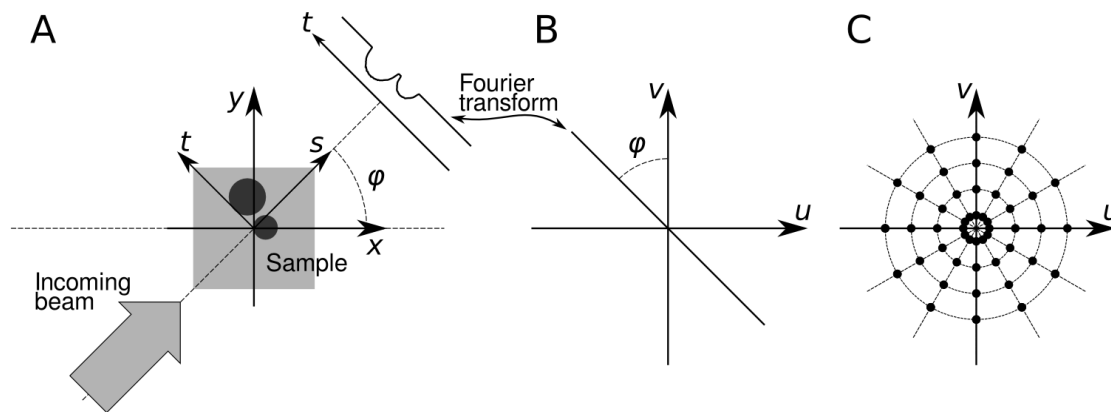
Fig. 2.6 (A) schematic illustration of projection imaging (B)Fourier slice of the projection. (C) Fourier space sampling from multiple projections, the points illustrate the gathered frequency domain data.

2.2.2 Computed Laminography

At a first glance, CT seems to be a non-destructive solution[47]. However, it requires samples to be small enough to fit to the field-of-view of the detector for a perfect reconstruction. Furthermore, for a laterally extended object CT suffers from exceedingly high absorption (and resulting in artifacts from insufficient transmission) when the plate-like object is near to be parallel to the beam direction. To avoid this, a destructive sample

treatment is required and the sample section with the ROI containing the interesting structure has to be mechanically truncated from the sample. The concept of computed laminography allows the ROI of a sample to be imaged without a need of sample truncation.

Before the development of CT a technique called laminography, nowadays known as classic laminography, was already used for imaging of structures inside macroscopic specimens[48]. This classic laminography uses a laboratory source. The source and the X-ray film move around the sample as shown in Fig. 2.7. The beam traverses the sample through different parts, but one layer inside the sample is always imaged to the same position on the film. This movement leads to that the other objects above and below the layer of interest are blurred, but the ones in the layer of interest appear sharp. Thus a chosen layer can be imaged inside the sample, and hence the name *laminography*, which means imaging of layers.
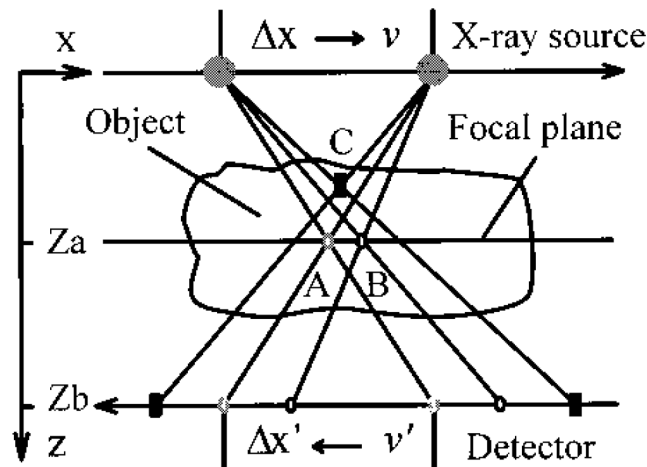
Fig. 2.7 Schematic illustration of classical laminography where the X-ray source and the film move synchronously in opposite directions (image from Zhou 1996[49]). One plane (Za) in the sample is always imaged to the same position on the film, whereas the other planes are imaged to different positions on the detector,

After the development of CT the interest in laminography waned. However, the fact that not every object is fully accessible from all directions gave new motivation to study laminography, as its different scanning geometry would allow imaging flat samples better than CT. This led to a renewed interest on the development of laminography, especially when combining the old idea with the developments of digital detector technology and computed reconstruction techniques.

Zhou *et al*[49] used digital detector technology and improved the laminographic technique by keeping the source and the detector still, but linearly translating the sample. Their technique makes use of the laboratory fan beam characteristic. During the translation of the sample, each small volume element (one voxel of the reconstructed volume) of the sample is imaged from consecutively changing angles, and thus full 3D image of the sample can be reconstructed instead of just one layer.

To make use of the advantages of SR, laminography technique has been transferred from

16

laboratory to synchrotrons by our group[50–52] and recently other research groups as well[53–55]. We will focus on the development and applications of synchrotron radiation computed laminography (SRCL).

SRCL utilizes a parallel beam geometry, and the laminographic scan is done by rotating the sample instead of translating it. The rotation axis is tilted with respect to the incoming beam by an angle less than 90 degrees. In the following this deviation from 90 degrees will be referred to as laminography angle θ, which is defined as the angle between the axis of sample rotation and the direction of the X-ray beam (see Fig. 2.8).

In contrast to SRCT, SRCL is based on the inclination of tomographic rotation axis with respect to the incident X-ray beam, the so-called laminographic angle θ, as seen in Fig. 2.9(a) and (b). With a flat thin specimen aligned nearly perpendicular to the rotation axis, the effective thickness of the specimen seen by the transmitting X-rays does not change significantly during the 360° scan around the rotation axis. During the 360° scan, the ROIs of the specimen which is illuminated at all projection angles are illustrated in dark gray.

Computed laminography follows similar theoretical principles as computed tomography. According to the projection theorem generalized to three spatial dimensions[56] a single 2D projection fills in Fourier space as a plane perpendicular to the incoming beam (illustrated as a pink plane in Fig. 2.9(c) and (d)). The rotation of the specimen fills the Fourier domain successively with data (light gray). But due to the inclined tomographic axis of CL, data are not collected within two cones centered at the axis, above and below the origin of Fourier space, as shown in Fig. 2.9(c) and (d) for $\theta = 45^\circ$ and $\theta = 65^\circ$, respectively. Laminography thus makes only incomplete sampling in the Fourier space, giving rise to characteristic imaging artefacts.

The laminographic angle θ between the rotation axis and the incoming beam determines the extent of the unsampled part, $\theta = 90^\circ$ and $\theta = 0^\circ$ being the two extreme cases of computed tomography (which, however, is not applicable due to the sample geometry) and single direction radiography. The larger θ corresponds to smaller unsampled regions in the Fourier domain, as seen Fig. 2.9 (c) and (d). The characteristic symmetry of the inaccessible region in the Fourier space influences the achievable spatial resolution of detail, which therefore depends on the specimen structure itself[50]. Although the missing information can cause artifacts in reconstructed images, previous CL work has given valuable results in a variety of contexts[51,57–60].

The difference between laminography and CT is illustrated by the example in Fig. 2.10 where a flat sample is imaged. The large, but flat, object leads to some missing angles that cannot be imaged. In the case of this example the missing angular range is ±30° around the sample surface. For CT the missing angular range means that some of the data required for good reconstruction cannot be acquired. This is illustrated in Fig. 2.10(c) where a wedge of missing information is left in the Fourier space. For CL the missing angular range mandates the use of a suitable laminography angle that avoids the problems. Thus each 2D projection gives a plane of information in the Fourier space, but this plane is tilted by an angle with respect to the k_z axis. When the sample is rotated, the plane also rotates in the Fourier space, filling up the space. However, a cone of missing information remains, given by the sample tilt angle. This is illustrated in Fig. 2.10(b).
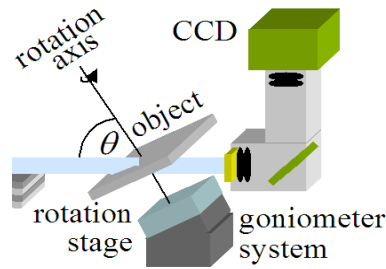
Fig. 2.8 Schematic setup of Synchrotron Radiation Computed Laminography, where the rotation stage is placed on top of a goniometer system in order to adjust the laminographic angle θ (Image is from Lukas Helfen).
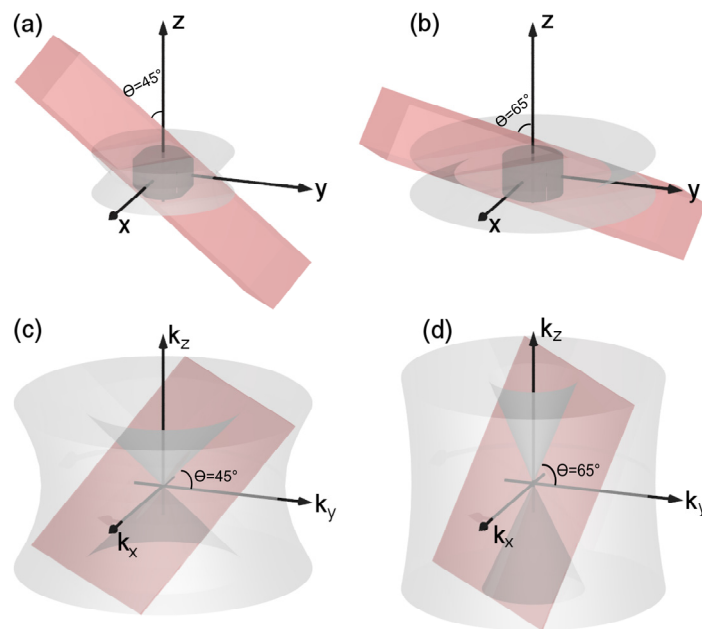
Fig. 2.9 Projection and scanning geometry of SR-CL in real space (a) and (b) for $\theta = 45°$ and $\theta = 65°$ respectively. The pink bars illustrate the incident and transmitted beam at a given projection angle, where θ is the angle of the rotation axis z with respect to the incoming beam. (c) and (d) are sampling in the Fourier domain corresponding to (a) and (b). The pink slices are an example of one projection in Fourier domain. After 360° rotation of the sample, they fill in the Fourier domain as light grey parts.
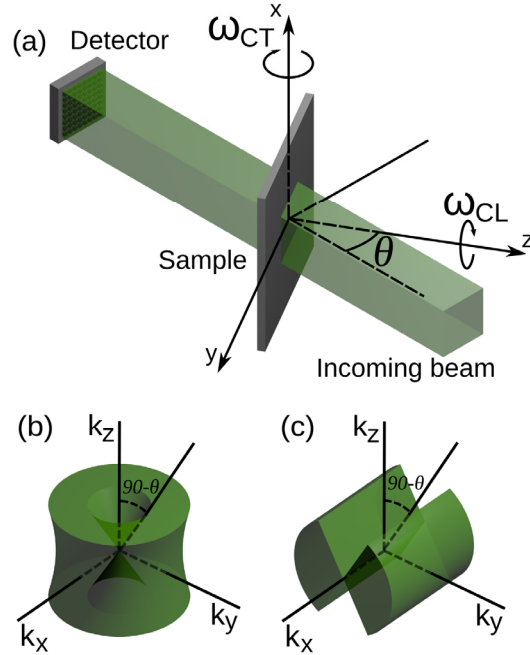
Fig. 2.10 Illustration of the two scanning geometries (a). ω_{CT} is the CT rotation axis. ω_{CL} is laminography rotation axis. θ is the laminographic angle. Sketch of the filling of Fourier space in CL (b) and CT (c) for $\theta = 60°$.

2.3 Full field laminography - Filtered Back Projection Reconstruction

The laminographic reconstruction is usually based on the filtered back projection as in computed tomography but with a modified back projection step and adapted filtering reflecting the different data acquisition geometry. If only a small amount of projections can be obtained, as for instance in fluorescence laminography, Algebraic Reconstruction Technique (ART) will be used instead. In this section we concentrate on the FBP method, reconstruction with ART will be explained in more detail in Chapter 3.

2.3.1 Projection slice theorem for CL

Filtered backprojection is based on the relation between the Fourier transform of the object and the Fourier transform of the projection. To consider how a projection from laminography contributes to the Fourier space, let us consider a sample whose surface normal makes an angle θ with the incident beam, and that has been rotated by an angle ω around its surface normal. Let (x,y,z) be a coordinate system in the sample's frame of reference and (x',y',z') a coordinate system aligned so that the incident beam is parallel to the axis z'. See Fig. 2.11 for illustration. Let $f_{\theta,\omega}(x',y',z')$ describe the sample (rotated by angles θ and ω) in the laboratory coordinate system, whereas $f(x,y,z)$ describes the sample in its own coordinate system. Then a single projection can be written as

$$P_{\theta,\omega}(x',y') = \int f_{\theta,\omega}(x',y',z')\mathrm{d}z' \qquad (2.16)$$

Then, taking the Fourier transform of the 2D projection we get

$$\tilde{P}_{\theta,\omega}(k_x{}',k_y{}') = \int\int P_{\theta,\omega}(x',y')\exp\left\{-i2\pi\left[k_x{}'x'+k_y{}'y'\right]\right\}dx'dy' \tag{2.17}$$

With the sample oriented by angles θ and ω, the transformation between the two coordinate systems is given by $\mathbf{x} = \mathbf{R}_x(\theta)\mathbf{R}_z(\omega)\mathbf{x'}$, where $\mathbf{R}_x(\theta)$ and $\mathbf{R}_z(\omega)$ are matrices describing rotation around axes x and z, respectively. The inverse transform is given by $\mathbf{x'} = \mathbf{R}_z(-\omega)\mathbf{R}_x(-\theta)\mathbf{x}$. We can write the transformation as

$$\begin{bmatrix} x' \\ y' \\ z' \end{bmatrix} = \begin{bmatrix} \cos\omega & -\sin\omega & 0 \\ \sin\omega\cos\theta & \cos\omega\cos\theta & -\sin\theta \\ \sin\omega\sin\theta & \cos\omega\sin\theta & \cos\theta \end{bmatrix}\begin{bmatrix} x \\ y \\ z \end{bmatrix} \tag{2.18}$$
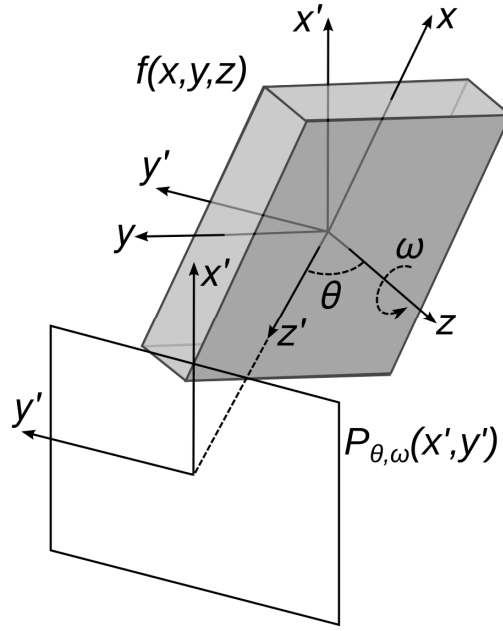
Fig. 2.11 Illustration of the sample coordinate system *(x,y,z)* and the laboratory coordinate system *(x',y',z')*. The beam direction is along *z'* axis.

The Fourier transform of the projection can be rewritten using the relation between the coordinates

$$\tilde{P}_{\theta,\omega}(k_x{}',k_y{}') =$$

$$\int\int\int f(x,y,z)\exp\left\{-i2\pi\left[(k_x{}'\cos\omega+k_y{}'\sin\omega\cos\theta)x+(k_y{}'\cos\omega\cos\theta-k_x{}'\sin\omega)y-k_y{}'\sin\theta z\right]\right\}dxdydz \tag{2.19}$$

This equation is clearly just a Fourier transform of the original sample function *f(x,y,z)* at spatial frequency given by

$$k_x = k_x{}'\cos\omega+k_y{}'\sin\omega\cos\theta$$
$$k_y = k_y{}'\cos\omega\cos\theta-k_x{}'\sin\omega \tag{2.20}$$
$$k_z = k_x{}'\sin\theta$$

This forms a plane in the Fourier space. The plane is tilted by an angle 90°-θ with respect to the k_z axis and is rotated by an angle ω around the k_z axis.

2.3.2 Laminography filter

A single projection in laminography forms a plane in the Fourier space. As is the case for tomography, the different angles contribute to different parts of the Fourier space, and at higher magnitudes in frequency the information is more sparsely distributed than at low frequencies. Furthermore part of the Fourier space remains completely undefined due to the tilt angle θ. Therefore a filter in Fourier space is required to weight the data correctly. Laminography uses a different filter than tomography due to the different scanning geometry[61].

The 3D laminography filter can be written in cylindrical coordinates (k_p, k_φ, k_z) as

$$H(k_p, k_\varphi, k_z) = \begin{cases} (\sin\theta)/2 \cdot \sqrt{k_p^2 - k_z^2 \cdot (\cot\theta)^2} & :| k_z \le k_p \cdot \tan\theta \\ 0 & : \text{elsewhere} \end{cases} \tag{2.21}$$

Where $H = \mathcal{F}(h)$ is the Fourier transform of the 3D filter function h. In the Cartesian frequency coordinate system (k_x, k_y, k_z) we have $k_p = \sqrt{k_x^2 + k_y^2}$, $k_\varphi = \text{atan}(k_y / k_x)$, and θ is the angle between the k_z and beam direction. Then (2.21) can be written as:

$$H(k_x, k_y, k_z) = \begin{cases} (\sin\theta)/2 \cdot \sqrt{k_x^2 + k_y^2 - k_z^2 \cdot (\cot\theta)^2} & :|k_z| \le \sqrt{k_x^2 + k_y^2} \cdot \tan\theta \\ 0 & : \quad \text{elsewhere} \end{cases} \tag{2.22}$$

2.4 Implementation of SRCL

We have explained how SRCL works in theory. Now we will proceed to show some examples how real setup can be realized and how the experiments are done in practice.

For a SRCL setup there are several essential factors. First, for transmission imaging, it is important to have the beam to go through the right region of the sample and to arrive at the detector. As synchrotron source is non-movable, we need to align the sample and detector with respect to the beam. Therefore, for the sample stage, the degree of freedom of XYZ translations is needed. The detectors should have its separate translation system.

Second, SRCL is a 3D imaging technique. In order to be able to take projections from different angles, there must be a rotation of the sample. And in order to keep the region of interest always in the beam, this rotation should not have big wobbling with respect to the detector pixel size.

Third, SRCL requires an inclined sample rotation stage with adjustable laminography angle. This is the main difference from CT.

Fourth, on top of the sample rotation stage, there should be a sample holder that can keep the flat sample on the rotation stage during imaging.

Fifth, in order to position the interesting region of the sample to the beam, there should be

some translation system that can move the sample with respect to the sample rotation stage.

Furthermore it should be possible to move the sample out of the beam and back in the beam with high precision compared to the pixel size. This is required for taking reference images of the beam (without the sample) which is essential for flat field correction at the data processing stage.

One possible example of the schematic setup is shown in Fig. 2.12[52]. The setup consists of a standard compact rotation table (big rotation ω) which gives option to adjust the sample rotation axis to the vertical plane of the beam. The Z translation is sitting on top of the rotation table (XY translations are not shown in the picture. They can be at the bottom of the compact rotation table). The laminographic angle θ is adjusted by a goniometer tilting stage which can go $\pm 20°$. On top there is a fixed tilt of 15° which extends to the possibility to reach 35° for the laminographic angle. Above the tilting stage is the sample rotation stage. The sample holder sits on the sample rotation stage. The sample positioning stage is next to the sample holder which can be different stages depending on how exactly the positioning is done.
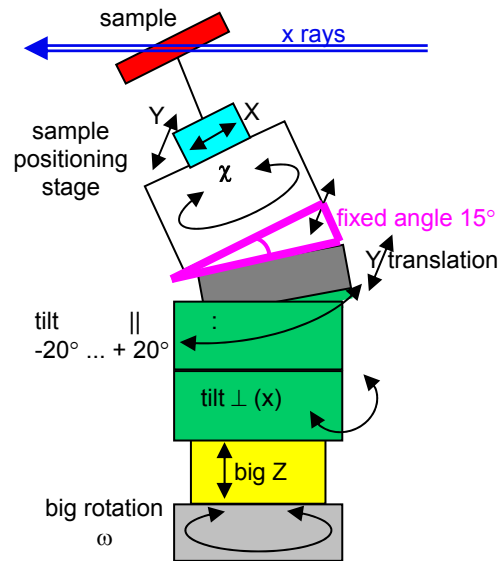
Fig. 2.12 An example of a Schematic setup for laminography (Image is from Helfen 2011[52]).

SRCL has been implemented on different beamlines at the ESRF to use the different beam qualities therefore to meet different application demands. In the following, we will introduce the designs of SRCL from beamline ID15 and ID19 and explain the procedures for SRCL experiments. Laminography setup for nanoimaging at beamline ID22 will be described in chapter 4.

2.4.1 White beam ID15 setup

SRCL is a non-destructive method. Therefore in-situ imaging of specimens is feasible. To make in-situ analysis, the trend is to make fast imaging to follow the changes of the sample under external conditions. To reduce the time of one SRCL scan down to less than one minute for in-situ imaging of foams, for example, enough flux is a critical requirement. Therefore, white beam is a good choice[62].

At beamline ID15 of the ESRF, fast tomographic imaging is one of the main developments. The X-ray energy ranges from 30 to 500 keV. It can use both white beam and monochromatic beam modes. Combined with white beam, SRCL has obtained 3D imaging within some seconds. It can be used to *in situ* observe the repairing process of microelectronic devices[52]. The implementation of the setup is shown as a photograph in Fig. 2.13(A). The X-Y translations are the bottom of the whole setup. This Y translation is used to move the sample out of the beam to take reference images. The sample rotation stage is a commercial motorized 360° rotation stage. The sample holder is made of Aluminum with a cone shape that allows most white beam to transmit. The top part of the sample holder is made to be a flat platform from ferromagnetic material. Therefore a magnetic sample frame can stick to the sample holder during rotation. The sample is positioned by a pusher which can laterally move the sample for a range of 10 cm. Fig. 2.13(B) shows an in-situ experiment set up with gas heating the sample. The sample frame is visible on the sample holder platform.
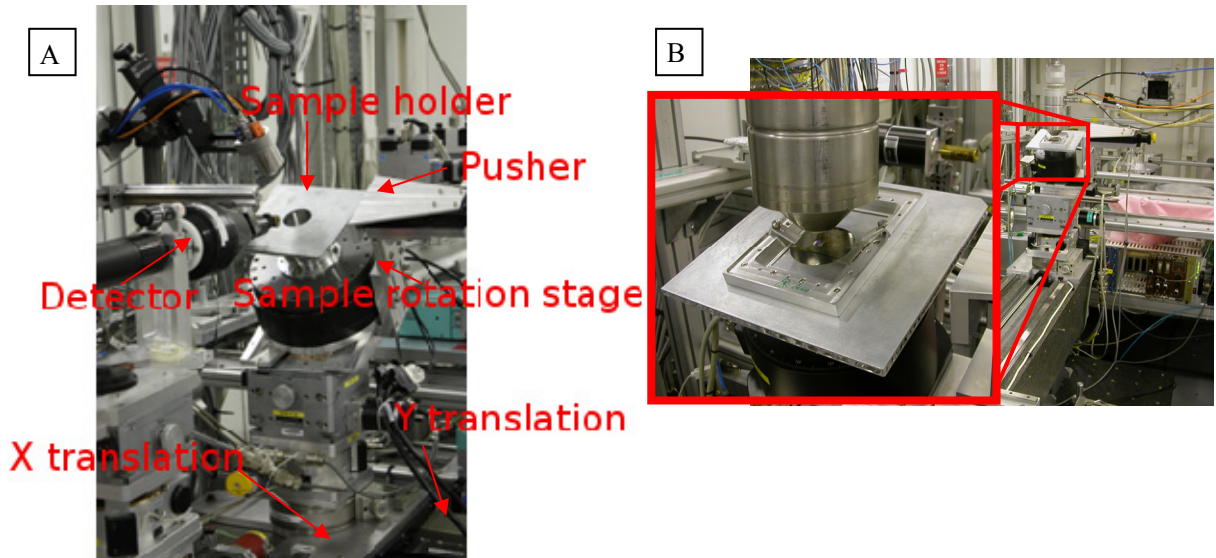
Fig. 2.13 (A) Photographs of the ID15 SRCL setup, (B) Gas heating system for in-situ SRCL experiments.

2.4.2 Monochromatic and white beam ID19 setup

X-ray imaging with white radiation gives mean value of the material property. In order to make more precise quantitative imaging, a monochromatic beam is required. In order to utilize monochromatic and high coherent beam, the beamline ID19 at ESRF was chosen to implement laminography. ID19 at the ESRF is a multi-purpose 145 m long imaging beamline[63]. The beamline is installed on a low-beta section of the storage ring which gives a small source size (30 μm vertical × 120 μm horizontal). There are three insertion devices available (two undulators and one wiggler). The small beam size in combination with the long propagation distance gives high coherence of the beam in the experimental hutch. The beamline can work in the energy range of 6 to 100 keV for either white beam or monochromatic beam. Two monochromators are available: a double Si-111 crystal monochromator ($\Delta E/E = 10^{-4}$) or a state of the art multilayer ($\Delta E/E = 10^{-2}$).

As shown in Fig. 2.14(A), the beam comes from the right side. The inclined round table

serves as a sample stage. It has a hole in the center to let the beam go through. The round table has three supporting motorized legs which can realize the movement of setting the inclined angle. The angle can be set between 20 to 45 degrees. Samples are mounted on a sample holder which is attached to this round table by magnets. The sample holder is square shaped which is shown in the picture Fig. 2.14(B). There are two pushers at perpendicular directions for sample ROI alignment. The reference images are taken by angular offset of the rotation table.
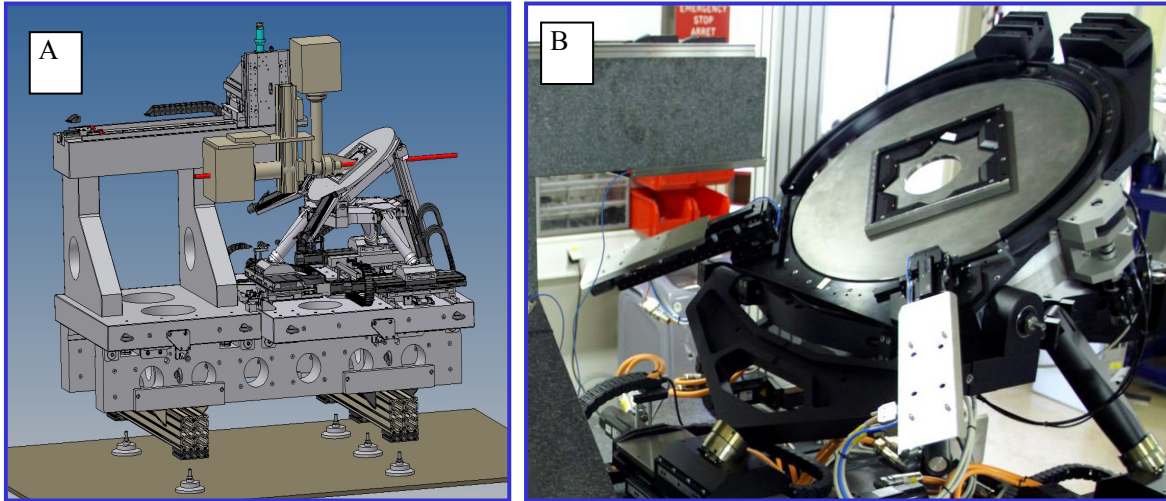
Fig. 2.14 (A) design of ID19 SRCL setup. (B) a photograph of the implementation (Images are from Lukas Helfen).

Experimental procedure

In order to obtain good quality data to use in the 3D reconstruction care has to be taken that the imaging system is properly aligned, and that the laminographic angle is known. The procedures for alignment are as following:

I. Alignment of the stage and detector

For SRCL experiments, we make alignments of the sample stage and the detector first. This is the same procedure as required for a CT experiment. It is done as following: the rotation axis is turned to the perpendicular direction from the beam (laminography angle = 90°). Then we put a needle with sharp tip on the sample stage. By taking two images with 180° rotation from each other, correlating one original image and the other image which is flipped, the rotation axis position and tilt on the detector can be determined.

II. Measurement of the laminographic angle

The exact laminographic angle is measured during the experiment. We make use of the fact that the projection of a circle in a tilted plane is an ellipse. From the ratio of the long and short axes the ellipse, we can derive the exact tilt angle. The experiment is done by imaging an absorbing metal ball for 360° rotation. The metal ball is allocated to be away from the rotation center but all the time within the field of view of the detector. The metal ball forms a circle in the on the rotation table and an ellipse in the detector images.

24

3 Image Data Analysis

As seen in chapter 2, CT and CL are similar in their principles of image reconstruction and data acquisition, but the exact nature of missing information differs. We start the present chapter by making a quantitative comparison of the imaging artefacts arising in the two imaging geometries. From this comparison we are able to establish the conditions in which CL produces better quality results than CT. We then proceed to deal with image processing in case of large imaged volumes where concatenation of 3D volumes is necessary. We also introduce iterative 3D reconstruction techniques for the case when only a limited number of projections could be recorded.

3.1 A comparison of limited angle CT and laminography for laterally large samples

CL is especially developed for flat samples. Meanwhile, limited angle CT has been one solution for flat objects 3D imaging. Limited angle CT is a method that scans the object in CT geometry, with missing projections from certain angle ranges. Despite the great success of CL, little is known about the nature of artifacts as compared to those from CT on a similar sample. In particular it has not been thoroughly justified in the literatures that to what extent CL could offer any benefits over CT within similar angle ranges. To address this we have made a systematic comparison of artifacts arising from these two methods. Our approach is based on simulated images of various types of samples that allow us to identify the essential features of the artifacts, and thus compare CT and CL in terms of image quality. The results can also be found in[64].

3.1.1 Computer simulations and image quality characterization

We simulated forward projections of X-ray attenuation for test patterns made of an arrangement of spheres and rectangular boxes. Projections were calculated to simulate the actual geometries with CT and CL methods, assuming fully parallel beams. From the projected data, volumes were reconstructed using the FBP algorithm in both methods. Hence the two methods were used on an equal ground on the basis of the reconstruction algorithm. Algorithms superior than FBP could have been used for the reconstruction, for example, iterative[65,66] or statistical[67] methods that may work better in case of a limited angular data set, at least in some cases. However, our purpose was to compare the inherent properties of the two imaging geometries, and we do not consider here the optimization of reconstruction techniques; instead we focus on the FBP method and compare the two geometries.

Two main factors play important roles for imaging flat, laterally extended samples: a) the missing angles close to the sample surface directions, and b) the fact that the imaging is local. The latter means that at least some of the projections illuminate some parts of the sample that are not illuminated in all the other projections. The locality of the imaging can cause problems for imaging objects with relatively strong contrast in the partially illuminated region. However, usually the local nature of the reconstruction is trivial, and hence we focused most of our attention on cases where the locality did not have much effect.

Although in our simulations we chose a particular pixel size for detector, and a particular

size and contrast for the objects, the simulation results are actually scale invariant. The relevant quantities are the relative sizes of the objects, and the relative contrasts between the objects. In the simulations the smallest objects for simulation were about 10 pixels in size, meaning that the effect of the detector pixels should be small in the results. Furthermore, ideal conditions were considered: perfect and accurately known orientation of the rotation axis, and noise-free images. Due to the similarity of the two reconstruction methods, the effect of noises should be similar.

Three main directions are considered: the direction along the normal of the sample plane (the CL rotation axis), the direction along the CT rotation axis in the sample plane and the direction perpendicular to the second one in the sample plane. For CL, the two directions in the sample plane are equivalent due to the rotational symmetry, but for CT these two directions are not the same. The direction perpendicular to the sample plane is the most interesting one, since it contains much of the artifacts due to that the undefined part of the Fourier space is mainly in this direction. Furthermore, resolution test patterns for real measurements are usually made as quasi-2D structures using lithographic techniques, which makes them difficult to quantify the image quality in the direction perpendicular to the sample plane in real measurements.

3.1.2 Results

Experimental results

As a starting point for our investigations, a resolution test pattern (Siemens star) was imaged using CT and CL. The experiments were done at the ESRF nanoimaging endstation ID22-NI. Briefly, X-ray propagation phase contrast with a highly focused point source (< 100 nm) was used to get magnified images of the sample (effective pixel size 60 nm) with a good sensitivity to density variations. The data were collected in equivalent conditions by the two methods; and a similar number of angles (1199 for CL and 1499 for CT) were used for projection. The results in the sample plane are shown in Fig. 3.1. As can be seen, the reconstructed images differ visibly from each other. In the transverse direction the image from CT is clearly blurred. This direction is perpendicular to the CT rotation axis. In contrast in the vertical direction the image form CT has less artifacts than the CL image. We will now present a more detailed analysis of artefacts based on simulations.
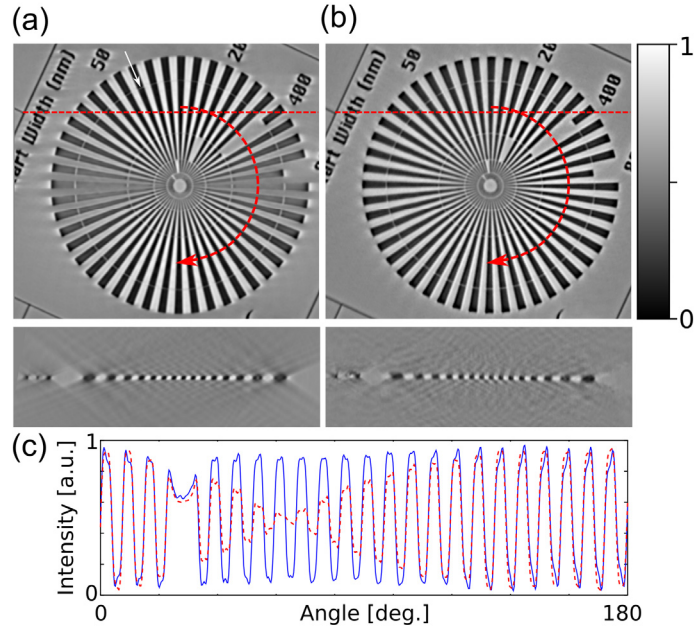
Fig. 3.1 Experimental images of a Siemens star test pattern recorded with CT (a) and CL (b). The top views show slices in the sample plane, and the bottom views show cross sectional slices along the horizontal profile line as pointed out in the top views. The grey scale of the images were normalized for good visualization. The white arrow in (a) indicates the ring mentioned in the text. A plot along the semi circle (depicted in a and b) for CL (solid line) and CT (dashed line) (c). The missing information angle was 30°.

General form of the artifacts

To study the artifacts in the simplest setting, a single sphere located on the rotation axis was used. The laminographic angle θ_{CL} was varied to see how the artifacts develop as more Fourier spaces becomes undefined. Generally in the vertical plane the forms of the artifacts for the two methods are similar as seen in Fig. 3.2, however, in the horizontal plane the image reconstructed by CT shows anisotropy, whereas the image by CL is completely isotropic. The artifacts indicate a change of the apparent height of the sphere by a factor of $1/\cos(\theta_{CL})$, a relation closely followed by the results of CL. The reconstructed height by CT is slightly larger than that predicted, and CT gives the average values 5% larger than CL.

27
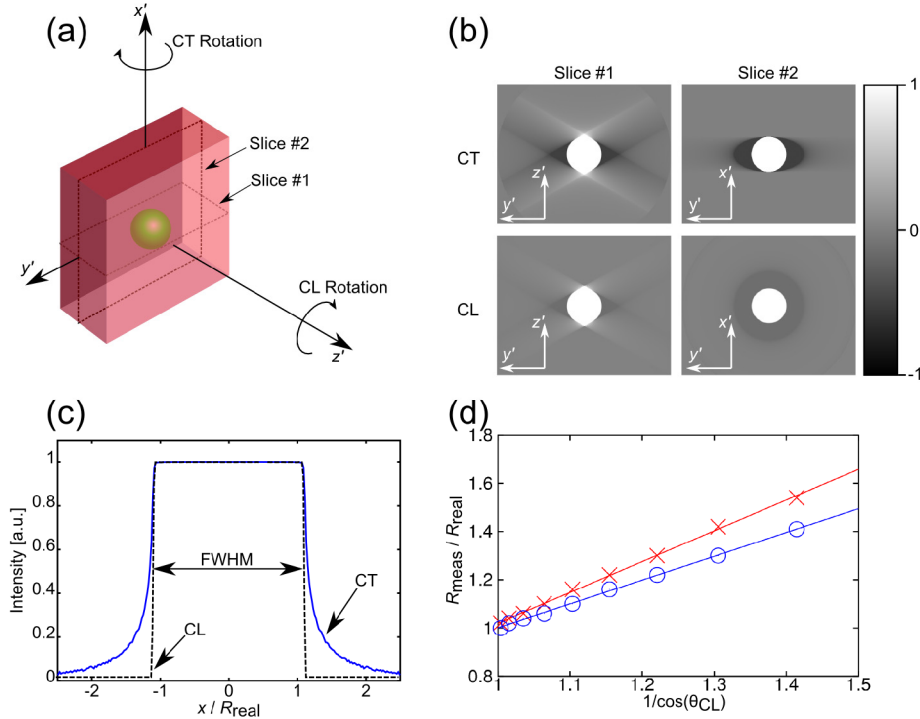
Fig. 3.2 Illustration showing the planes and coordinate system that we choose for inspection (a). Slice #1 and slice #2 of reconstructed single sphere for $\theta_{CL} = 30°$ (b). A plot of the profiles through the central sphere along the CL rotation axis (c). A plot of height, measured as a full-width half-maximum (FWHM) of the central vertical profile, as a fraction of the real radius of the sphere for CT (crosses) and CL (open circles) (d).

Effect of artifacts on resolution

As the artifacts may distort the image, it is possible that artifacts make two objects indistinguishable that would otherwise be possible to see. When the resolution along a given axis is studied, the quantity that plays an important role is the size of the detail along this axis and its relation to the size of the object in the plane perpendicular to the axis. A linear resolution grating made of a series of rectangular boxes of width, W, was used. The longitudinal length, L, of the boxes varies adiabatically along the axis of interest. The profile crossing vertically the middle of the gratings are shown in Fig. 3.3, along with the plots through the middle of the gratings. In the direction parallel to the CT rotation axis, CT produces perfect results in terms of the resolution. At the other axis in the sample plane, CT produces strong artifacts resulting in large errors in the contrast. CL produces results that are somewhere in between the two extreme cases of CT. The vertical plane shows the clearest difference between the two methods. Clearly CL can distinguish objects of smaller L/W better than that of CT. This result is consistent with the previous one obtained from single sphere.
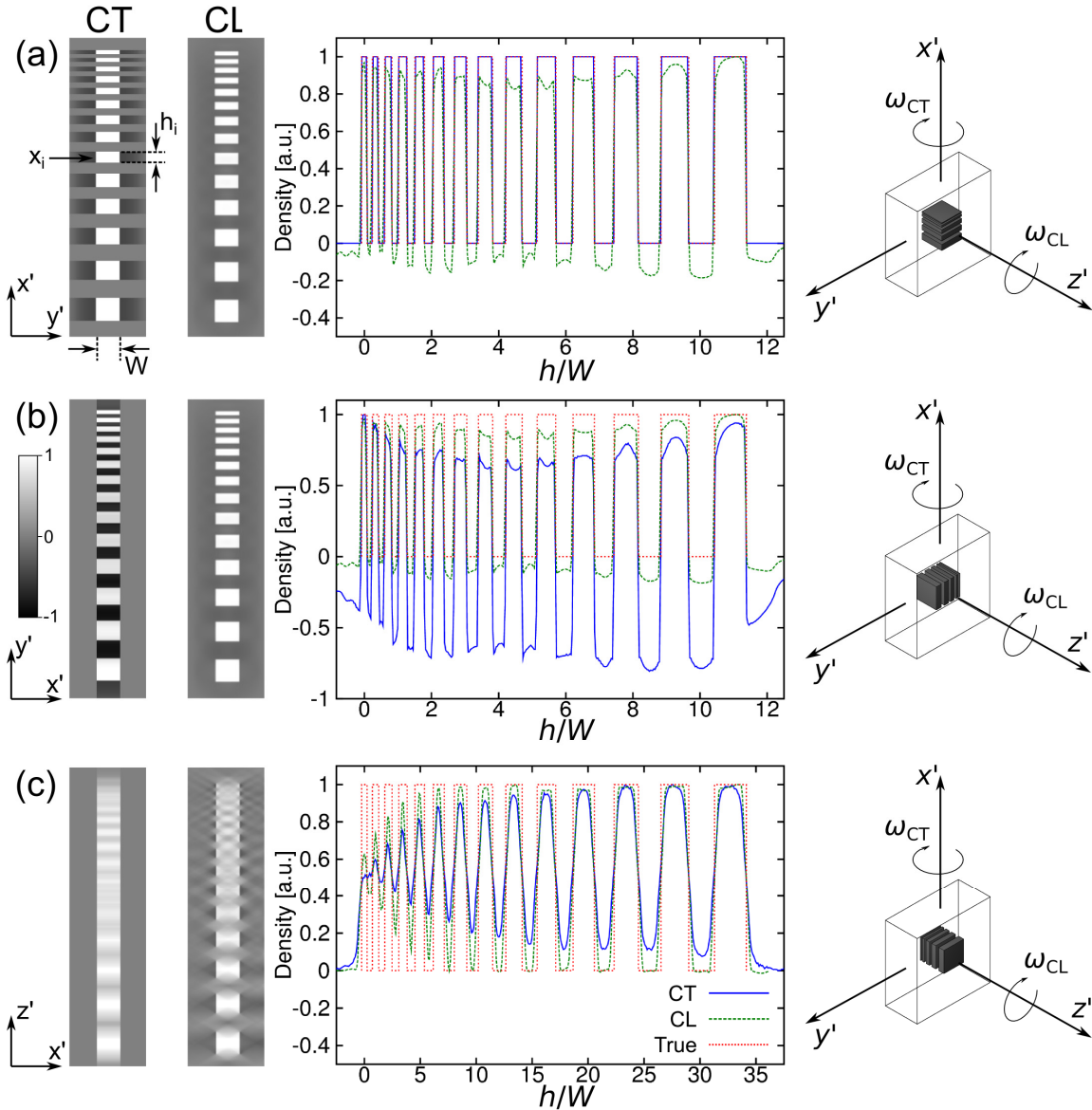
Fig. 3.3 Resolution test pattern aligned along the CT rotation axis (a), perpendicular to the CT rotation axis in the sample plane (b), and along the sample surface normal (c). On the left are shown the reconstructed central slices of the test pattern by CT and CL, in the middle are shown plots through the middle profile line of the test pattern, and on the right are illustrations of the geometry. Note that the profile plot in (c) has a different scale on the horizontal axis than the other two profile plots.

Effects of local tomography

Although local tomography normally plays a minor role, there are some cases where the effect of it can be important. One of such cases is a detail that extends beyond the field of view, such as a long wire on a microchip. In this case the orientation of the wire can play a major role when reconstructing from a CT measurement. If the wire is oriented along the CT rotation axis in the sample plane, then the wire can be reconstructed without a

problem. If the wire is oriented at the direction perpendicular to the CT rotation axis (still in the sample plane), the CT reconstruction will have major artifacts. This is explained by CT being unable to quantify the depth coordinate of the object since due to the missing angles the wire is not seen 'head on' in any projections. This dramatic effect is demonstrated in Fig. 3.4.
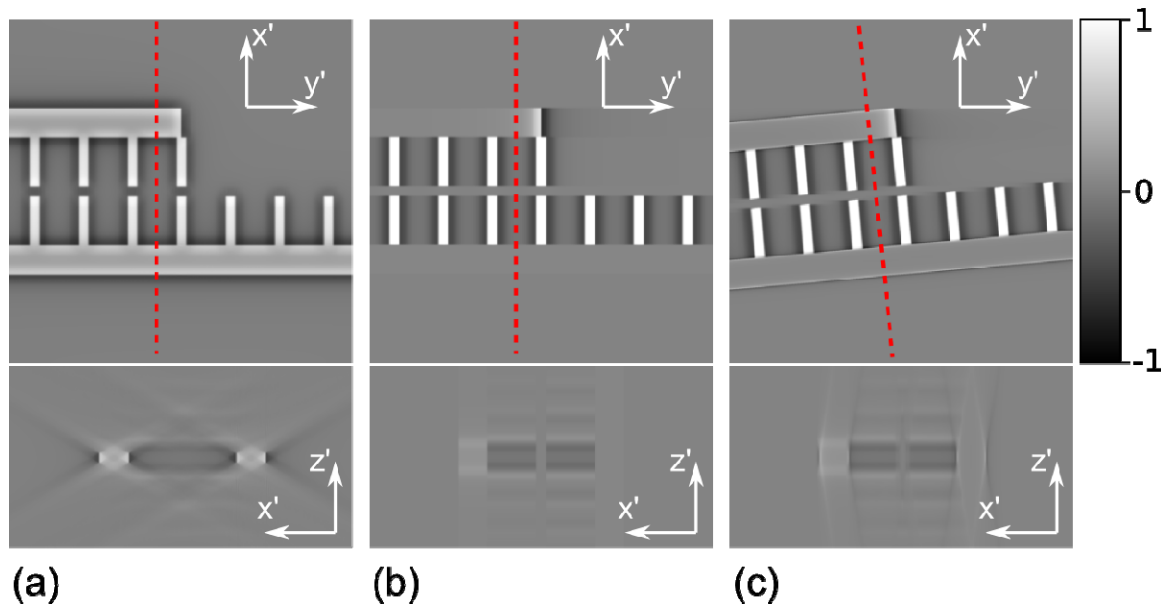
Fig. 3.4 An arrangement of boxes where the two larger boxes go beyond the field of view. Result for CL (a), for CT when the long structures are perpendicular to the rotation axis (b), for CT after rotating the structure by 5° (c). The images above show slices in the plane of the sample, and the images below show cross sections along the dashed lines depicted in the top images.

Effects of noise

So far the imaging has been purely considered as a geometrical problem, disregarding some of the issues in practical implementations. One fundamental concern in practice is the noises from photon counting statistics. In order to study the effect of the noise, we considered a case of a flat and uniform sample, where the limiting factor at low angles is the absorption from the substrate. In this case, the laminographic angle should be chosen so that available incoming photon count gives sufficiently good counting statistics in the transmitted beam. Due to scanning geometry the average transmission for CT is larger than for CL at angles away from the surface larger than angle θ_{CL}. Fig. 3.5(a) shows how the transmitted intensity evolves as a function of the angle for cases where 100%, 99%, 90%, 50% or 10% is transmitted at angle $\theta_{CL} = 90°$. Therefore, it can be expected that CT has a better signal-to-noise ratio (SNR) than CL.

We tested the effect of noise on the linear resolution grating which was used in Fig. 3.3. Results at two values of θ_{CL} were calculated. First CL and CT images were calculated at $\theta_{CL} = 30°$ using counting statistics that gave a reasonable noise level. Then the same incoming photon statistics were used to calculate the result at $\theta_{CL} = 1.8°$. The results with larger angle have a better SNR, while the artifacts are greatly reduced for the case where the angle is smaller. This is applicable for both CT and CL. In the case of $\theta_{CL} = 1.8°$ the

CT result has clearly better SNR due to that more photons could be collected at the angles that were far from the sample surface.
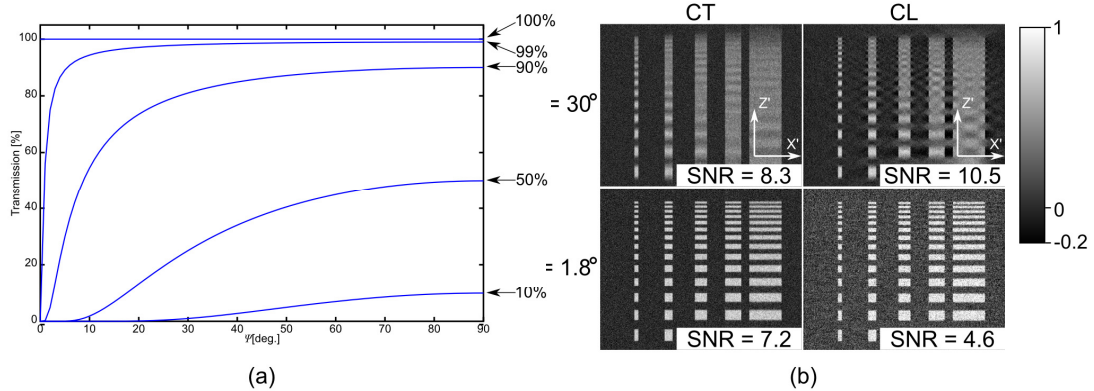
Fig. 3.5 Transmitted intensity as a function of the angle θ_{CL} for differently transmitting flat objects (a). Simulated images of the resolution test pattern with noise for CT and CL at $\theta_{CL} =30°$ and $\theta_{CL} =1.8°$ (b). The values for signal-to-noise ratios have been calculated for the largest detail on the leftmost column of the structure.

3.1.3 Discussion

The choice of laminographic angle depends on one of three things: 1) a strongly absorbing part of the sample or its environment that limits the accessible lowest angle, 2) mechanics of the imaging setup that limit the accessible range, and 3) the absorption in the rather homogeneous sample that decreases the SNR too much at low angles. Concerning the first two, a clear solution is that the smallest angle that avoids the problem should be used as the laminographic angle. In our simulations we have considered things from this point of view, so that the accessible range was taken to be identical for CT and CL.

The third case, absorption in a rather homogeneous sample, is always a compromise between the artifacts introduced and the achieved SNR, given the same exposure time or dose constraints of the imaging. From Fig. 3.5(a) it can be seen that only in the case of very weak absorption there exists a threshold angle above which the absorption increases dramatically. This threshold is invariably close to the sample surface, so that results from CT and CL do not differ much in terms of the artifacts. The results from simulations with noise show that CL does not bring benefits for flat samples that are rather homogeneous, and where the counting statistics is the only criterion in choosing the laminographic angle. Additionally, for CT the exposure time at each angle could be changed so that the transmitted number of photons stays the same, while keeping the total exposure time in CT scan the same as in CL scan. This would give CT a larger angular range than CL, while retaining the same noise level for each projection. However, in this case, care has to be taken that detector nonlinearity does not introduce artifacts when taking reference images.

Therefore, it is only for situations where exists a fundamental limitation to go beyond angles smaller than certain threshold θ_{CL} that CL brings benefits over CT. These

limitations could arise from the sample itself, for example some highly absorbing structure moving into the field of view after certain tilt angle, or some structures starting to overlap so that below a certain angle the absorption suddenly jumps up. In addition, the limitations could arise from the measurement setup, for example from bulky equipment that doesn't allow going closer to the sample surface. In this situation it seems that CL has clear benefits over CT from the artifact point of view.

Here we have mainly considered the absorption induced contrast. For other contrast mechanisms CL has some additional advantages that have not been dealt in the former discussion. For X-ray phase contrast imaging in local CT mode, the phase retrieval is not quantitative. Therefore projections may not get correctly weighed, whereas in the CL geometry each projection should see similar thickness of the sample, allowing projections to be normalized to the same averaged level. One of the most promising method for CL applications is fluorescence laminography. In fluorescence CT some angles would result in situation where the outgoing fluorescent photons have to travel through much of the sample to go to the detector. For low energy photons this would be detrimental in quite large range of sample orientations, limiting the achieved filling of the Fourier space. Additionally, at some angles a lot of the signal would come from regions outside the region of interest, because the incoming beam would traverse a long distance within the sample. For CL, however, the geometry can be always designed so that the fluorescence photons go to the detector along the sample surface normal, minimizing the path in which these photons have to travel inside the sample. Choosing a suitable θ_{CL} minimizes the areas beyond the region-of-interest that would contribute to the fluorescence signal.

3.2 ART reconstruction for computed laminography

The reconstruction problem is "given a subset of all possible projections of an object, estimate its internal density distribution"[68].

There are two approaches to solve the reconstruction problem[68]:

I. Given a certain number of projections of an object, we attempt to obtain as much information as possible regarding the density distribution of the object from the available data.

II. Given a desired level of resolution, we collect data using a sufficient number of projections in order to guarantee that the reconstruction is correct up to that level of resolution.

As scanning technique usually takes N (N = number of pixels in a 2D image) times longer than full field projection imaging, in practice we usually acquire a limited number of projections due to available experimental time. So above mentioned approach I is applied. In this case, to reconstruct the 3D volume, FBP will bring in undesirable artifacts. Another type of reconstruction technique is more suitable for this case, namely algebraic reconstruction technique (ART). In this section, we will introduce the method of ART used for laminographic reconstruction.

ART was first introduced by Gordon *et.al.*[68]. It reconstructs 3D density profiles from three or more projections. Instead of considering the projections in the Fourier space as

the FBP methods, ART works in real space. We start from forward projection. Consider the sample to be composed of N voxels v_j. Let's assume that M pixel values g_i have been recorded in all the projections combined. Then the projection data can be expressed based on the voxels by the use of equations[69]:

$$w_{11}v_1 + w_{12}v_2 + w_{13}v_3 + ... + w_{1N}v_N = g_1$$
$$w_{21}v_1 + w_{22}v_2 + w_{23}v_3 + ... + w_{2N}v_N = g_2$$
$$...$$
$$w_{M1}v_1 + w_{M2}v_2 + w_{M3}v_3 + ... + w_{MN}v_N = g_M$$

(3.1)

Here w_{ij} is the element in the interaction matrix that represents the influence that voxel v_j has on the x-ray coming to pixel g_i (see Fig. 3.6). At this point the formalism is completely general, as w_{ij} can take any form depending on the imaging geometry. In order to solve how the measured quantity is distributed in the sample, we should solve the v_j from this set of equations. The g_i are the measured quantities, and w_{ij} can be calculated when the imaging geometry is known. In matrix notation we can express this as

$$\mathbf{g} = \mathbf{w} \cdot \mathbf{v}$$

(3.2)

Where g = $(g_1, g_2,..., g_M)$, v = $(v_1, v_2,..., v_N)$, and w is the interaction matrix.

The system of linear equations (3.1) is greatly underdetermined ($N >> M$) and thus the system of equations cannot be directly inverted to get v. Therefore, an iterative procedure has to be used [Gordon 1970]. The algorithm starts from an initial guess for the voxel data $v^{(0)}$, which can be for example uniform average value from projections. The algorithm then proceeds in iterations going through all the equations in Eq.(3.1), and updates the voxel data $v^{(k)}$ at iteration k to get the next estimate $v^{(k+1)}$. The update step uses the difference between the measured pixel values g, and the estimation $g^{(k)}$ based on the voxel data. From this difference the voxel data is updated, weighting the contributions by the elements of the interaction matrix w. The correction process can be expressed by

$$v_j^{(k+1)} = v_j^{(k)} + \lambda \frac{g_i - g_i^{(k)}}{\sum\limits_{n=1}^{N} w_{in}^2} w_{ij}$$

(3.3)

Here $g_i^{(k)} = \sum\limits_{n=1}^{N} w_{in} v_n^{(k)}$, and λ is a relaxation factor usually between 0 and 1. Eq. (3.3) is iterated for a given number of iterations or until a merit-of-fit (based on g and $g^{(k)}$) is satisfied.

The basic ART equation (3.3) can be varied in several forms to get reconstructions with different properties for convergence and image quality[70–72]. Generally the best performance for reconstruction is offered by Simultaneous Algebraic Reconstruction Technique (SART)[73–75]. In SART the projection data is considered not on a pixel-by-pixel basis, but each projection direction as a whole. This eliminates some artifacts present in ART, while still retaining a fast convergence. The main update for SART is
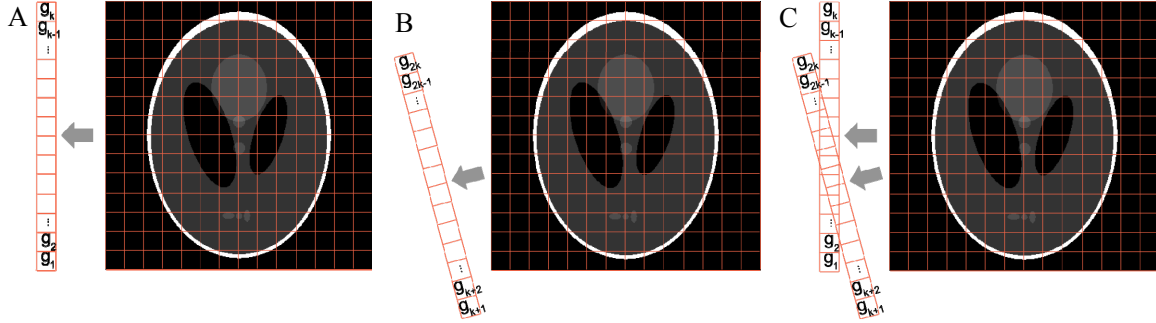
Fig. 3.6 Illustration for 2D object of the notation used for projection data in the ART reconstruction.

$$v_j^{(k+1)} = v_j^{(k)} + \frac{\sum_{i \in P_r}[w_{ij}(g_i - g_i^{(k)}) / \sum_{h=1}^{N} w_{ih}]}{\sum_{i \in P_r} w_{ij}} \tag{3.4}$$

Here P_r is the set of indices corresponding to the pixels in projection r.

ART for laminography

ART and related methods have been used for X-CT and electron tomography, laboratory based laminography and tomosynthesis[69,76,77]. For laminography the main difference comes from the definition of the interaction matrix **w**. **w** contains the effects from both the projection angle and the laminographic angle.

3.3   Reconstructing multiple-FOV volumes

Due to the limited detector size or beam size, the ROI may be bigger than the field of view. For laminography and flat shape of samples, there are two experimental solutions to increase the field of view. First is to make 2D image stitching prior to reconstruction.

This can be used for tomography as well. The second is based on 3D digital volume concatenation of reconstructed sub-volumes. This is not well applicable to CT because each sub-volume has artifacts from local tomography. In the following, we will go to more details of these two approaches.
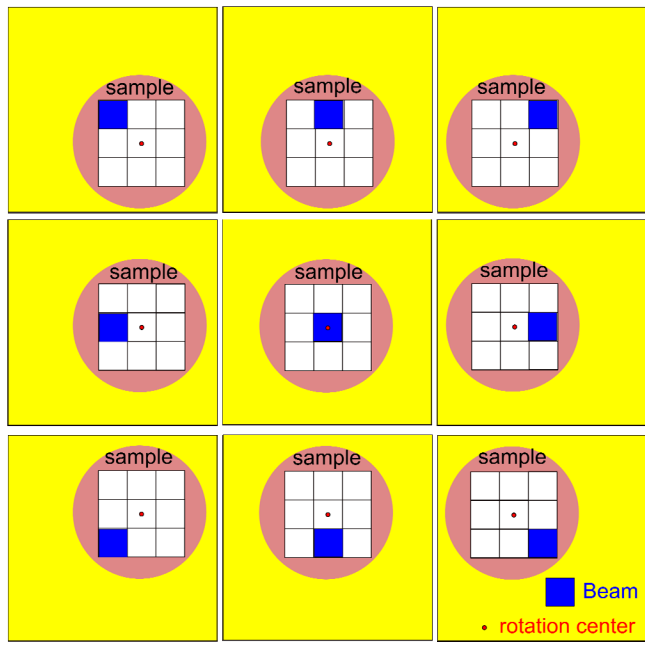
Fig. 3.7 Illustration of data acquisition using 2D projection stitching. Using synchrotron source, the beam shown as a blue square is still with respect to the yellow ground. The sample stage, and thus also the rotation center, is moved with respect to the beam to obtain bigger region on the sample. The images are then stitched to form a big projection that is used in 3D reconstruction to get a multi-FOV volume.
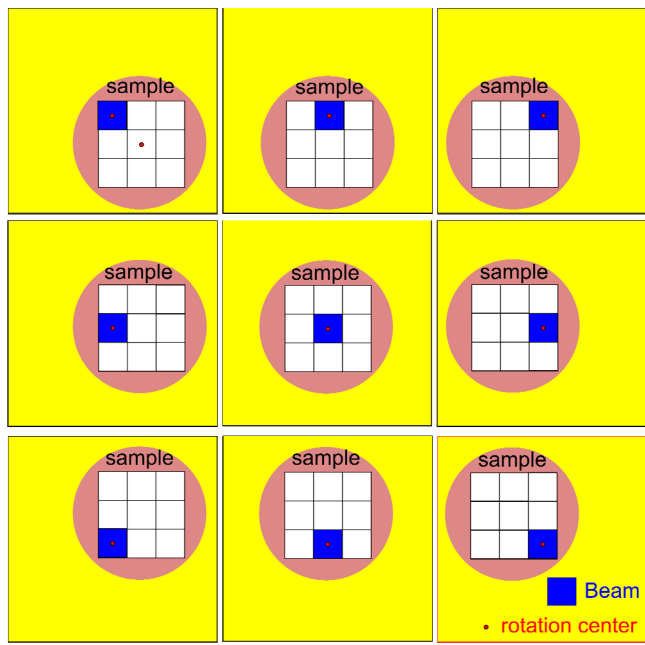
Fig. 3.8 Illustration of data acquisition for the case of 3D volume concatenation. The rotation center is kept at the beam center, and different parts of the sample are moved into the field of view. Each dataset can be reconstructed in 3D independently, and the resulting volumes can be concatenated in 3D to get a mutli-FOV volume.

2D Stitching

One solution to get a multi-FOV volume is to translate the rotation stage across the beam to cover a large illuminated region of the sample. If so the rotation center is not always in the center of the detector view. Fig. 3.7 shows an example of 3×3 scans. The principle is the same for N×M scans (N, M∈ [1, 2, 3, …]). This results in that at one rotation angle multiple images are taken at adjacent regions of the sample. After scanning, we can stitch the image taken at every angle to get a virtual bigger field of view. The stitched images are then used for 3D reconstruction.

In practice, we usually keep a small overlap between adjacent images for every rotation angle. After the scans, by use of the overlapped regions, we can calculate up at a sub-pixel precision how much the images are overlapped, and align the images accordingly.

To implement this. we developed a stitching algorithm based on normalized 2D cross correlation[78,79]. The two images are represented as $f(x, y)$ and $t(x, y)$. To save computing time, $f(x, y)$ and $t(x, y)$ are usually cropped from the original projection images at nearby the overlapped regions. When the size of $f(x, y)$ is equal to the size of $t(x, y)$ the cross correlation can be calculated as,

$$\gamma(u,v) = \frac{\sum_{x,y}[f(x,y)-\overline{f}_{u,v}][t(x-u,y-v)-\overline{t}]}{\{\sum_{x,y}[f(x,y)-\overline{f}_{u,v}]^2 \sum_{x,y}[t(x-u,y-v)-\overline{t}]^2\}^{0.5}} \tag{3.5}$$

where $\overline{t}$ is and $\overline{f}$ are the mean values of the two images in the overlapping region. The values of $\gamma(u,v)$ are between -1.0 and 1.0. The maximum value of $\gamma(u,v)$ corresponds to the best match between the images, and gives the required translation (x_1, y_1) of the images at an accuracy of the pixel level.

To get sub-pixel accuracy[80], a fit with least squares estimation method around $\gamma(x_1, y_1)$ will be used. We estimate the peak with a quadratic function (i.e. a paraboloid) $h(x,y) = a_1x^2 + a_2y^2 + a_3xy + a_4x + a_5y + a_6$. This function is fit to the neighboring 3×3 elements of $\gamma(x_1, y_1)$ by the linear least squares method[81] to find out the coefficients a_i. From the coefficients the position of the peak can be accurately calculated. When added to the pixel level translation (x_1, y_1) found by correlation this gives the required shift between the two images with sub-pixel accuracy. This method is accurate and the images can be of different sizes. The disadvantage is that it is computationally expensive. Application examples are shown in chapter 6.

3D digital volume concatenation

The other approach is to locate separate regions at the rotation center and make independent laminographic scans. This will involve 3D digital volume concatenation [Fig. 3.8]. This is done by iteratively taking two perpendicular slices from the volumes and making normalized cross correlation. The examples of application are shown in chapter 5.

The 3D volume correlation is specific for CL. In CT it might not work well due to the artifacts of local tomography problems at edges. This also allows for narrow structures to be measured in an efficient way.

3.4   3D volume data manipulation

We are imaging thin flat objects with CL. For flat samples, such as flip chips, there often exists a specific direction, a plane that is of interest to visualize. The plane could be *e.g.* parallel to the sample surface or along some other orientation. In experiments, it is not always practically possible to set this interesting plane perfectly perpendicular to the rotation axis. Thus, the plane of interest crosses three directions (X, Y, Z) in the reconstructed 3D volume as shown in Fig. 3.9. To analyze this featured plane, it is necessary to express it as a 2D dataset in XY plane. So we need to rotate the volume along X and Y directions, and interpolate the 3D data.
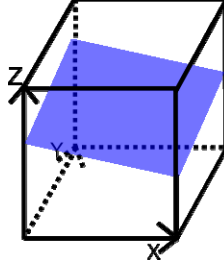
Fig. 3.9 Illustration of reconstructed volume shown in black box and the plane of interest shown in blue.

Another case is that it may be necessary to align reconstructed volumes, from the same sample after *ex situ* experiments, to the same orientation. In this case, 3D volume data manipulation involves rotation and translation along all X, Y and Z directions.

Although this manipulation of 3D volume data can be realized by commercial softwares such as VGstudioMax or Avizo, these softwares are difficult to use to make precise alignment in a repeatable and documented way. Therefore we made a code based on the matrix operations:

$$\mathbf{T_1} = \begin{bmatrix} \cos(\alpha) & -\sin(\alpha) & 0 & 0 \\ \sin(\alpha) & \cos(\alpha) & 0 & 0 \\ 0 & 0 & 1 & 0 \\ 0 & 0 & 0 & 1 \end{bmatrix} \tag{3.6}$$

$$\mathbf{T_2} = \begin{bmatrix} 1 & 0 & 0 & 0 \\ 0 & \cos(\beta) & \sin(\beta) & 0 \\ 0 & -\sin(\beta) & \cos(\beta) & 0 \\ 0 & 0 & 0 & 1 \end{bmatrix} \tag{3.7}$$

$$\mathbf{T_3} = \begin{bmatrix} \cos(\gamma) & 0 & -\sin(\gamma) & 0 \\ 0 & 1 & 0 & 0 \\ \sin(\gamma) & 0 & \cos(\gamma) & 0 \\ 0 & 0 & 0 & 1 \end{bmatrix} \tag{3.8}$$

$$\mathbf{T}_4 = \begin{bmatrix} 1 & 0 & 0 & 0 \\ 0 & 1 & 0 & 0 \\ 0 & 0 & 1 & 0 \\ xt & yt & zt & 1 \end{bmatrix} \tag{3.9}$$

$\mathbf{T}_1$, $\mathbf{T}_2$, $\mathbf{T}_3$ makes rotations at α, β and γ along Z, X and Y axises, respectively. $\mathbf{T}_4$ makes 3D translation of *xt*, *yt*, *zt* along X, Y and Z directions, respectively.

The code takes the angles of rotation as input, and interpolates the original data in a cubic manner to get a new volume. The angles have to be manually determined, for example, by finding out three points on the plane of interest, or by locating the same feature in two corresponding volumes.

3.5 Discussion

We have shown that when the limited angle region is above a few of degrees, CL has some clear advantages over CT. Specifically, the artifacts in the direction of the sample surface normal limit the achievable resolution more strongly in CT than in CL. Furthermore, in the plane of the sample surface, the artifacts created by CT are anisotropic and create clearer features in the images than the isotropic artifacts from CL. For microelectronic and micromechanical devices, and other specimens containing long straightly extended structures, the orientation of the sample was shown to be critical when applying CT. In this type of samples, structures in certain directions, namely perpendicular to rotation axis, could not be reconstructed properly with CT, whereas CL is able to reconstruct structures in every direction equally well. The advantage of CL makes it the method of choice for a number of cases where the full-angle CT cannot be performed. Utilizing the laminographic principle in other tomographic modalities besides X-rays, such as visible light or electron based methods[82], could be used in cases where the projection angles close to the sample surface are not accessible.

Currently, the ART gives good, qualitative volume information. In studies such as biology and medical research, quantitative information of the elemental concentrations is important. The main limiting factor for obtaining quantitative information is self-absorption. Self-absorption diminishes the amount of fluorescence signal coming from deep in the sample, leading thus to underestimation of concentrations inside the sample. Based on the sample structure and elemental concentrations, an iterative correction can be applied during the ART reconstruction phase[83–85]. In laminography the absorption for each reconstructed slice (perpendicular to the rotation axis) depends only on the slices above, so that a correction scheme working on a slice-by-slice basis could be implemented after the full volume reconstruction. Another problem is reconstruction speed. It would be helpful if online reconstruction can be done during data acquisition. In this case, we can decide whether more fluorescence projections are necessary. So future work can be in the directions of optimizing ART for self-absorption correction and quantitative reconstruction, and of speeding up the reconstruction with graphics processing unit.

4 Implementation of Nanolaminography

Motivated by application needs from biology and materials sciences, one aim of our research group has been to develop laminography as a 3D nanoscale resolution imaging technique. We have implemented laminography with absorption contrast at the beamline ID15 and both absorption and in-line phase contrast at the beamline ID19 of ESRF. The spatial resolutions of these two beamlines are limited to the micron level. To go towards nanoscale imaging Beamline ID22 was chosen as a development platform. Beamline ID22NI offers the possibility to go to nanoscale resolution. Nanoscale resolution is obtained by image magnification with projection microscopy, and thus the detector is placed some distance behind the sample. This non-zero sample-to-detector distance leads to wave propagation from the sample to the detector, meaning that a pure absorption image cannot be recorded. Therefore at ID22 we work with phase contrast images. At this beamline the beam is focused to a spot well below 100 nm, and in addition to phase contrast imaging, this beam can be used for scanning fluorescence imaging at the nanoscale. So the laminography at this beamline benefits from nanoscale resolution, with phase contrast and fluorescence as contrast mechanisms. In this chapter we address the general setup of laminography at the beamline ID22NI, and in addition discuss some technical concerns and the experimental procedures.

4.1 Beamline set-up

The main goal of the beamline ID22NI at the ESRF is hard X-ray imaging with nanoscale spatial resolution. In synchrotrons, the distance from the source to the experimental hutch in synchrotrons is usually so high that the beam in experimental hutch can be considered as parallel beam. For synchrotron parallel beam imaging the resolution is currently limited by the pixel size of the detector. The smallest available pixel size is in the range of hundreds of nanometers and the available resolution is in the range of one micron. In order to get nanoscale resolution, an effective way is to use projection microscopy to get magnified image There is no magnification effect with respect to the parallel beam. Moreover, as the source itself (electron bunch) is at least several microns in size, it is too large to be used directly as a point source in projection microscopy. Hence additional optics must be used to define a secondary X-ray source, and to increase the beam divergence that is required for projection microscopy.

The goal is to have the smallest possible focused beam, with high flux, of hard x-rays. The schematic picture of the beamline is shown in Fig. 4.1. We describe here the main characteristics and components of the beamline. The beamline utilizes an undulator source. A single undulator harmonic is used in the energy range from 17 keV to 29 keV. At the ESRF the horizontal emittance of the electron beam is 4 nm rad and the vertical is 0.025 nm rad[86] (present day values have somewhat improved). As ID22 is located on a high-beta section the electron beam has a large horizontal size (400 μm) and a low horizontal divergence (10 μrad). Vertically the source size is smaller, only some 8 μm. To reduce the horizontal source size a horizontal slit is placed in the beam to define a secondary light source in the horizontal direction, with the aperture set to either 10 or 25 μm. Then a platinum coated mirror, installed at 33 m from the undulator source, is used for horizontal reflection. The function of the flat mirror is to cut off the high energy components that are produced by the undulator (harmonic peaks on axis with energy of

odd times of the base energy, 17, 51 keV, etc.). It is important to remove these peaks, because they otherwise give unwanted heat load to the KB system (the KB mirrors may degrade due to radiation damage) and they will bring negative effects to phase retrieval process. The slits and the horizontally reflecting mirror are in a separate optics hutch. Then the only other relevant component is the focusing optics, located in the experimental hutch 63 m downstream from the source.

There are plenty of alternative approaches to focus X-rays, such as capillaries, zone plates (ZP), compound refractive lenses (CRL) and Kirkpatrick-Baez (KB) mirrors. ZPs, CRLs and KB mirrors are commonly used in synchrotrons for different focusing purposes. CRLs are usually easy and cheap to make, and rather easy to align[87]. However, because of the very small numeric aperture[88], only a small part of the incoming beam can be utilized. CRLs also have strong absorption for low energy X-rays (less than 10 keV). ZPs are more efficient for lower energy appliction[89]. Both CRLs and ZPs are chromatic, meaning that the focal distance changes if photon energy is changed. The merit of KB mirrors is the large aperture of acceptance, which depends on the length of the mirror and the incident angle. The non-chromatism of focus with energy is good for spectroscopic applications. Moreover, the KB mirrors have good efficiency, because of high reflectivity at grazing incidence. The disadvantages are the technical difficulty for the fabrication of very long (typically 50 to 100 mm) mirrors with sufficiently small surface roughness and non-straightforward alignment due to the elliptical bending required.

At ID22NI a KB mirror system is used for x-ray focusing. The KB optic system is ESRF inhouse developed[90]. The geometric design is shown in Fig. 4.2(a) and a real photograph is shown in Fig. 4.2(b). The KB optics are made of two elliptically shaped orthogonal reflecting surfaces[91]. At ID22NI instead of using pure external reflection from surface, the mirrors are coated with a multilayer[92]. The multilayer increases the angular acceptance of the KB mirroror (from about 2 to 8 mrad). Large acceptance will increase the flux when full mirror length is used and reduce the sensitivity to optical aberrations. The acceptance aperture of the current KB is 0.28×0.52 mm^2 at 17 keV and the working distance is 35 mm from the exit. Another advantage advantage of the multilayer is that it avoids using a silicon crystal monochromator. Because of the large band pass, a full energy bandwidth of one harmonic component from the undulator can be used and we gain two orders of magnitude in the photon flux as compared to using a monochromatic beam. The multilayers necessitate setting the mirror curvature when the incident energy changes. This is accomplished by actuators and an iterative (automated) alignment routine that tunes the mirror bending to optimize the size of the focal spot.

The design of the KB mirror (and the flat mirror upstream) allows an energy range from 17 keV to 29 keV. Presently a focus size of 47 (V) $\times$ 82 (H) nm^2 has been achieved in a routine user mode, giving a flux of more than 10^{12} photons/s at the focus, a medium monochromaticity of $\Delta E/E = 1.5\%$. This flux corresponds to a photon density of more than 10^8 photons/nm^2/s. Such flux allows both full field in-line phase contrast laminography and scanning fluorescence laminography at realistic timescales. The sample stage will be explained in the next two sections.
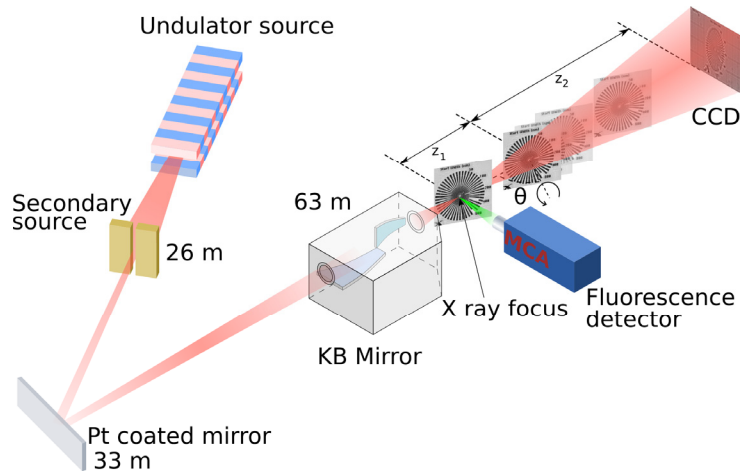
Fig. 4.1 Schematic layout of the ID22NI beamline and experimental setup.
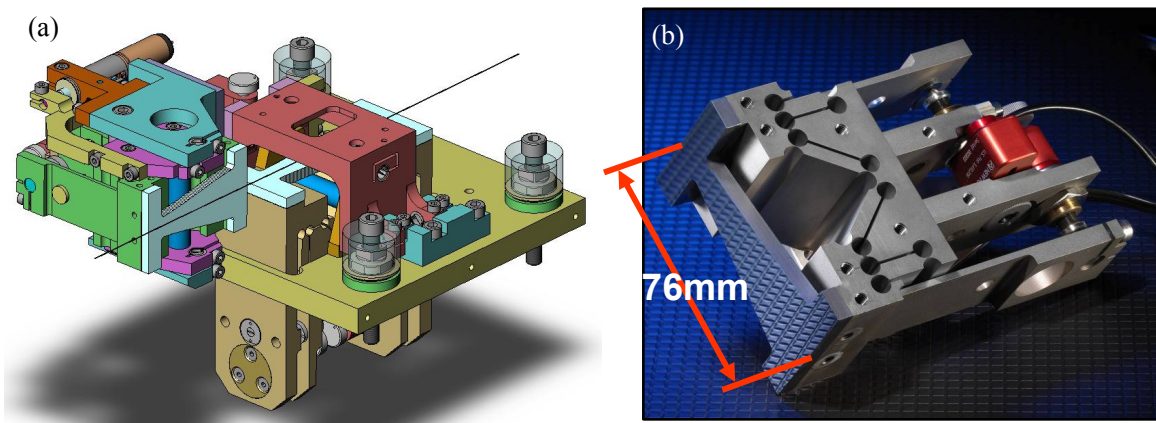
Fig. 4.2 (a) Design of optics geometry of the KB mirrors and benders. (b) Photograph of one mirror and bender. (Images are from Peter Cloetens).

4.2 The design of the nano-laminography setup

As mentioned earlier, laminography using phase contrast and fluorescence contrast at the nanoscale resolution will be implemented. It will be convenient to integrate all modalities into one setup, permitting an easy access to correlative imaging using the two contrast modes. The phase contrast imaging requires that the sample is held in such a way that the pure signal from the sample can be recorded. In practice the beam will traverse through a sample holder as well, and it is important that the sample holder does not cause appreciable contrast. The fluorescence imaging places further constraints on the design of the setup. The influence of Compton scattering places demands on the correct detector positioning, while the self absorption of fluorescence signal determines the good sample orientation. We will now discuss these points in more detail.

4.2.1 Influence of Compton Scattering

The scattering coming from the sample (mainly Compton scattering, but also elastic scattering) should be minimized, because if the scattering is too strong it can saturate the detector. Thus the minimization of scattering coming to the detector is an important part

of the design of a fluorescence imaging setup. When imaging trace elements, the scattering signal can be much stronger than the fluorescence signal, and this can cause two problems. Firstly, the scattering signal can saturate the fluorescence detector, which is typically an energy resolved photon counting detector. To remove the saturation the incident intensity would need to be lowered, which would slow down the imaging data collection. Secondly, the scattering signal can be many orders of magnitude higher than the fluorescence signal, and it could contribute significantly to the background intensity of the energy spectra at the energies where the fluorescence lines are located. This would reduce the signal to noise ratio of the measurement, and thus increase the detection limit. Thus it is important to minimize the scattering coming to the detector.

The X-ray scattering signal depends on the polarization state of the incident radiation. Especially, in the polarization plane and perpendicular to the incoming beam direction, the elastic scattering is completely eliminated[93]. At this direction the Compton scattering also reaches a minimum[94]. Synchrotron radiation coming from an undulator source is polarized in the horizontal plane (the plane where the electrons undulate in the undulator). Therefore it is possible to minimize the effect of scattering by placing the fluorescence detector perpendicular to the incident beam and in the horizontal plane. Fig. 4.3 shows the measured energy spectra and scattering signal at two positions of the fluorescence detector. When the detector is at 90 degrees with respect to the incoming beam, the scattering amplitude is dramatically decreased from the case where the direction of detector is 75 degrees (the detector has an opening angle of a few degrees, which means that even at 90 degrees position the elastic peak does not go to completely zero).
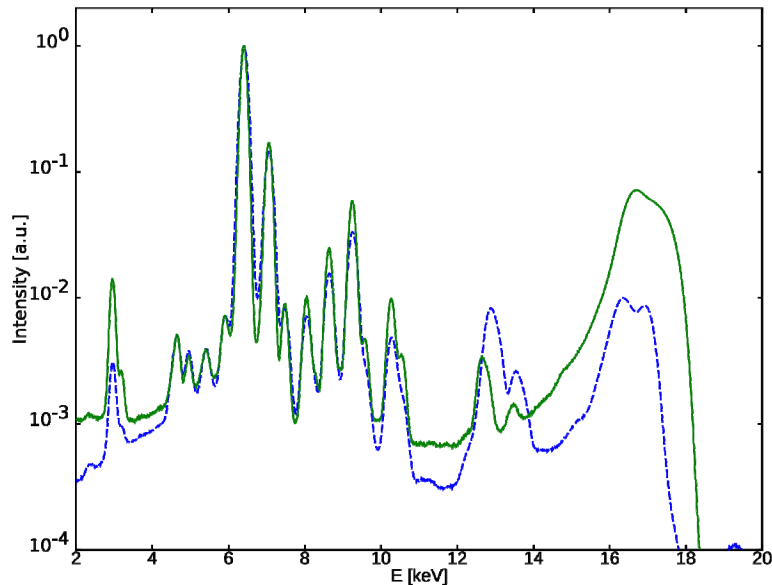
Fig. 4.3 Energy spectra, elastic and Compton scattering peaks of an Al foil Sample at two positions of the fluorescence detector placed in the horizontal plane at 90 degrees (dashed line) and at 75 degrees (solid line) with respect to the incoming beam direction.

4.2.2 Influence of self-absorption

For a given sample, the self-absorption of the fluorescence signal is dependent on the outgoing fluorescence beam path. For dense samples and/or low fluorescence energies

the quality of the collected fluorescence signal depends heavily on the mutual orientation between the sample and the detector. The absorption is inversely related to photon energy, and as the incoming beam energy is usually much higher than the fluorescence energy, the effect of the incident beam path is typically negligible. In the design we therefore optimize the geometry of detector to minimize the path length of the outgoing fluorescence inside the sample.
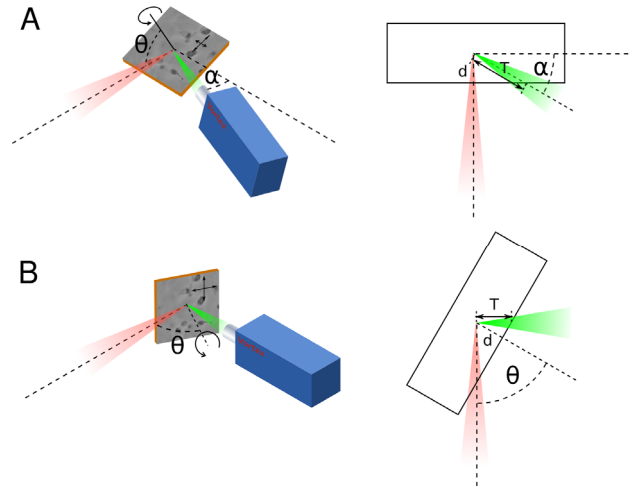
Fig. 4.4 Effect of the different paths of two laminography setups. (A) Vertical rotation axis. (B) Horizontal rotation axis.
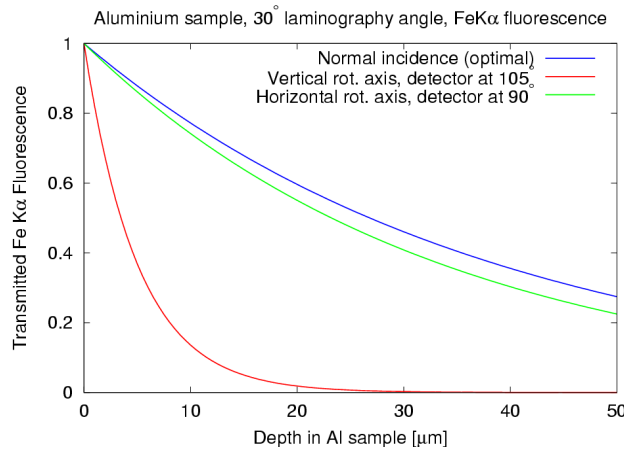
Fig. 4.5 Simulated fluorescence transmission of Al foil at vertical and horizontal laminography rotation axis

In the usual laminography geometry which is used for ID15 and ID19 setup, the rotation axis is close to the vertical direction [Fig. 4.4(A)]. As the fluorescence detector is in the horizontal plane, tilted by an angle α from the ideal 90 degrees position, the photon coming from depth d in the sample has to pass through thickness $d/cos\theta/sin\alpha$ in the sample. Here θ is the angle between the incoming beam and the rotation axis. To minimize the Compton scattering, the detector would ideally be placed perpendicular to the incoming beam (*i.e. α=0*). But, in this case, the fluorescence signal would have to

travel through the whole width of the sample, which is not compatible with the idea of imaging flat and large samples. Usually we therefore set the detector at an angle α with respect to the perpendicular position in the horizontal plane, typically α being 15 degrees. Fig. 4.4 (B) shows the improved approach: horizontal rotation axis. The detector is put to be perpendicular to the incoming beam. So the path of the fluorescence inside sample is $d/\sin(\theta)$. The improvement looks like a minor detail; however it has a remarkable effect which will be shown in next section 4.2.3.

4.2.3 Simulations of the fluorescence imaging geometry

To compare the two orientations of the rotation axis we simulated the Fe $K\alpha$ fluorescence signal coming from different depths in an Al matrix. The results are shown in Fig. 4.5, where the laminographic angle θ was 60 degrees. The blue curve is the case when the detector is perpendicular to the sample surface. This geometry is optimal for the absorption, but could result in large signal from Compton scattering. The red curve is for vertical rotation axis, with $\alpha = 15°$. The green curve is the case with horizontal rotation axis and the detector at 90 degrees from the incoming beam. It is clear that for the case of vertical rotation axis, from the depth of 10 μm the transmission is well below 20%. For the horizontal axis, even from the depth of 50 μm we still get more than 20% transmission.
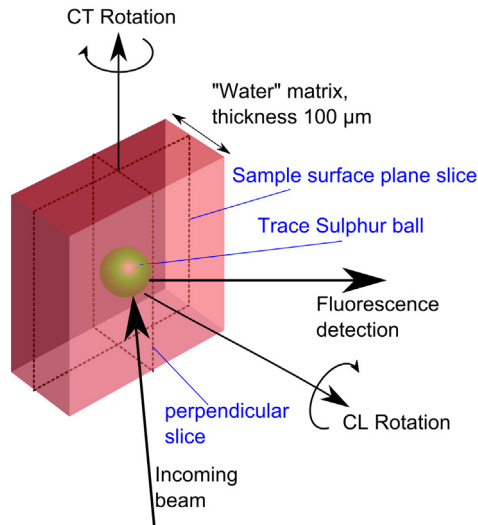
Fig. 4.6 Fluorescence scanning geometry of CT and CL.

In addition to comparing the two laminographic geometries, we show here a simulation-based comparison of the image quality of CT and CL for 3D fluorescence imaging of flat, thin objects. Fig. 4.6 shows the different scanning geometries of CT and CL for fluorescence imaging. For CT, the rotation axis is along the vertical direction (parallel with the surface). For CL, the rotation axis is perpendicular to the sample surface. The sample is a 100 μm thick water matrix, shown in red color, inside there is a sphere containing a trace amount of sulphur, shown in green. The fluorescence signal is detected at 90 degrees from the incoming beam. The simulation was done with ray tracing principle[95]. The fluorescence was calculated using a voxel based method where the sphere was divided into small voxels. For each voxel, the incident beam intensity was

calculated by taking into account the attenuation of the beam in the matrix and in the other parts of the sphere. Then the outgoing beam was similarly tracked to outside the sample. By combining these two calculated attenuations we got a number that represents the relative amount of fluorescence signal coming from each voxel to the detector. We will now examine two central slices of the sulphur sphere. One is along the sample surface plane; the other is the perpendicular slice.
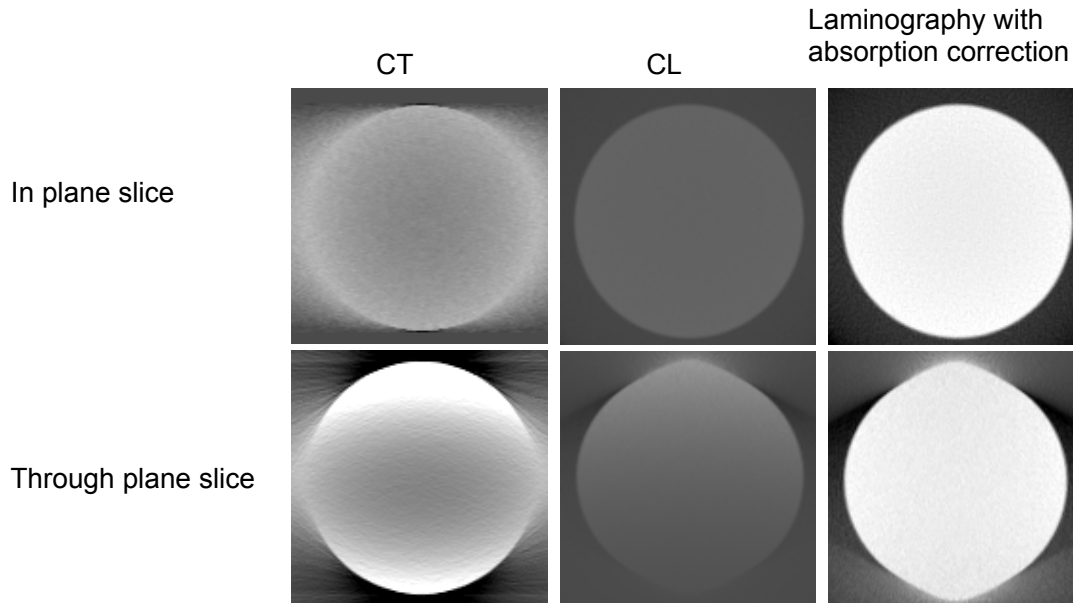
Fig. 4.7 Reconstructed cross sections of CT and CL. The two planes marked in **Fig.** 4.6 are examined.

The simulated results are shown in Fig. 4.7. The top row shows the slices from the sample surface plane direction. In CT, the artefacts are anisotropic along the radial direction. While for CL, in this plane, there are no visible artefacts. In the perpendicular plane both have artefacts, for CT the artefacts come from differences in self absorption depending on if the part is close to sample surface or far away from the surface. For CL the artefacts come from missing information in Fourier space sampling. Because the absorption is different for every projection angle of CT self absorption can not be easily corrected after reconstruction. In Computed Laminography the absorption is similar for all angles, for rather homogeneous samples the self absorption only depends on the depth from sample surface, so we can correct the self absorption effect. The corrected images are shown in the right column.

4.3 Full field phase contrast laminography

4.3.1 Introduction

Due to the non-zero distance between the sample and the detector the magnified projection imaging produces propagation based phase contrast. This allows phase imaging that is sensitive to small differences in electron density, but also makes necessary to use phase retrieval. There are three main approaches for phase contrast imaging techniques. One is grating interferometer based differential phase imaging[96–98]. Another is

diffraction enhanced imaging (DEI) by use of an analyser crystal placed between sample and detector[99–101]. Here we mainly talk about the third one: propagation based phase contrast imaging, also called inline holography.

Inline holography bears the advantage over the other two methods on its extreme simplicity of instrumentation[102–104], as it can be easily modified from absorption radiography just by increasing the sample to detector distance. Additionally, compared with the other two approaches, inline holography offers better dose as it utilizes no optics after the sample. Because of the possibility to use magnified projection imaging, the propagation based method offers better spatial resolution than the other two methods. As compared to DEI, which utilizes a monochromator before the sample, propagation based imaging offers a much higher photon flux on the sample, enabling faster imaging.

Propagation based phase contrast imaging underwent a rapid development only after the third generation synchrotron radiation facilities have been built because it requires a (partially) coherent beam. Inline holography is not a straightforward method for data analysis because it records Fresnel diffraction patterns. Phase information needs to be retrieved from the recorded intensity, and it offers quantitative information[104]. See chapter 2 for further details on the phase retrieval.

4.3.2 Experimental procedure

Alignment

To make a magnified phase-contrast laminographic scan, there are three main steps for sample alignment. It is important to know the focus-to-sample distance at an accuracy comparable to the depth of X-ray focus (which is of the order of 50-100 μm) , so first we need to move the sample to the focal plane. This is done with the help of a visible light microscope that has been previously focused to the X-ray focal plane. The depth of focus of the optical microscope is only of the order of 10 microns, so the visual observation for the image sharpness gives sufficient accuracy for optimizing the focal plane. The sample position thus obtained is used as the reference to set the distances used in the phase contrast imaging. The second step is to set the focus-to-sample distance values to be used for imaging. The smallest distance is chosen to give the desired pixel size. In phase retrieval at ID22NI typically 4 focus-to-sample distances are used, and the other three distances are then chosen appropriately to give good results for phase retrieval. The third step is to align the rotation axis to be close to the middle of the field of view. This is done in two steps, first a rough alignment at a large sample-to-focus distance (large field of view), and a refinement at the closest chosen focus-to-sample distance. The rotation axis is aligned based on the criterion that objects go around the rotation center on an elliptical trajectory (as seen on the detector). Thus, 10 images with 15 degree intervals are recorded and summed, which gives a good indication of the central position of the ellipse. The sample stage is then moved so as to bring the ellipse center to the center of the field-of-view. Another aspect of the alignment is to find a suitable sample region to image. Once the rotation axis position is known, the sample can be moved with respect to the rotation axis position to put the correct region-of-interest (ROI) in the field-of-view.

Unlike in tomography, the rotation axis of laminography is not perpendicular to the beam. For accurate reconstruction this angle needs to be determined as precisely as possible. Hence an additional measurement of the laminographic angle needs to be made. We make use of the fact that a projection of a circle in a tilted angle is an ellipse. By measuring the

46

long and short axes ratio, we can obtain the tilt angle and thereby laminographic angle. In order to reach high accuracy, a highly absorbing 100 μm diameter ball made of nickel is used as a test object. The Ni ball is pushed some distance away from the rotation axis on the tilted laminography stage (while still remaining in the field of view of the detector). By making a certain number of projections, we are able to fit the ellipse and calculate the laminographic angle.

Imaging

At each of the four distances, a full laminographic scan is made. Sample is rotated around 360 degrees, typically 1500 to 2000 projections are used. The rotation is continuous, so that structures far from the rotation axis get somewhat blurred. This blurring helps to reduce the artefacts arising from the locality of the imaging. The exposure time varies from one experiment to another, and is typically between 0.1 s and 0.5 s per projection. Because the incident beam is highly structured (mainly due to effects of the optical components) a flat-field normalization has to be employed, where the image with the sample is divided by a reference image taken without the sample. Reference images are taken at the beginning of the measurement. At given intervals during the measurement the rotation is stopped, and reference images are taken. These reference images during the scan are necessary to ensure a high quality of flat-field normalization even if the incident beam changes significantly during the scan. The detector used for phase contrast imaging is the FReLoN[105] detector. The detector uses a 20 μm thick scintillator screen, which is optically coupled to the CCD, giving a physical pixel size of 0.96 μm.

Propagation based phase contrast imaging with a diverging beam is similar to the parallel beam case[106]. However the images are magnified by factor M = $(z_1+z_2)/z_1$, and the effective propagation distance is D = $z_1z_2/(z_1+z_2)$, where z_1 is the source to sample distance and z_2 is the sample to detector distance (the parallel beam case is a special case of this formulation with z_1 being infinite). The first propagation distance is chosen so as to give the desired pixel size at the sample plane. The other 3 distances are then set to be 1 mm, 5 mm, and 15 mm further downstream from the first sample position, giving sufficiently different propagation effects to be used in phase retrieval. The lateral field of view is confined by desired pixel size set by the largest magnification and the number of detector elements. The thickness of the sample that could be imaged is approximately equal to the lateral field of view. In the high resolution images the X-ray propagation effects are well visible, and the images before phase retrieval resemble the sample only remotely. However, the phase retrieval techniques developed originally for parallel beam case do not make approximations about the resolution or the propagation distance, and they work remarkably well with magnified imaging as well.

4.4 Scanning Fluorescence Laminography

In addition to morphological imaging, we are able to also detect the elemental composition in 3D (both for major and trace elements) via scanning X-ray microscopy and using an energy resolved detector, simply moving the specimen to the focal plane. The sample is raster scanned laterally with respect to the beam to get a 2D map. Similar scan is repeated for different sample rotations to get necessary information for 3D reconstruction. At each raster point a fluorescence spectrum is recorded with an energy resolving detector (Vortex-EX) placed perpendicularly to the incoming beam. The

spectra are then processed by the ESRF developed software PyMCA[107]. Typically we acquire 64 projections for fluorescence laminography, each projection containing about 100×100 points. The step size depending on the application was between 300 nm to 500 nm. In synchrotrons without top-up mode, the beam intensity decays with time after every injection. Therefore the fluorescence signal varies also with time, so the 2D images were normalized by the measured electron beam current in the storage ring before reconstruction. Considering that only a limited number of projections is recorded, the Algebraic Reconstruction Technique (ART) is usually applied for fluorescence laminography. More details about ART are available in chapter 3.

4.5 Implementation of Laminography Stage at ID22NI

Sample movement stages are needed in order to move the sample in and out of the beam, to align the rotation axis with the detector, and to move the sample to suitable distance from focus. For the fluorescence scanning a fast, accurate and repeatable lateral movement is required. For the sample movements, the sample stage has linear translation motorized stages in three degrees of freedom. On top of this moving platform is placed the rotation stage for laminographic scanning of the sample. A piezo actuator in the horizontal direction, perpendicular to the beam, allows for rapid and stable raster scanning of sample over a range of 90. The sample resides on a disc that is magnetically attached to the rotation stage, and by using a pusher it can be slid on the surface to bring different parts of the sample into the field of view. As shown earlier in section 4.2, the horizontal plane is the best choice for the rotation axis for fluorescence laminography, which differs from usual laminography or CT setups where the rotation axis is vertical. To get laminographic images, we align the rotation axis roughly at 60° inclination with respect to the incoming beam. This rotation axis alignment can be changed by a few degrees manually using an adjustment screw. The rotation stage is hosted in a cradle, whose angle can be varied. Presently this angle is fixed by a wedge to give the laminographic angle of about 30 degrees. The angular range of the cradle allows in principle an angle to be varied between 0 and 90 degrees. The 30 degrees is a suitable compromise of image quality and having an unobstructed view of the sample. Fig. 4.8 shows a schematic drawing of the laminography stage and Fig. 4.9 shows a photograph of the actual stage.

The samples are mounted on custom-designed sample holders (Fig. 4.11) which is fixed on top of the rotation stage. The sample holder consists of a base part made of aluminum. On top of the base part a cylindrical glass tube is mounted (diameter 6.5 mm, thickness 50 μm, height 10 mm). The glass tube gives little contrast in imaging (with phase contrast or fluorescence). It is used to lift the sample up away from the sample stage to prevent the beam going through the sample from hitting the stage. The samples are placed on top of the glass tube either directly by gluing or by using a Si_3N_4 (silicon nitride) membrane (500 nm thick, 3×3 mm^2 window size) to hold the sample. The membranes give very little additional contrast and are used for samples that would not be sufficiently stable structurally to be mounted just by themselves.
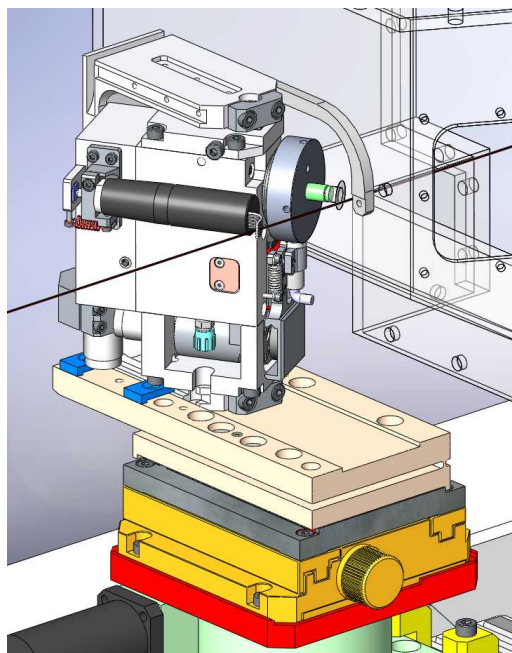
Fig. 4.8 Schematic setup of the nano-laminography stage at the beamline ID22 of ESRF (drawn by Pascal Bernard).
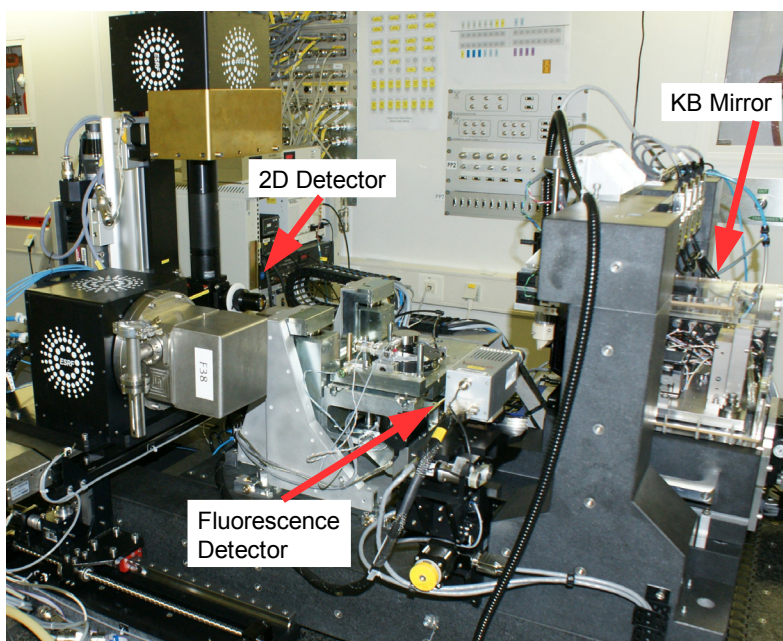
Fig. 4.9 Photograph of ID22NI experimental hutch. The detectors and KB mirror are marked by red arrows.
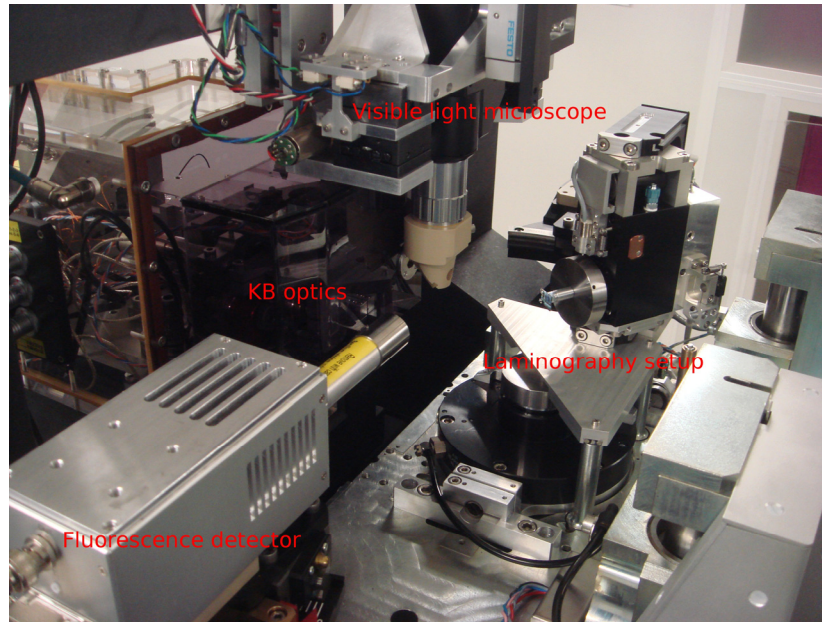
Fig. 4.10 Photograph of nano-laminography setup.
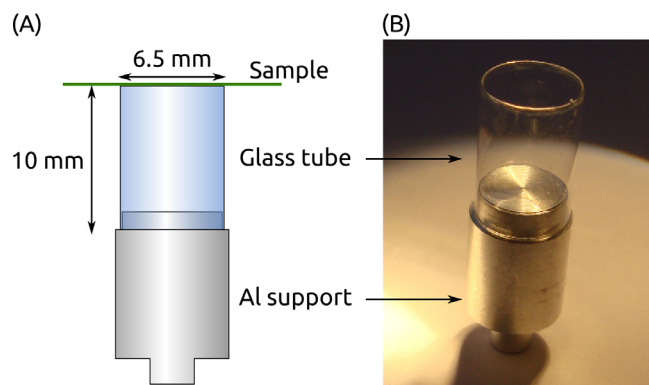
Fig. 4.11 Schematic of the sample holder (A) and a photograph of a nanolaminography sample holder (B).

4.6 Proof of principle experiments

In order to characterize the suitability of the nanolaminography setup we imaged several test samples. We aimed to characterize the spatial resolution, especially in the phase contrast imaging, in order to know that the setup is stable enough to give comparable results as the already established CT setup gives. The resolution characterization was done using a Siemens star test pattern. Furthermore we wanted to show the advantages that our setup has for fluorescence, and we imaged an Al foil for this purpose.

4.6.1 Resolution Characterization

Because of the magnification geometry, in the experiment we can easily choose the effective pixel size by moving the sample longitudinally. While the maximum pixel size is limited to about 0.3 microns by how far the sample can be moved from the focus, there is in principle no lower limit for the pixel size. However, usually we use 60 nm or 50 nm pixel sizes because going much below this would not help to increase the resolution

which has a limit also from the X-ray focus size that is at best about 50 nm. In terms of spatial resolution, focus size, mechanical stability and also the detector point spread function have a contribution as well, so that in practice it is difficult to reach below 100 nm resolution for 3D imaging. In order to characterize the precision of our nanolaminography instrumentation, we imaged a Siemens star resolution test pattern (Fig. 4.12). It is a lithographically fabricated nanostructure, which comparable in structure and contrast to samples that are commonly encountered in many microsystem studies, e.g. electronic and micro-electro-mechanical systems. Here, such a nanostructure gives us an experimental evidence of the achieved resolution in the 3D reconstructed image. The Siemens star pattern is made of a 200 nm (+/-10%) thick gold layer, supported by a 300 nm thick Si_3N_4 membrane. At 17.5 keV x-ray energy such gold pattern results in 96% transmission and a phase shift of 0.177. Fig. 4.12 A-D shows the original images after flat field correction. The features of the Siemens star are blurred due to the highly visible propagation effects. However, phase retrieval works very well in removing the fringes and revealing the true sample structure (Fig. 4.12E). The reconstructed slice in the sample plane is shown in Fig. 4.12F. 3D rendering is shown in Fig. 4.13A. The profile plot in Fig. 4.13B shows that a resolution better than 135 nm has been achieved in the specimen plane. This is very comparable to the actual resolution achieved in 3D tomographic experiment[108].
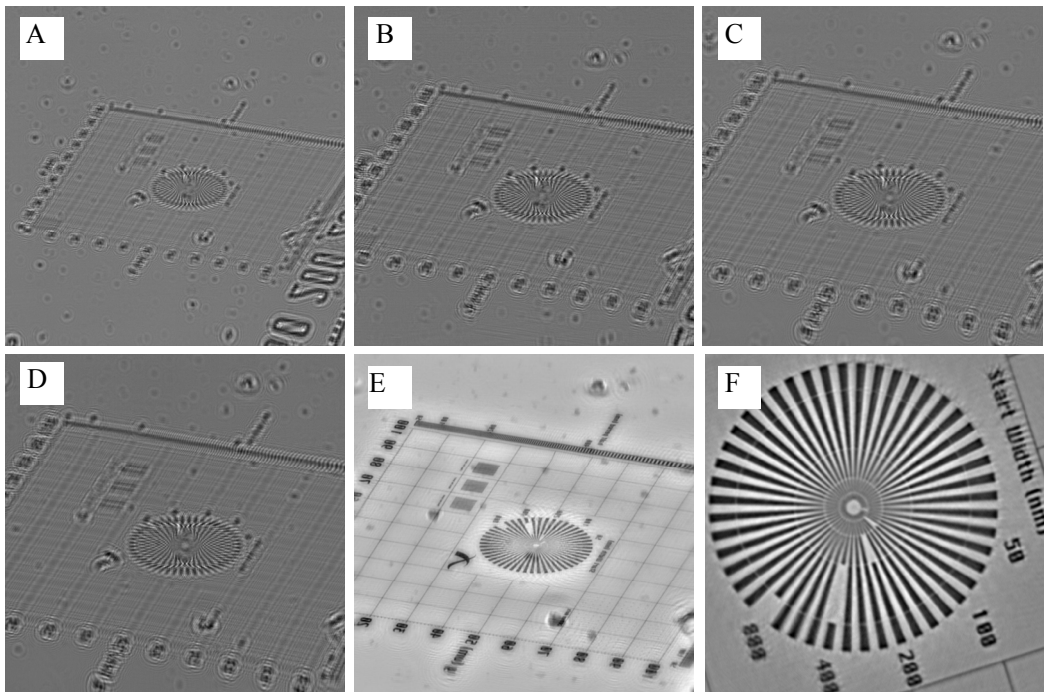
Fig. 4.12 (A), (B), (C) and (D) are four phase contrast images collected with the detector. (E) shows the reconstructed phase map after phase retrieval. (F) is a cross section from laminographically reconstructed volume.
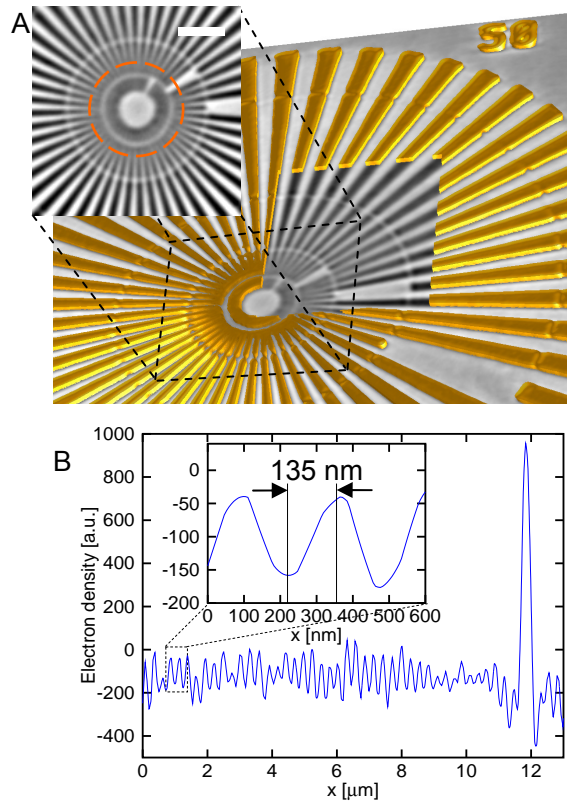
Fig. 4.13 (A) 3D rendering of a lithographically fabricated Siemens star test pattern: the window reveals a single slice from the reconstructed 3D volume and the inset shows the central part of the test pattern (scale bar 2 μm). (B) Profile plot along the circle shown in the inset of panel A. The inset shows a 135 nm half period achieved as lateral resolution in the 3D image.

4.6.2 Comparison of horizontal and vertical rotation axis

As mentioned in section 4.2, we designed our nanolaminography setup at ID22 with a horizontal configuration for the rotation axis. In section 4.2.3, we theoretically studied the influence of horizontal and vertical rotation axis on the fluorescence spectra. We concluded that a horizontal rotation axis is superior for fluorescence measurements. In order to evaluate the two geometries in practice, a comparison was made using a test sample. The sample was a commercial aluminium foil of 50 μm thickness which was imaged at the X-ray energy of 17 keV. The sample was scanned in both laminographic geometries and fluorescence data was taken. The energy spectrum is shown in Fig. 4.14, showing that many impurity elements (Mn, Fe, Ni, Cu, Zn, Ga) besides Al are found in the sample.

Fig. 4.15 shows the Fe fluorescence images from the Al-foil sample. The image shows a plane parallel to the surface normal, summed over one direction in the sample plane. There are several hotspots of Fe visible, which are from particles of various compositions that are found in the sample (for more details, see chapter 5). In Fig. 4.15A the sample rotation axis was in the vertical plane, leading to a long path for the outgoing fluorescence in the sample. In Fig. 4.15B the sample rotation axis was in the horizontal plane, allowing a shorter distance for the fluorescence photons in the sample. Although a different region was imaged for the two measurements, the general differences are very

clear. In the case of a vertical rotation axis, the signal strength drops quickly below the limit of detection, only the first 10 to 15 microns of the sample are seen. In the case of a horizontal rotation axis, the Fe signal is visible throughout the whole sample. This makes it clear that minimizing the path inside the sample is essential for a good imaging of fluorescence from the bulk of the sample.
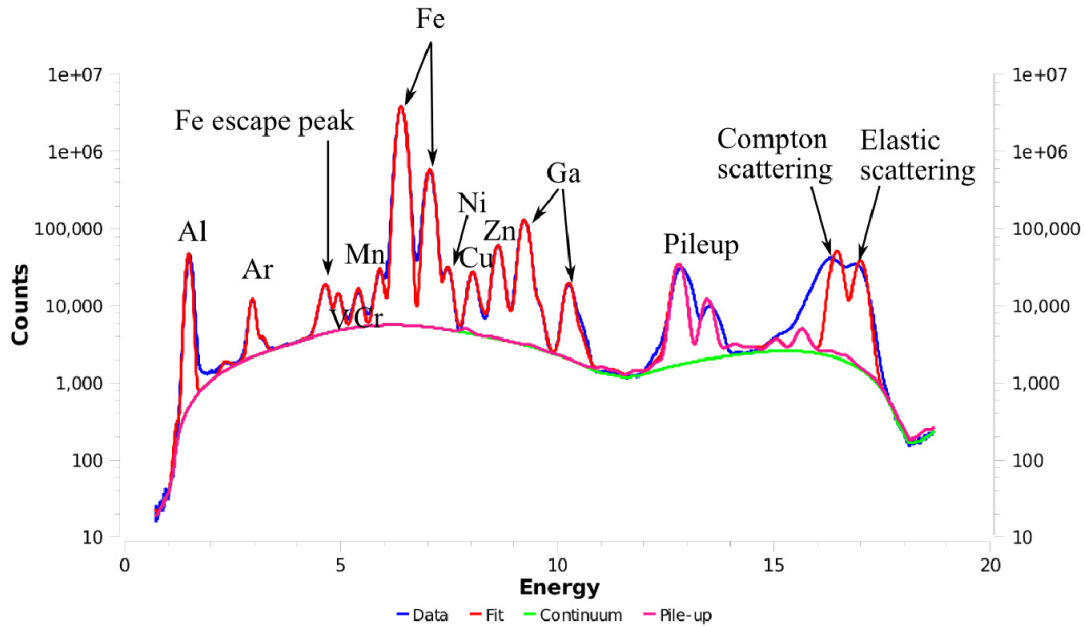
Fig. 4.14 Fluorescence spectrum of aluminium foil recorded at X-ray energy of 17 keV. The blue curve is measured spectrum. The red curve is fitted spectrum. The green curve is background signal. The pink curve is pileup spectrum. Detected elements are marked.
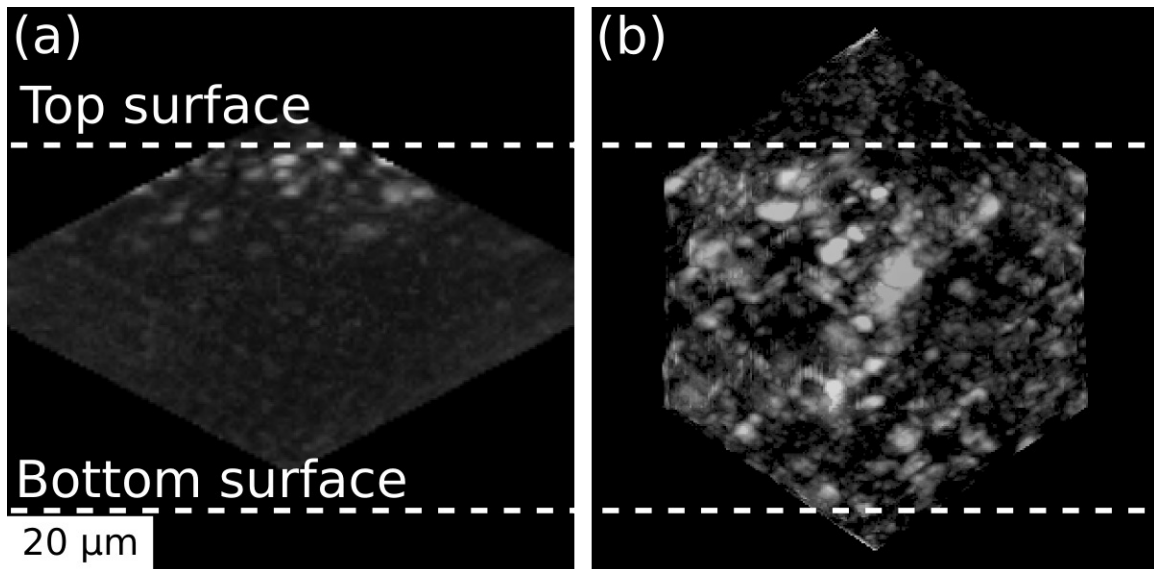
Fig. 4.15 Fe fluorescence images from an Al-foil specimen. The signal from the fully illuminated sample volume was summed, in direction perpendicular to the shown slices, to produce the images. The case for the rotation axis in the vertical plane is shown in (A) and the case for the rotation axis in the horizontal plane is shown in (B). A different ROI was imaged in the two measurements.

4.7 Discussion

Nanolaminography presents presently rather satisfactory results, however, there is space for improvement. One of the biggest challenges is the alignment of the setup. The current Ni ball (100 μm diameter) which is used to measure the laminographic angle is rather large in size for nanoimaging, and its shape is not perfectly spherical in the view of nanoscale pixel size detector. The most time consuming part of the alignment procedure has been to locate the Ni ball in the field of view and to bring the rotation axis to the center of the field of view. This step is especially time consuming for nanoimaging because the field of view is very small. This is because the sample holder is several mm in size, and there are no markers for positioning the Ni ball. Therefore a more sophisticated standard sample has been proposed, as seen in Fig. 4.16. The red lines are made of strong x-ray absorbing materials, such as Fe or Cu. The blue spheres are the ball positions. For nanoscale imaging, the ideal ball should be less than 50 μm in diameter and made from strongly absorbing materials. In the new design, when the sample is put in the beam, we simply move the sample towards the denser direction of the radial structures and we will find the ball of interest in a short time.
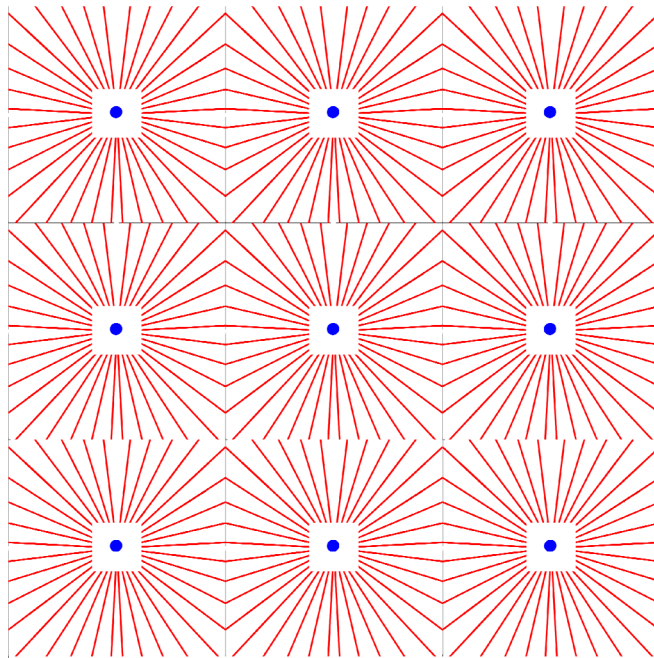
Fig. 4.16 A proposed model for the new alignment sample is shown here. The blue sphere marks the position of the highly absorbing ball. The red lines are line structures made of absorbing materials. The example is shown with 3×3 periods. It can be extended to more periods for practical considerations.

In the following two chapters, experimental results of several applications will be presented. We focus mainly on two fields: materials science and life science. For every example, specific experimental setups and contrast mechanisms will be explained and correlated with the contexts in the earlier chapters.

5 Applications in Materials Sciences

Materials Science covers a broad field of topics related to materials, from the basic research of properties of materials to the applications of materials in practice. Laminography can be applied to study materials in wide range of length scales (from tens of centimetres to tens of nanometres) and using different contrast modes. Studies at macroscopic scales reveal for example cracks inside laminates. Nanolaminography can be used to study microscopic (sub-micron meter) structures in specimens of macroscopic dimension, and to map elemental distributions inside the specimens in three dimensions.

In this chapter we present several examples in materials sciences, using the imaging techniques presented earlier in the thesis. We use X-ray phase contrast laminography to study damage evolution in polymer composites and an Al-alloy under different loading conditions. We study the structure of Pb-free solder bumps under in-situ current and thermal stressing as well as the microstructure and elemental distribution changes in ex-situ conditions. We apply the phase contrast microimaging technique to study the performance of a new flip-chip bonding technique in the manufacture of CdTe based X-ray pixel detector.

5.1 Phase and absorption contrast micro-imaging of polymer composites

Polymer composites are increasingly exploited in automotive and aerospace industry due to their light weight and high strength. Motivated by the demand of developing high performance materials, as required by the applications in these fields, there is a great interest in the investigation of damage evolution, which is a four dimensional (4D) phenomenon. None of the methods used recently, e.g. acoustic emission sensing[109], optical fibre sensing techniques[110], thermography[111], are able to observe the damages directly in three dimensions for composite materials.

In the following we will show that laminographic imaging with SR is a promising technique to study failures in carbon composite materials which allows us to monitor the damage evolution with increasing loading rates. Since the beam time of synchrotron radiation is usually rather limited, the experimental parameters in the imaging process must be pre-examined and optimized in term of image quality, measurement time and radiation doses delivered to the specimen during the experiment. With help of partial coherence of the synchrotron radiation beam, phase contrast laminography can be applied. The *in-situ* experiment of micro-imaging of the formation and propagation of damage-induced defects in a $70 \times 60 \times 1$ mm³ panel made of polymer composite and applied with different loads has demonstrated the potential application in materials science.

In this section we demonstrate the high potential application of SR-CL in non-destructive testing field – the *in-situ* study of damage in polymer composites at engineering length-scales. The content has been previously published by us in Journal of Synchrotron Radiation[112].

Experiments were carried out on ID19 at the ESRF using a monochromatic X-ray beam at energy of 20 keV. A detector based on a charge-coupled device (CCD) (the ESRF in-house development Frelon 2k[113]) with a 2048×2048 pixel array provided a pixel size of 0.7 μm by use of optical lens coupling to a thin-film of crystal scintillator[114] and a square

field of view of 1.4 × 1.4 mm². 3D data sets with an isotropic voxel size of 0.7 μm were reconstructed using a filtered back-projection algorithm under various combinations of experimental parameters. Phase contrast was necessary to distinguish the polymer matrix and carbon fibres because they have low contrast in absorption. To facilitate 3D segmentation of the crack structure by imaging the 3D distribution of the refractive index decrement, one could apply holographic laminography[51,103], using phase retrieval from several specimen-detector distances. However, in order to reduce the X-ray irradiation dose delivered to the specimen we employed phase retrieval using a single detector-to-sample distance[34].

The material investigated in this work is a commercial prepreg, carbon fibre-epoxy unidirectional composite (Hexcel HexPly M21), with a ply thickness of approximately 250 μm. A [90/0]s laminate was produced using the manufacturer's standard consolidation process, resulting in a total specimen thickness of approximately 1 mm.

The laminographic angle between rotation axis and X-ray beam is an additional experimental parameter (compared to CT) which has to be adapted to the sample geometry and structure. Additionally we explore how the number of projections and exposure time per projection can influence the image quality.

As discussed before, the laminographic angle plays an important role in Fourier domain sampling. Two scans were made on the same sample at $\theta = 65°$ and $45°$, keeping other experimental parameters the same. After reconstruction, typical cross-sectional slices (containing both sample and air) were carefully selected from approximately the same position by use of normalized cross correlation [Fig. 5.1(a) ($\theta = 65°$) and (b) ($\theta = 45°$)]. A continuous scanning mode was also adopted at $\theta = 45°$ as shown in Fig. 5.1(c). In Fig. 5.1 the reconstructed greyscale values obtained from a red profile lines (CD) are also plotted as a function of distance (pixel number). The contrast is the highest in (a), however, its artefacts appear most pronounced. To quantify this, standard deviations (Std) are measured over two homogeneous regions (where no specimen structures are present) of air, A, and a resin-rich region, B. The Std values of A and B in (a) are 0.05 and 0.06, respectively, whilst the Std of A and B in (b) are both 0.02. This seems puzzling since theory predicts less imaging artefacts for larger θ angles. This unusual behaviour can be explained by considering two specimen volumes in real space: 1) volume being illuminated at all projection angles and 2) volume being illuminated at some but not all projection angles, see the Fig. 2.9(a) and (b). The ratio R of the total volume (illuminated at least once, illustrated as light grey) over the volume illuminated by all projections (shown as dark grey) depends on the laminographic angle θ as :

$$R = \begin{cases} \dfrac{(\sqrt{1+\cos^2(\theta)} + r\sin(\theta))^3 - (\sqrt{1+\cos^2(\theta)})^3}{3\cos^2(\theta) - 2\cos^3(\theta) - (1 - r\sin(\theta))^3} & (r<1, 0<\theta \leq \arccos(\frac{1-r^2}{1+r^2}) \; or \; r \geq 1, 0 < \theta < 90°) \\[4mm] \dfrac{(\sqrt{1+\cos^2(\theta)} + r\sin(\theta))^3 - (\sqrt{1+\cos^2(\theta)})^3}{3r\sin(\theta)\cos^2(\theta)} & (r<1, \arccos(\frac{1-r^2}{1+r^2}) < \theta < 90°) \end{cases}$$

$$(5.1)$$

where $r=t/a$, t denotes the specimen thickness and a is the lateral dimension of the detector's square field-of-view. Here the specimen is assumed to be perpendicular to the rotation axis and centred with respect to the imaging geometry. For a given r, R is a

monotonically increasing function of θ. For the particular case of $\theta = 45°$ and $\theta = 65°$ we calculated $R = 5$ and $R = 11.5$ ($a = 1.4$mm, $t = 1$mm), respectively, in other words, for thick samples (compared to the detector window a) and large values of θ, more artefacts will be created from the parts of the illuminated ROI which move in and out of the beam during the scan. This is in analogy to CT with truncated projection data (sometimes called local tomography) where the impact of artefacts depends on the size of the truncated part of the projections (*i.e.* beam width minus the sample diameter in case of cylindrical sample geometry).
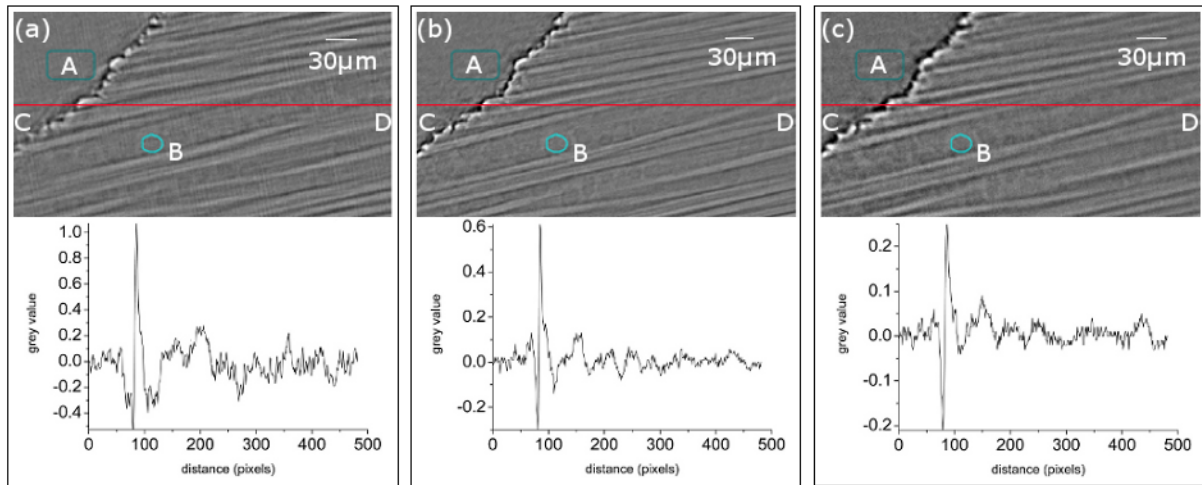
Fig. 5.1 The same slice from 1500 radiographs 200ms exposure time at (a) $\theta = 65°$, stepwise scan; (b) $\theta = 45°$, stepwise scan; (c) $\theta = 45°$, continuous scan. Region A is air. Region B is resin-rich area. The plots correspond to the image values along the red horizontal profile lines, CD.

Instead of the stepwise scanning (each exposure is taken at the break of the specimen rotation), the quick scanning mode can be adopted. This mode employs continuous scanning and collects data on the fly of sample stage. However, the disadvantage is clear: the object structures not exactly on the rotation centre will become blurred, which results in an increase of overall artefacts levels. The motor instability is also a concern. In our experiments, when 1500 angularly equidistant radiographs at a 200 ms exposure time were taken, the stepwise scan [see Fig. 5.1(a) for $\theta = 65°$ and (b) for $\theta = 45°$] will take around 80 minutes whilst a continuous scan [see Fig. 5.1(c) for $\theta = 45°$] only takes about 15 minutes. The Std of A and B in (c) are 0.01 and 0.02, which are very close to those of (b). The reconstructed values along the red profile line in Fig. 5.1(a), (b) and (c) are plotted to give an indication of the signal-to-noise ratio. In a compromise of noise/artefacts and contrast, the stepwise scan at $\theta = 45°$ clearly displays the best image quality.

To investigate their effect, SR-CL was applied to measure polymer composites, A series of stepwise scans were performed on a same ROI of a sample and images were taken at different exposure times and number of projections. The laminographic angle was set to 65°. Fig.5.2 shows the same reconstructed slice taken under the parameters listed in Table 5.1. The square in the bottom left (B) is a zoom of the small square in the upper left. In all images (a)-(f) cracks are visible. As expected, the image quality differs for different imaging parameters. Two typical homogeneous regions (where no specimen structures

are present) containing air and resin only were selected, regions A and B, respectively. The standard deviations are listed in Table 5.1. For similar scanning time, more projections clearly yield a better quality. For example, the total illumination time of (b) is longer than that of (c), but the standard deviation is greater indicating that the reconstruction quality is worse.
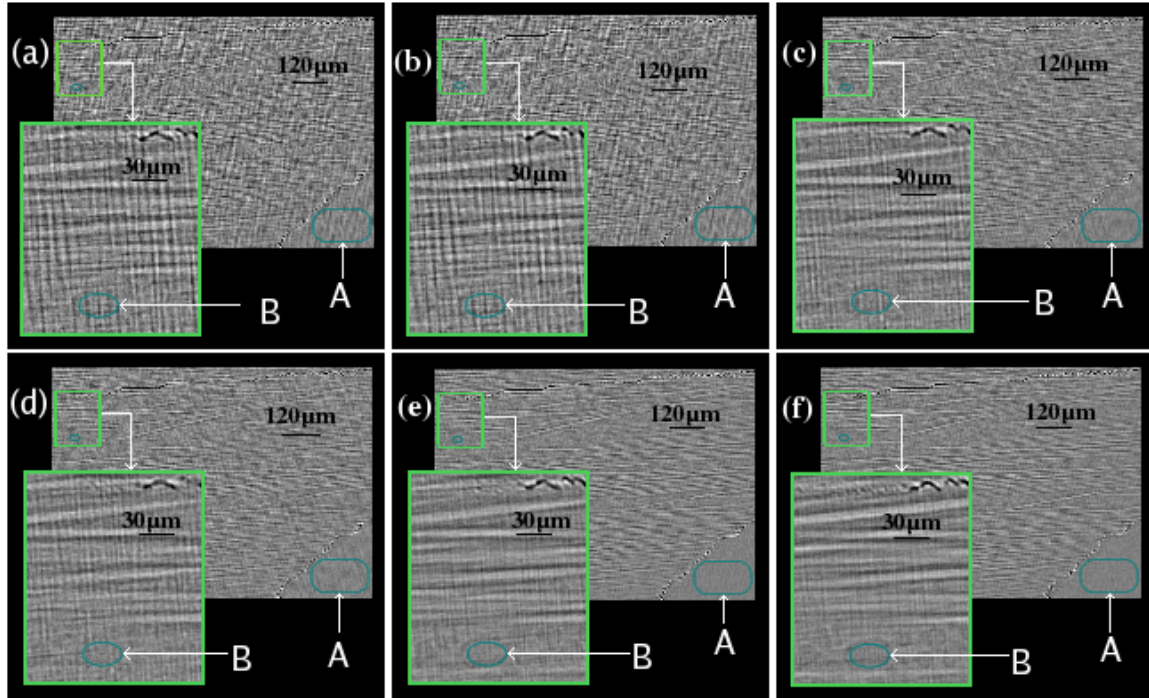
Fig.5.2 Laminographic images collected in the stepwise scan mode at a laminographic angle of 65° for a sample, and at different experimental parameters as listed in Table 5.1. The region A is air and the region B is a resin-rich area.

	(a)	(b)	(c)	(d)	(e)	(f)
Exposure time (ms)	50	100	50	100	100	200
Number of projections	600	600	1000	1000	1500	1500
Std of region A	0.10	0.10	0.06	0.06	0.04	0.03
Std of region B	0.16	0.16	0.11	0.08	0.07	0.07

Table 5.1 Experimental parameters and quantified values of Fig.5.2.

Besides the laminographic angle and the scanning mode, other important parameters influencing the quality of the reconstructed image include exposure time and number of projections[115,116]. These latter two parameters determine the total counting time and hence the experiment time and the irradiation doses delivered to the specimen.

For many load bearing material structures, the characteristic length scale of fracture from cracks and notches can be in the centimetre range and above[117]. Aimed to test the capability of SR-CL, panels of $70 \times 60 \times 1$ mm^3 in size and made of composite were subjected to progressive damages from a deep notch. The fractures around the notch tip were imaged *in situ* via the SR-CL. Fig. 5.3(a) shows that a split initiated and propagated

58

away from the notch. Transverse ply cracks and delaminations were also observed. In order to improve the segmentation quality and better visualise these structures in 3D, phase retrieval using a single detector-to-sample distance which was explained in chapter 2 was applied for reconstruction[34]. In a comparison to the reconstruction in the edge-detection regime, the same slice of the volume reconstructed with phase retrieval is shown in Fig. 5.3(b). In the reconstructions involving phase retrieval, the cracks and splits under different loads could be more easily visualized (simple thresholding for binarisation) in the 3D renderings of Fig.5.4. It is seen that with increasing loads, it is mainly the split and crack 2 which are growing, crack 3 almost stays at the same size. A split can be seen to propagate along a direction with 45 degree due to the notch's shape. Cracks in Fig.5.4 (b) are seen at a length scale of 2 mm, which are larger than the field of view of the detector. Therefore, a raster scan was employed across different lateral positions (adjacent ROIs) which were concatenated afterwards by 3D image correlation techniques. As we see, the entire crack structures can be visualised and examined in three dimensions, across scales and in engineering-relevant coupon sizes that would be inaccessible to a comparable CT configuration.
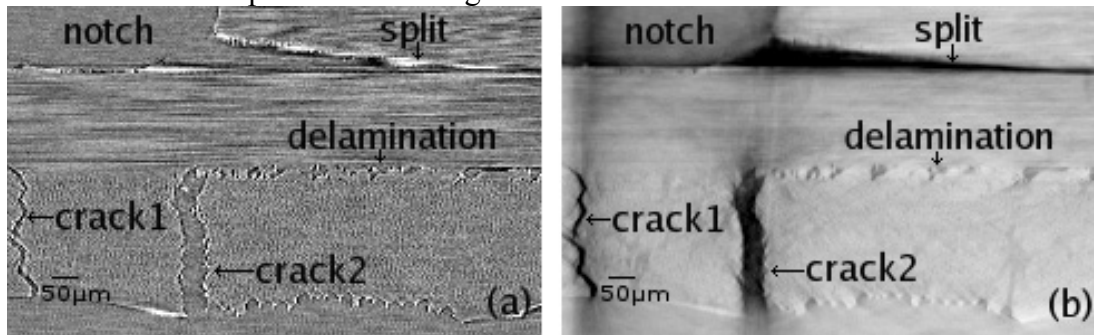
Fig. 5.3 The same cross-sectional slice under *in situ* load reconstructed by SR-CL ($\theta = 65°$) for the edge-detection regime (a) and applying phase retrieval from a single detector distance (b).

The relevant parameters space of SR-CL was examined for the study of such composite materials. It was shown that for the particular sample thickness and spatial resolution (determining the field of view of the detector) chosen, the laminographic angle of 45° offers better overall reconstruction quality than that of 65° and reasons for this were given. For further *in situ* studies and relatively thick composite panels (compared to the detector's field of view), an axis inclination angle of 45° and stepwise scanning with a large number of projections (in the order of 1500) at a low exposure time will allow us to acquire even better imaging quality than those have shown in Fig. 5.3 and Fig.5.4.

In conclusion, it has demonstrated that SR-CL can be applied to image ROI in panels of polymer composites in three dimensions. Propagation-based phase contrast imaging with phase retrieval proved an effective approach for easy segmentation of the damage. As a result, damage induced defects could be identified and interpreted. Large growing cracks can be visualized by combining one or more scans into one large 3D image which can extend to the entire damaged region, whilst high spatial resolution is maintained. Consequently, during *in situ* loading it is possible to follow the defect propagation over a wide range of loads. This study demonstrates that SR-CL can shine a light on the 4D phenomenon of fracture evolution and its mechanisms in a wide range of composite materials.
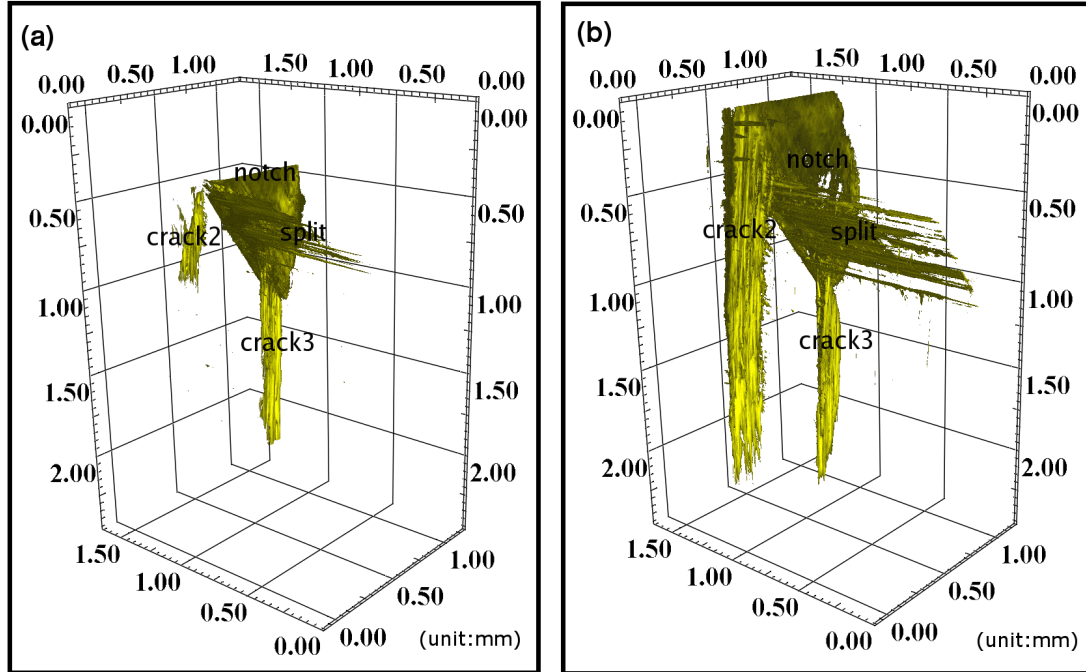
Fig.5.4 The 3D renderings (a) and (b) show the widening of the crack under increasing *in situ* loads.

5.2 Ductile crack initiation and propagation in ductile 2139 Al-Cu alloy studied by absorption contrast and edge enhancement micro-imaging

Micromechanical damage and crack evolution in combination with the microstructure are of high interest in materials science[118–120]. Fracture resistance and ductility are critical design criteria for thin sheet materials in aerospace applications and require in-depth understanding of the underlying physics to enhance material performance[121,122]. Although 2D imaging techniques and 3D tomography have been used to explore fracture mechanisms, the sample geometry was far from ideal engineering conditions. CL is specially designed for large extended thin objects; it offers an opportunity to study the damage mechanisms during crack propagation in advanced engineering materials[123]. It allows an inspection to damage mechanisms for sample geometries that can reproduce stress states similar to those in real service. Here we study the initiation and propagation of ductile fracture in a ductile 2XXX alloy which was used for aerospace applications[124].

The sample was a plate made from commercial ductile 2139 Al-Cu alloy. It was machined symmetrically with thickness varying from 3.2 mm to 1 mm. Testing was performed in the T(long transverse)-L(rolling direction) configuration. The material had an initial void volume fraction of ~ 0.3%[125,126]. The sample geometry is shown in Fig. 5.5. A notch was machined via electron discharge (EDMC) machining resulting in a notch diameter close to the EDMC wire diameter of 0.3 mm. The loading was applied via a displacement-controlled wedging device which controls the crack-mouth-opening displacement (CMOD) of the specimen (see Fig. 5.5).

Experiment was conducted on the beamline ID19 at ESRF with a monochromatic X-ray beam of energy 25 keV. Images were reconstructed using the FBP approach from 1500

60

angularly equidistant radiographs; the exposure time was 250 ms for each projection. The pixel size of the detector was $0.7\mu m$.
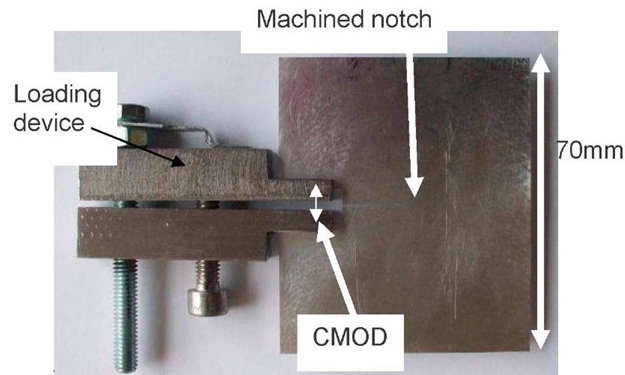
Fig. 5.5 Loading device and 1 mm thick notched plate sample of ductile 2139 Al-Cu alloy. The CMOD is the crack-mouth-opening-displacement of the specimen.

Fig. 5.6 shows 2D sections taken from reconstructed laminographic images at different CMODs. The section is taken at the mid of the bulk of the specimen at every scan. In Fig. 5.6a the machined notch is observed. Fig. 5.6 b-f show the development of damage induced defects, which can be clearly observed by the in-situ experiment. SR-CL allows for unprecedented monitoring of ductile crack initiation and propagation in industrial grade materials at a realistic length scale compared to engineering applications.
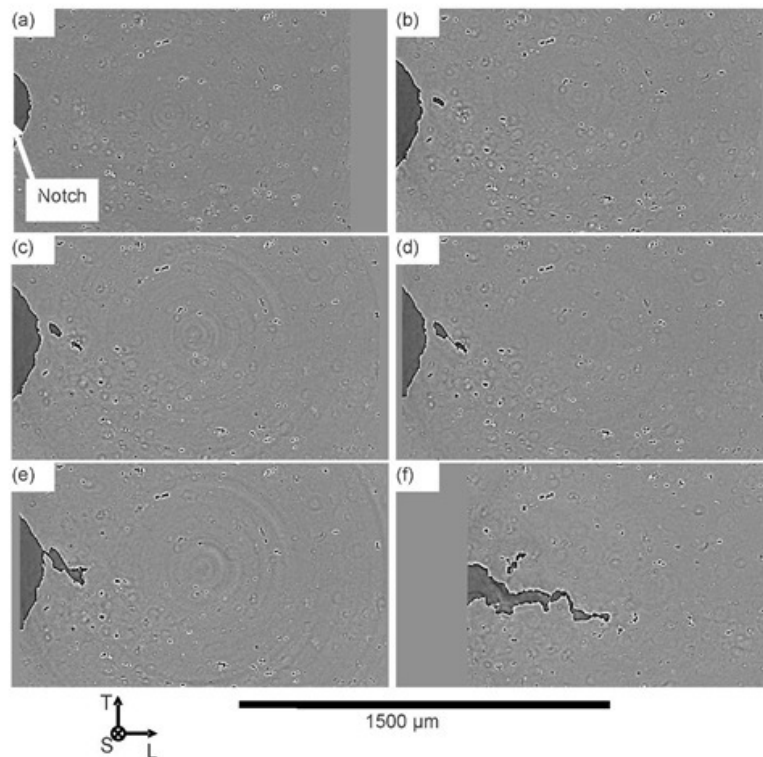
Fig. 5.6 2D slice section at mid-thickness of Al-Cu alloy sheet taken from in-situ SRCL data for a) CMOD = 0.5 mm b) CMOD = 1.5 mm c) CMOD = 1.625 mm d) CMOD = 1.75 mm e) CMOD = 1.875 mm f) CMOD = 2.375 mm.
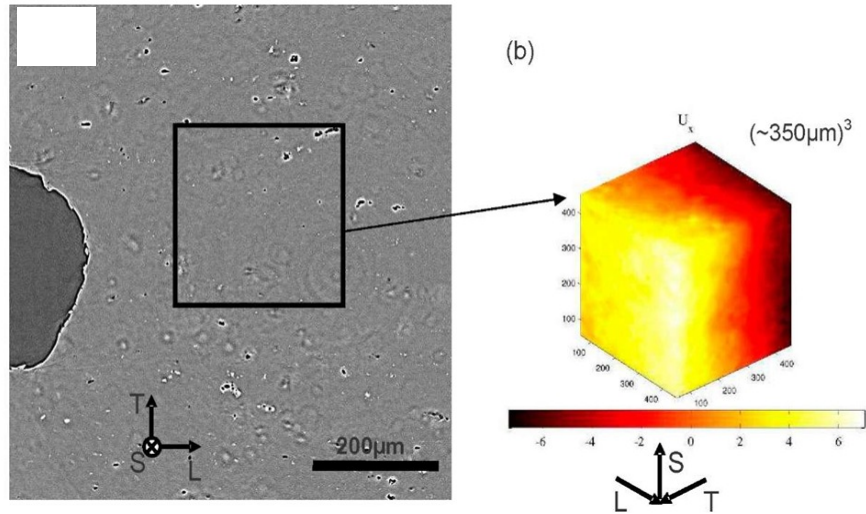
Fig. 5.7 (a) 2D section taken from the laminographic scan of the Al-Cu plate at CMOD = 0.5 mm. (b) Measured displacement field obtained from images of CMOD = 0.5mm and 0.625 mm, the color bar indicating displacements in T direction expressed in voxels.

Fig. 5.7 shows the displacement field by extracting from two images within the squared box indicated in Fig. 5.7a. The reconstructed images of CMOD = 0.5 mm and CMOD = 0.625mm were used. The volume of the compared cubes is taken symmetrically at the sheet mid-thickness. The preliminary result obtained from the present study encourages us to take further loading steps, and to derive strain fields. The measurement may then open a possibility to go insights into deformation field and strain localization mechanisms leading to crack bifurcation.

5.3 Correlative elemental and structural nano-imaging of an aluminum alloy

This is a feasibility study. Linking material structure to the elemental composition is important when studying alloys. To have several elements in the sample gives rise to complex interactions between the element quantities, the material forming conditions, and the subsequent processing. In order to understand the material, it is important to be able to study not only the structure, but to be able to look at also how the elements are distributed. The relevant length scales for structures in such materials are often well below 1 micron, so that high spatial resolution imaging is necessary.

To demonstrate the ability to combine electron density and elemental contrast imaging at the nanoscale, we chose to study a widely used material - aluminum foil. The Al alloy type is AA8079 and the foil was 42 micron thick. The studies were done at ESRF at the beamline ID22, and the laminography setup there has been described in more detail in Chapter 4.

The Al foil was glued on top of a cylindrical sample mount made from a Kapton foil and an aluminium ring. The geometry with vertical rotation axis was used for the experiment. The average incoming photon energy was 17.5keV, and the distances for phase contrast imaging were chosen to give the effective pixel size of 60nm. Exposure time of 1 second per projection was used and 1499 projections were collected over a rotation of 360

degrees at each of the four focus-to-sample distances. Afterwards, the same region of the sample was brought to the X-ray focus for fluorescence imaging. The fluorescence signal was recorded by scanning the sample in 0.5 µm steps over a region of 50 by 50 µm². The step size was chosen to have a sufficient resolution while covering a large sample volume in a reasonable time.

The phase maps revealed that there are plenty of dense particles inside the Al foil (Fig. 5.8). Based purely on the phase contrast images, it would be impossible to guess if the all particles have similar composition or different, the densities of the particles looked similar given the SNR limit of the images. By combining the fluorescence results to the phase contrast images, we saw that the particles were mainly composed of Fe, Ni and Cu, with a varying mixture of elements in each particle.

Fig. 5.9 shows the 3D rendering of phase contrast and fluorescence contrast volumes. Notably, the bottom of the fluorescence rendering appears empty, *i.e.* no fluorescence signals near the bottom. This is due to self absorption of the photons inside the sample. As was explained in Chapter 4 the vertical rotation axis geometry is particularly bad for the self absorption, therefore exaggerating the effect of self absorption. With a more optimized geometry, fluorescence from the bottom part of more than 50 microns thick samples could still be observed.
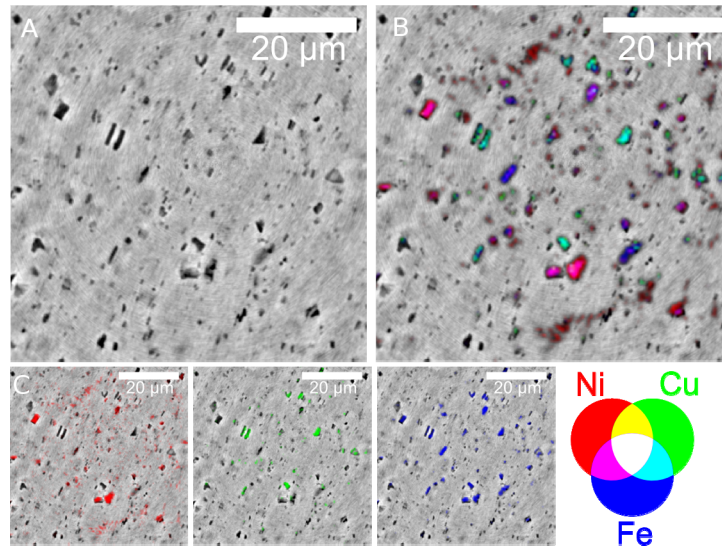
Fig. 5.8 Structure and elemental distribution of Al foil in a single slice of 60 nm pixel size, 3µm below the foil surface. (A) Structure reconstructed from phase contrast images with dense parts showing in darker color. (B) Co-localization of the three elemental (Ni, Cu and Fe) contributions. (C) Images of Ni, Cu and Fe distributions overlapped with the structural images, and the color code.

This example of an Al foil has shown that precipitates, intermetallic phases, impurities etc can be visualized at the nanoscale in 3D without sample destruction. It demonstrates that our method can be used to detect the distribution of multiple elements simultaneously, and that the elemental information can be reliably correlated with the morphological imaging. The quantification of the element concentrations is furthermore feasible in cases where the absorption is homogeneous, i.e. in cases of homogeneous materials with only trace impurities.
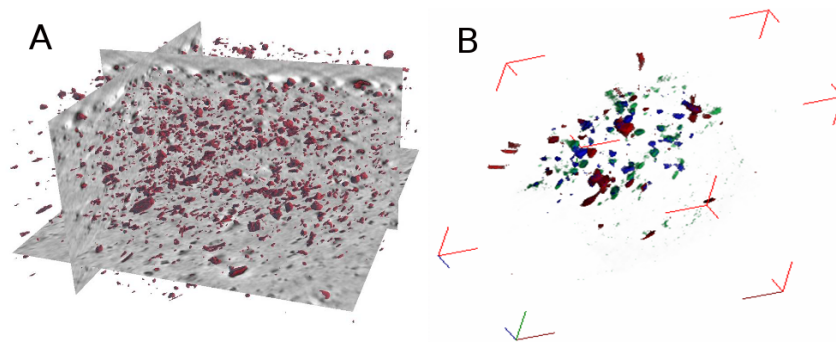
Fig. 5.9 (A) 3D rendering of phase contrast nanolaminography on Al foil. The volume size is 90×90×48μm3. (B) 3D rendering of fluorescence nanolaminography on Al foil. Color code: RED = Ni, GREEN = Cu, BLUE = Fe.

5.4 Microsystem packaging studied by SRCL

Solder has been playing a ubiquitous role for circuitry connection in electrical product[127]. Due to environmental concern, there is a directive to ban Pb-based solders in consumer products by the European Congress on July 1, 2006. At present, nearly all the eutectic Pb-free solders are Sn-based. For a large scale application of Pb-free solder joints, the reliability is of serious concern[128]. Electromigration (EM) has been recognized to be an important cause that is associated with reliability in flip chip solder joints in electronic packaging technology. EM, referring to the atomic motion from the cathode end to the anode under the influence of high electric current density[129,130], can build up compressive stress at anode and tensile stress at cathode, which is well known as back stress. EM-induced melting of flip chip solder joints has been frequently observed and has become a reliability issue in packaging technology[131]. The Al interconnect is the dominant heat source in the flip chip structure. Furthermore, while the applied current density in the bump is about 10^4A/cm^2, the current density in the Al interconnect reaches 10^6A/cm^2, which can cause EM damage in the Al interconnect. The resistance of the damaged Al interconnects can be easily doubled or tripled, leading in turn to corresponding increase in Joule heating as well. This is the underlying reason for the melting of the solder bump. An unexpected phenomenon for EM is that it has induced the formation of voids in the anode region of the Al interconnect[132]. It is of great importance to investigate the process of bump melting and void formation under different current densities for the comprehension of microstructure changes.

Intermetallic compounds (IMCs) induced by EM are also attracting more attention nowadays because of three reasons. Firstly, as the size of solder joints keeps shrinking, the solders become more and more brittle and less resistant to mechanical shocks as IMC grows from submicron size to tens of microns. Secondly, since Cu has a high diffusivity in Sn, more Cu-Sn IMCs will be formed at the anode end due to the polarity effect of EM and more compression stress will be generated[133]. As a result, IMCs can put the reliability of flip chip solder joints at risk and lead to the failure of the whole circuit or even the entire electronic device. This in general is a serious alert for the application of Pb-free solders.

There is a second tendency – 3D integration. For microelectronic devices, the number of 2D integrated circuits (IC) increased from 1 thousand per chip in 1975 to 1 million per

chip in 1990 and from 1 million in 1990 to 1 billion in 2010, closely following the famous Moore's Law[134]. Beyond 1 billion, it is hard to project the future since we are advancing into nanotechnology, and quantum mechanical effects will become more significant; the critical feature size is presently down to 22 nm, approaching the physical limit of miniaturization[135]. Furthermore, economical considerations also become very unfavorable. Thus, the microelectronic industry cannot but look for a new direction to grow and the new direction is 3-dimensional (3D) IC. Today, electronic industry is developing microbumps for through-Si-via (TSV) technology for 3D IC and the diameter of a micro-bump is about 10–20 μm, so the density is about 10^5–10^6 joints/cm^2. This is the new direction of growth or the new paradigm of the future of microelectronic industry. Since the 3D IC structure is new, the details of reliability problems, such as thermomigration (TM), EM and stress-migration, are mostly unknown.

5.4.1 White beam laminography for time resolved imaging of Pb-free solder bumps

At the beamline ID15 at the ESRF, *in-situ* and *ex-situ* experiments were done to characterize 3 types of flip chip Pb-free solders under two different EM testing conditions. The aim of the experiment was to study the generation of voids at an initial stage which were induced by electron. Table 5.2 gives the summary of the sample we examined.

Type	UBM	Solder	Current Density MA/cm^2	Temperature °C
1	Ti/Cu/Cu(7.5um)	SN100C	7.5	130
			10	
2	Ti/Cu/Cu(7.5um)	SAC1205	7.5	130
			10	
3	e-less Ni(5 um)/Au	SN100C	7.5	130
			10	

Table 5.2 A list of solder bumps sample and treatment parameters. Current density is the current density of the bump.

For *ex-situ* experiments, we current stressed six chips at the same time. Around every 13 hours, we took the samples out of the furnace and scanned them using white beam x-ray laminography. Fig. 5.10 shows the schematic diagram of the sample structure. There are two bumps on each sample, the electron flow comes from the bottom of Bump B and then goes through the Al trace on the top of these two solders, finally it goes out of the bottom of the Bump A. Therefore the upper right corner of the Bump A is the entrance point of the electron flow, which is so-called current crowding region. The current crowding region is believed to be the initial site of the void formation induced by EM. After the nucleation of the voids, it will grow through the interface between solder and the under bump metallization (UBM), as the direction of the electron current redistributes As EM is basically a long-term diffusion phenomenon hundreds of hours or more will be

needed until the failure finally happens under typical testing conditions of accelerated degeneration.
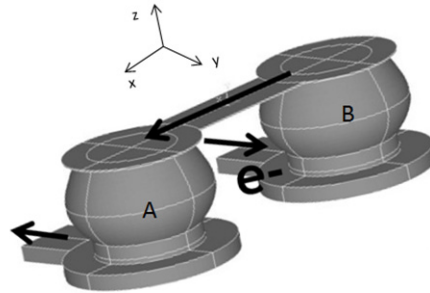
Fig. 5.10 Schematic diagram of the solder bumps structure. A and B are solder bumps. e⁻ represents electrons. The arrows show the electron flow direction.

In our study, we monitored what happened inside testing solders as a function of time to investigate the EM effect at the early stages of damage formation. Fig. 5.11 is an example of 2D reconstructed images of the type 1 sample under 7.5MA/cm^2 electron current powering at 130°C. It shows the evolution of the upper interface between solder body and UBM. Clearly, the results confirm the existence of EM, indicating that the voids were mainly formed from the current crowding point. However, what is unexpected is that there is not only one dominating void existing inside the bump, but also several small voids were formed at the same time. This effect has never been found by previous SEM examinations. The longest EM treatment we used was 77 hours, and at this time there was still no significant change in the electric resistance. Actually the late stage which leads to a real failure would be also of interest, but due to the limited beamtime it was not possible to follow this.
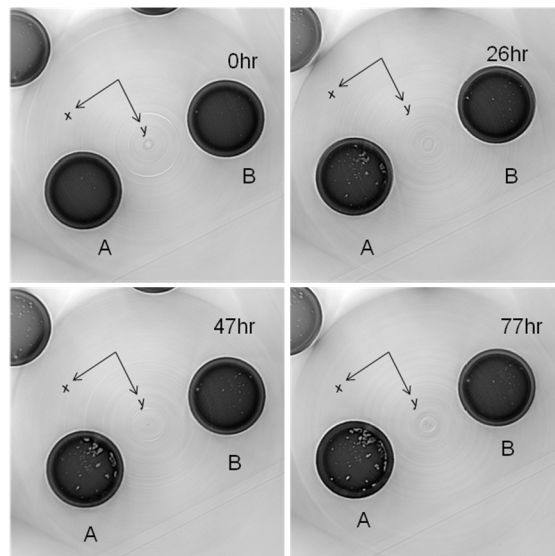
Fig. 5.11 2D reconstructed images of the type 1 sample under EM treated at different times. The times are 0, 26, 47 and 77 hours for a, b c and d, respectively.
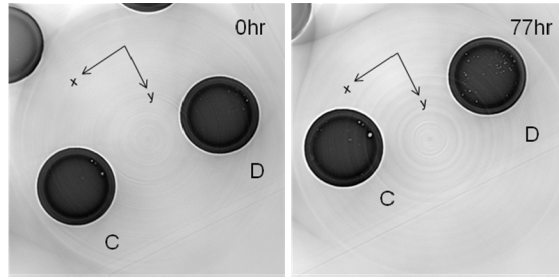
Fig. 5.12 2D reconstructed images of the sample under 130°C thermal treatment.
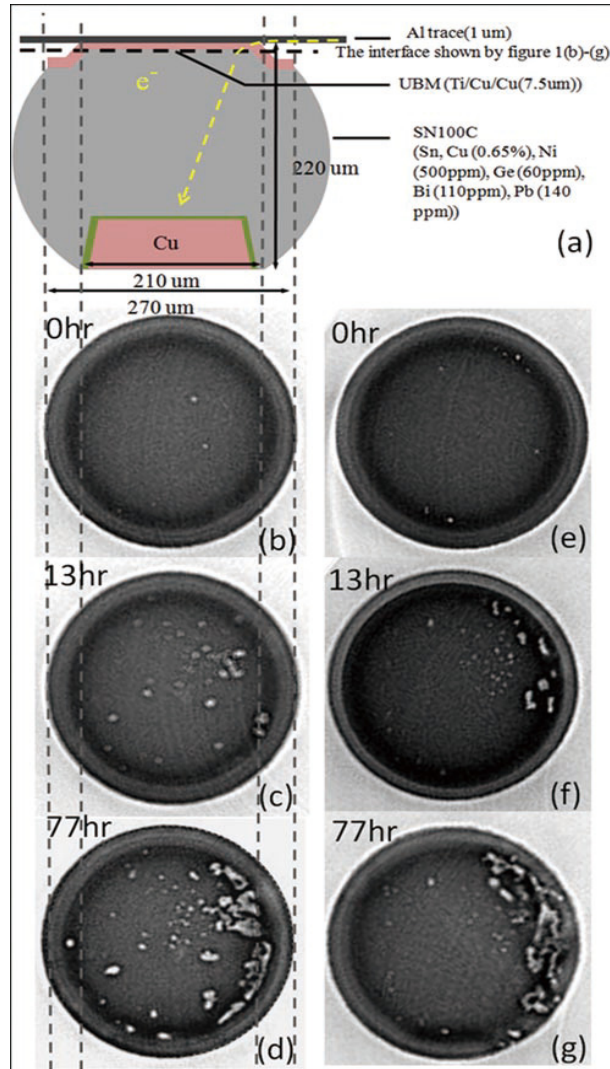
Fig. 5.13 (a) A schematic diagram of the cross-section of the solder joint, showing the configuration and dimensions of the sample. (b)-(d) show the cross-sectional slices reconstructed by SRCL of the sample I at the interface between the solder ball and UBM before, after 13 hr, and 77 hr of EM test, respectively, under a current density of 7.5×10^3 A/cm2 at 130°C. (e)-(g) show cross-sectional slices of the sample II, before, after 13 hr, and 77 hr of EM test respectively under a current density of 1×10^4 A/cm2 at 130°C.

For comparison, Fig 5.14 shows the evolution of the interfaces of two unpowered solder bumps, which were only treated by thermal aging at 130°C. The image taken after 77

hours of heat treatment shows several small voids at the interface, which are not present in the image taken before the thermal aging. This means that the interaction between UBM and solder body can introduce vacancy segregation and thus leads to void nucleation. This finding is new and worth a deeper study, however, it will not invalidate the theory of EM since in this latter case the distribution of voids is clearly random.

Fig. 5.13 (a) is a schematic diagram of the cross-section of the solder joint, showing the structure and dimension of the sample. Fig. 5.13(b)-(d) show the reconstructed cross-sectional images (voxel size $= 0.84\mu m$) of the top-view of sample I, at the interface between the solder ball and UBM, at different time stages of stressing by the current density of 7.5×10^3 A/cm^2 at 130°C. Before EM, there were just two pre-existing voids locating at the top interface (Fig. 5.13(b)). After 13 hrs of EM test, dozens of voids were formed at the interface (Fig. 5.13(c)), some of them kept growing during the stressing (Fig. 5.13(d)). Similarly, Fig. 5.13(e)-(g) show the evolution of voids at the top interface of sample II stressed by the current density of 1.0×10^4 A/cm^2 at 130°C.

Unlike the most popular assumption in previous studies which assumed nucleation of a single void and propagation from the current crowding area, the SRCL results reveal that a group of voids are created on the interface and followed by a rapid growth[136].

5.4.2 Phase contrast and fluorescence nano-laminography for microbump inspection

Laminography is an ideal method for non-destructive imaging of microelectronic devices. The beamline ID22NI at ESRF is capable of making holographic laminography to detect structures and fluorescence laminography to map 3D elements distribution on a nanoscale resolution. By conducting *ex situ* imaging on microbumps under current stressing we aim to quantitatively investigate intermetallic compounds (IMC) formation and void formation/propagation, both of which are of serious concerns for reliability.
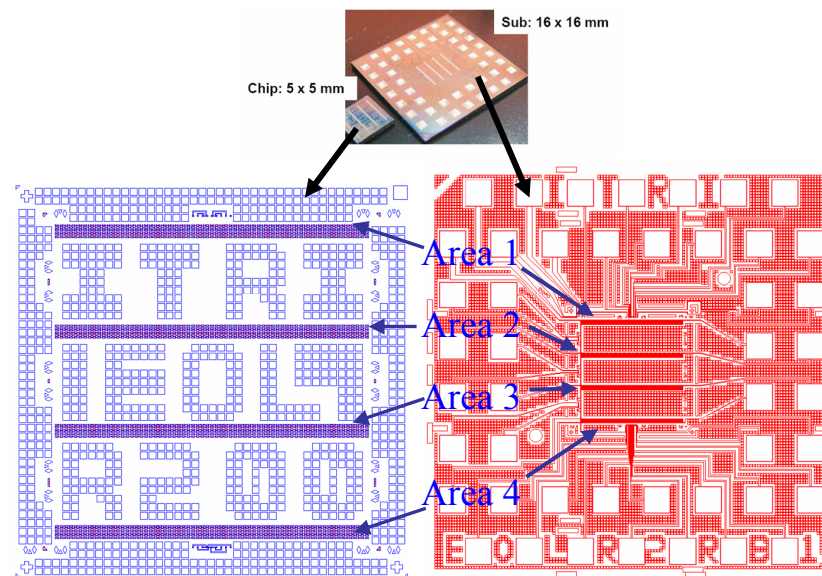
Fig. 5.14 Microbump structure. The substrate is 16×16 mm^2 silicon. The Chip is 5×5 mm^2 in size. On the chip there are four areas with microbumps which have been pointed with arrows as Area 1-4. Each area contains 134 (column)×6 (row) = 804 microbumps.

At the moment, a major paradigm change, from 2D IC to 3D IC, is undergoing in microelectronic industry[137]. In the 3D IC, the challenge for manufacturing is in vertical interconnection, which is made by using micro-bumps to join the TSV chips in stacking. As the size of a microbump is typically 10 μm, just a temperature difference of 1 °C across the microbump, induced by joule heating, will cause a temperature gradient of 1000 °C/cm, which is huge. Similarly, in such a small scale, large gradient forces exist together with stress gradient, voltage gradient, and chemical potential gradient. Compared to the 2D IC structures, the 3rd dimension brings new types of reliability problems, and very little experimental data are available. In the 2D IC, EM and TM have been recognized to be important reliability concerns in flip chip solder joints in electronic packaging technology[130]. In the 3D IC, we started our research with EM related IMC formation and void formation/propagation. The structure of the sample used in our experiment is shown in Fig. 5.14. The microbump size is around 20 μm.
Fig. 5.15 shows the current flow in the area.

In the experiment at ID22, we performed holographic laminography and fluorescence laminography on as-received and current stressed microbumps. The result on the as-received sample is shown in the Fig. 5.16. (A) is a cross section of the reconstructed phase contrast volume. (B) is 3D rendering of phase contrast laminography. (C) is from the 3D fluorescence laminography. We were able to distinguish the microstructures and map 3D elements distribution. In the current-stressed microbump, we observed IMC formation and void formation/propagation. Next step is to measure initial information of the current stressed bump by *ex-situ* technique in order to make quantitative analysis of the voids growth.
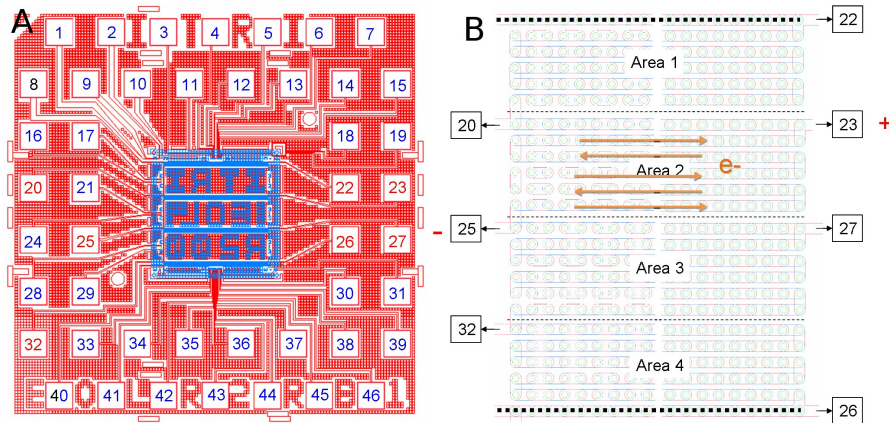
Fig. 5.15 (A) Daisy chains of the microbump. (B) One example of current flow through the microbumps in the central blue part of (A) where the microbumps are located.. Pad 23 is connected to anode and pad 25 is connected cathode. Four areas containing microbumps are identified.

We also imaged thermal cycled samples. As these thermal cycled samples have been cut out for testing, tomography was used. Fig. 5.17 shows reconstructed 2D holographic tomography slices of two adjacent microbumps after thermal cycling. Morphologies at different depths in the bulk of microbumps are distinguishable.
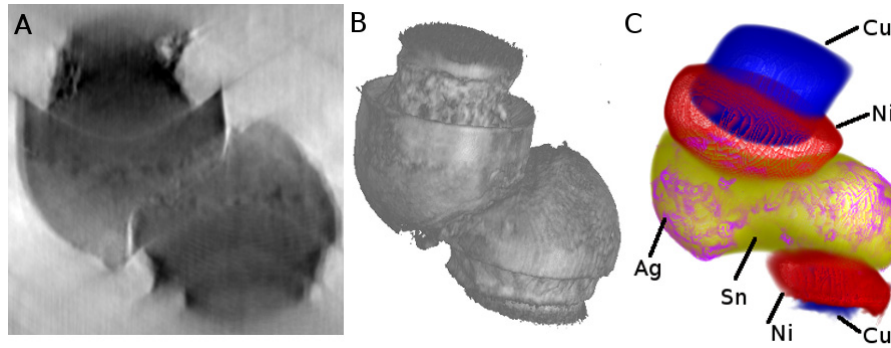
Fig. 5.16 SRCL results of as-received microbump (A) 2D reconstructed phase contrast slice, (B) 3D rendering from phase contrast laminography (C) 3D rendering from fluorescence laminography, different elements Cu, Ni, Ag and Sn are indicated. The two half bumps of the bump are misaligned from manufacturing.
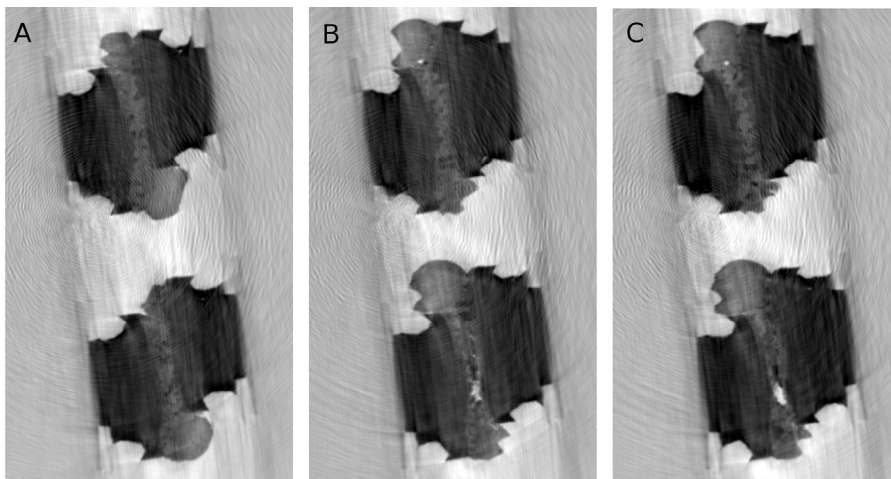
Fig. 5.17 Reconstructed 2D holographic tomography slices of two adjacent microbumps after thermal cycling. A, B and C are at different depths.

5.4.3 Flip-chip interconnections in Medipix detectors studied by white beam laminography

Background

Medipix photon counting pixel detectors are considered of significant importance for synchrotron radiation experiments[138]. Currently, the attention of the research is focused on the development of high atomic number (high-Z) semiconductor based photon counting detectors to extend the energy applicability up to 150 keV. In particular CdTe and GaAs are being considered as a valid alternative to silicon which has a low-Z. One of the most delicate points during the fabrication of a CdTe pixel detector is the choice of a suitable flip-chip interconnection technique. The typically used temperatures (200°C - 350°C) may reduce the semiconductor resistivity by several orders of magnitude[139–141]. Moreover, thermo-compression based techniques can not be used because the mechanical stress induces local changes of crystallographic and electrical properties of the sensor material. Based on these facts, an innovative flip-chip bonding technology has been developed at the *Freiburger Materialforschungszentrum* (FMF) for guaranteeing a low temperature handling and minimised pressure on the detector material. The method is

70

based on a flexible process, which permits the use of an eutectic In-Sn alloy with a photoresist mask and a reflow temperature equal to 150°C. Further details are available in the paper by Fiederle[142]. During the flip-chip process, defects, such as solder joint displacements, cracks, pores, bridges etc can form. This results in blind spots on the detector, which do not count the photons, and thus severely reduce the detector performance. The origin of the formation of those defects and what possible remedy can be made are still unclear.

We investigated the flip-chip interconnections after the sensor material (CdTe and GaAs) is bump-bonded to the readout board. Due to the thickness of the used semiconductor (1mm) opaque structure and lateral extension, the classical optical and ultrasound microscopy techniques are completely inadequate to investigate the bump-bond defects.
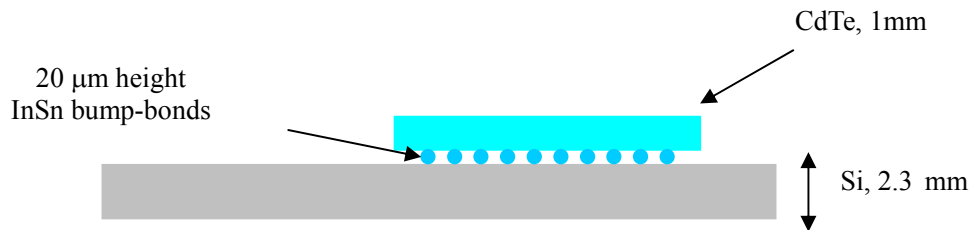
Fig. 5.18 Scheme of the CdTe sensor chip. The light blue block is CdTe die.
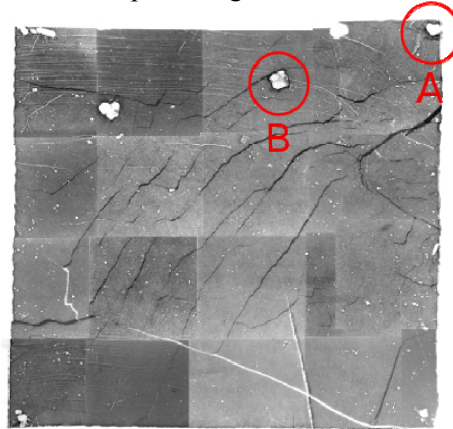
Fig. 5.19 White beam topography mapping of the 1mm CdTe chip. A and B are regions that have been inspected by SRCL.

Experiments and results

Due to the fact that CdTe is highly absorbing material, we chose white beam laminography at the beamline ID15 of ESRF with the peak energy of the spectrum at 90keV. A CCD Dalsa camera of 1024 × 1024 pixels was used with a pixel size of 0.84 μm after magnification. For each laminographic scan, 2400 projections were taken over 360 degree rotation. Due to the high flux in the incoming white beam, a short exposure time of only 50ms per projection was used. The dimensions of the chip are shown in Fig. 5.18. Fig. 5.19 shows a white beam topography mapping of the CdTe chip integrated with a silicon substrate. From the mapping, there are several interesting places with white spots. We imaged regions A and B marked in the figure. Fig. 5.20 is the laminography result of the same chip. From the reconstructed slices Fig. 5.20A and Fig. 5.20B, many voids can be observed inside the bumps.

The example demonstrates that by use of white beam laminography, we are able to inspect the defects of the bump bonding inside medipix detectors. This will help to develop the manufacturing techniques to improve the quality of single photon counting detectors.
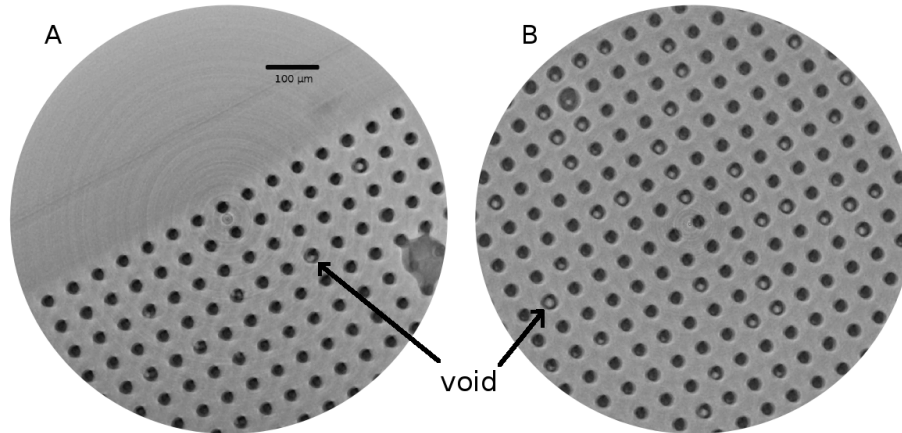
Fig. 5.20 Cross sections of reconstructed volumes from two scans at different regions of the sample. (A) is from upright corner shown in Fig. 5.19. (B) is in middle part.

For a GaAs chip, we conducted the experiments on ID19 at ESRF with white beam laminography with the mean X-ray energy of 60 keV. A total of 1999 projections were acquired over a 360 degree rotation for the laminographic scan. Exposure time was chosen to be 0.6s per projection (Some scans were done with o.5s exposure time due to limited beamtime). Effective pixel size is 0.7 μm and the detector comprises of 2048x2048 pixels. Fig. 5.21 (A) shows a picture of the sample and (B) is a radiograph of the chip. From the image, the details of the bump are not clearly visible. After laminography reconstruction, the bumps are very well resolved. The preliminary results are shown in Fig. 5.22. Further data processing and analysis are undergoing.
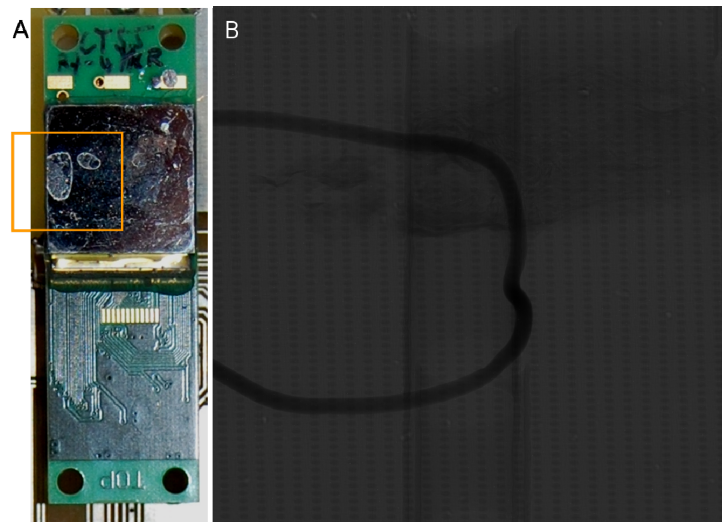
Fig. 5.21 (A) Picture of the GaAs area detector chip. (B) X-ray white beam radiograph of a region in the chip. The radiograph was taken with the chip surface at a 25 degree inclination angle with respect to the beam. Image size is 1.4mm (H)×1.4mm(W). The corresponding sample area is

3.3mm(H) ×1.4mm(W).
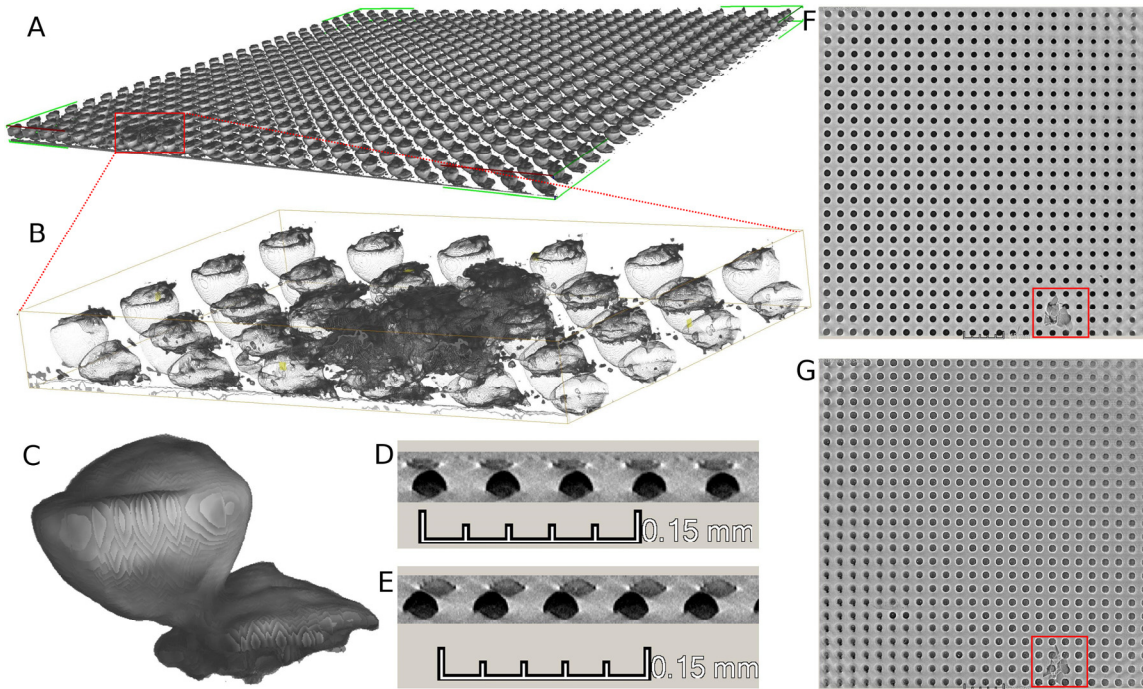
Fig. 5.22 (A) 3D rendering of the solders in the chip. (B) Zoomed region of the 3D rendering from (A) where a defect is found. (C) 3D view of one bump bonding. (D) 2D xz side view of the 3D reconstructed bumps. (E) 2D yz side view of the 3D reconstructed bumps. (F) and (G) 2D xy images of the 3D reconstructed bumps at different depths of the chip from top view, where the defect shown in (B) is marked in red rectangles.

5.5 Discussion

We have applied laminography to inspect material properties in several different applications. The applications have shown new scientific results in cases where other techniques would not have been able to produce good results. The common factor in all of these examples was that the sample had to be kept large for reasons of having realistic surroundings for the region of interest. In the damage propagation studies, the sample was necessary large to allow the damage to propagate freely, without creating artificial boundary conditions by having too small a sample. In the microbump studies several bumps inside a chip could be studied at once, and an intact chip allowed *in-situ* studies. For the example of CdTe pixel detector the large sample was necessary because the bonding quality varied among the pixels, and it was essential to study a large area (not to mention that breaking the detector chip just to take an image would have been quite wasteful).

Despite the successes presented here, there are some challenges remaining, which do not allow all studies to succeed equally well. Mainly these problems stem from the strong absorption of x-rays in some materials samples. Because currently only a setup with magnification of the beam, such as at ID22, can realize nanoscale resolution imaging,

images are naturally obtained with phase contrast. The current phase retrieval techniques suffer from strong absorption, because they have been based on the simplifying assumption that the absorption is weak. If this is not the case, then phase retrieval results will contain artefacts. An example of this is shown in Fig. 5.23 where a vias sample was imaged. A projection shown on the left contains severe artefacts at positions where the pillars overlap, and the resulting 3D reconstruction consequently is of very bad quality.
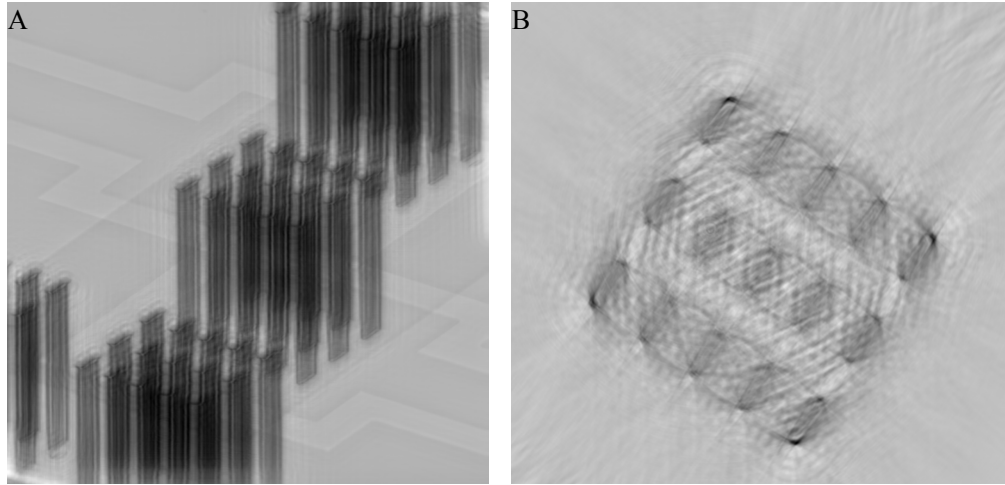
Fig. 5.23 A single phase retrieved image from an interconnect vias sample, the image size is 90μm × 90μm (A), and a slice from the reconstructed 3D volume (B).

The strong absorption is a problem not only for the phase retrieval, but also for the fluorescence imaging. The fluorescent K-edge and L-edge lines are typically quite low energies (below 10 keV often for example), and such photon energies absorb quite readily in the dense materials samples. Therefore fluorescence signal coming from deeper layers of the material is more attenuated than the signal from the surface. This problem is especially difficult for samples with big variations in the local linear coefficient of absorption (such as solder bumps), where depending on the sample orientation the radiation from some part of the sample might reach the detector or it might not.

As a partial solution to the absorption problem in phase retrieval, we have increased the x-ray energies as high as possible within the current setup, which at ID22 is about 29.5 keV. For example the presented solder bump studies have been done with that energy. Another improvement comes by using a blurred average of the four images at each projection angle to normalize away the contribution of the absorption. A more general solution would be to improve the phase retrieval techniques to use the full absorption. For the fluorescence a simple self absorption correction by assuming a homogeneous sample composition and normalizing based on the layer depth works well on types of samples where there aer no big density differences. However, for samples such as the solder bumps a more general approach is required. Such corrections could be included in the iterative reconstruction step as has already been done for CT[83,84].

6 Scientific cases in Life Sciences

Imaging techniques have an important role in solving problems arising in life sciences, both in functional and structural studies, and techniques such as SEM, TEM, MRI and CT have been explored. Imaging gives important information for example about functionality of different proteins, and communication between cells. X-ray imaging can give access to metals in cells and tissues and to crystalline structures that are common in biological systems. Furthermore, imaging of tissue and cell structures in 3D is one prominent use for X-rays.

Life sciences have been one of our main reasons to develop nanolaminography. Nanoimaging in 3D often requires a marginally small sample volume to be used, and it is not easy to choose a suitable region of interest that would be representative of the sample. Furthermore, cells and tissues are importantly affected by their interactions with their neighbours, and thus an isolated cell or a piece of tissue does not necessarily contain all the relevant characteristics as they would have in connection with their neighbours. Laminography gives a solution by offering a possibility to have rather large samples. To be able to study such samples on multiple length scales and to focus on most interesting regions for high resolution imaging, is one of the main benefits foreseen from laminography to the applications of life sciences.

In this chapter, we introduce applications in life sciences, mainly focusing on microstructures and toxicology.

6.1 Paleontology –Microimaging

6.1.1 Introduction

Paleontological findings attract broad public attention. Recently, synchrotron radiation imaging techniques, especially CT, have made a considerable progress in paleontology studies[143–145]. The merit of CT in paleontology stems from its nondestructive capability of imaging fossils inside rocks. This has opened up a completely new world of fossil research. However, some fossil samples are laterally extended. In this case, inhomogeneous transmission from different angles which will bring anisotropic artifacts in the reconstructed 3D volumes if CT is being used.

Here we show examples on how CL can be used to overcome this limitation, and to obtain good results for fossils of laterally extended shapes. The experiments were conducted on the 145m-long beamline ID19 at the ESRF. In the experiments, CL takes advantages of synchrotron sources, such as high flux and collimated beam.

6.1.2 Examples

First specimen for laminography study was a fossil of trilobite collected from China. We used the monochromatic beam of 51 keV at ID19, a beam size of 46.5mm ×10mm. The specimen required rather larger illuminated area in order to image a larger region of the sample. We made two scans of the sample. The sample was translated upward for with respect to the rotation center for the second scan, the images were shown in Fig. 6.1A and B. Before the laminographic reconstruction, every projection from the first scan was concatenated to the corresponding projection of the second scan, by using normalized

cross correlation techniques explained in chapter 3 (Fig. 6.1C). Then the reconstruction was performed on the stitched images. A single slice from the reconstructed result is shown in Fig. 6.1D. This example shows that laminography gives sufficient contrast for fossil style samples. However, this sample does not have much in depth feature.

Next interesting sample we studied is a 125 millions year old insect fossil (Araribe, Brazil) in an 8 mm thick lithographic calcareous sandstone. The fossil insect is found to be close to modern insect Insect fossil Heteroptera Naucoridae (nymph). We imaged the fossil at the beamline ID19. The pixel size was 7.5μm. The main features, such as wing, tendon, fissure and anus are clearly visible (Fig. 6.1E, F). Fig. 6.1E, F are 2D cross sections of reconstructed volumes from different depth to the sample surface. We can see clearly laminography can resolve the 3D features. A 3D rendering of this example is shown in Fig. 6.1G.
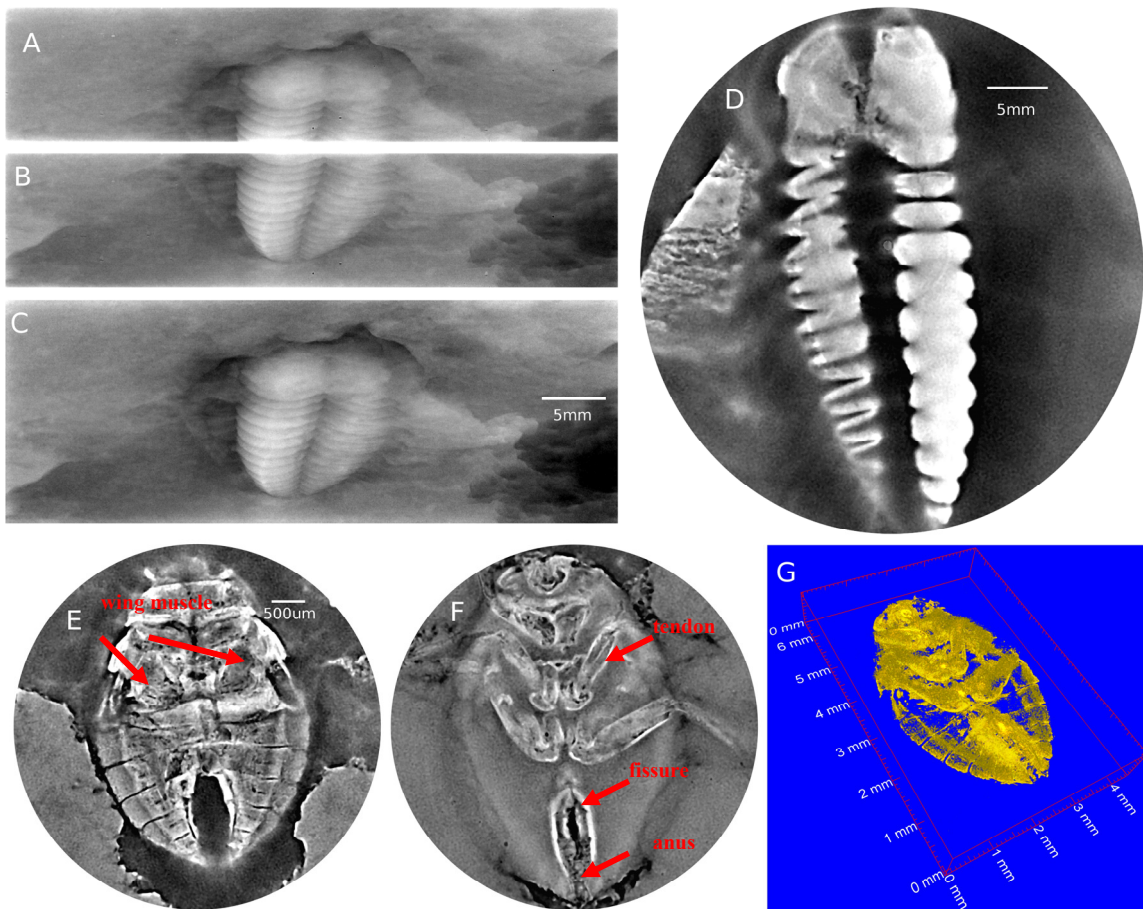
Fig. 6.1 (A) and (B) are flat field corrected projections of specimen trilobite from adjacent ROIs . (C) is stitched image from (A) and (B) by use of 2D normalized cross correlation technique. (D) is reconstructed cross section of sample trilobite. (E) and (F) are 2D cross sections of sample Araribe from different depth. (G) is 3D rendering of sample Araribe.

Furthermore, we studied a sample containing a specimen of *Eupodophis descouensi,* Rage and Escuillié (2000), that was discovered in the Cenomanian of Al Nammoura, Lebanon[146]. The fossil in question is that of a snake, and the specimen size is about 30 × 30 × 3 cm^3. We used a monochromatic beam at 60keV from a Si-111 double crystal

monochromator, which allows a better absorption contrast to be obtained compared to polychromatic beam. The FreLoN camera with the effective pixel size of 30.3 μm was used. A laminographic scan with at the laminographic angle of 30 degrees was made, with a total of 900 projections over a 360 rotation range. The main results are shown in Fig. 6.2. The interesting discovery is that we can not only inspect the visible femur Fig. 6.2B but also from a hidden leg Fig. 6.2C[146].
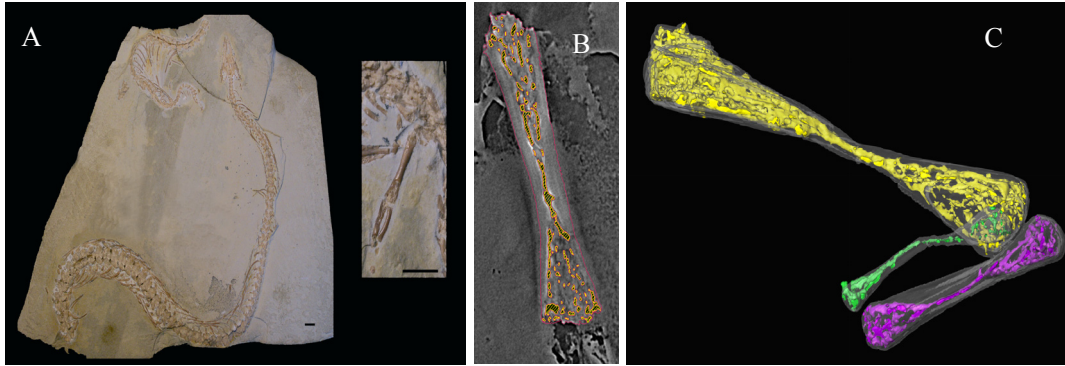
Fig. 6.2 (A) picture of *Eupodophis descouensi*. Scale bars are 1cm (left) and 5mm (right); (B) 2D section of the visible femur. approximate outline of the bone in pink, inner cavities in yellow; (C) 3D reconstruction of the inner cavities of the femur (yellow), tibia (purple) and fibula (green) of the hidden leg.

6.2 SKOV3 Cells - Phase contrast nano-imaging feasibility study

6.2.1 Introduction

Cells and interconnected networks of cells are the basic building blocks of biology. In the feasibility study, we chose to do structural imaging for individual cells embedded in EPON (sample preparation protocol is attached as appendix in this chapter). These include dose resistance of samples and achievable imaging contrast. The cells used in the study were collected from SKOV3 human ovarian cancer cell line, provided by the American Type Culture Collection (Manassas, VA, USA). This type of cells has already been imaged before by nano-x-ray fluorescence, but only in 2D. More details on the cells can be found in the paper[147].

6.2.2 Experiment

The samples were prepared according to the protocol given in the Appendix. The thickness of the sample is 80μm. The laminographic imaging experiment was performed at the beamline ID22NI of ESRF. The laminographic setup used for this experiment is different from what has been shown in chapter 4. The rotation axis of the laminography setup was in the vertical plane, as shown in Fig. 6.3. The laminographic angle was set to 30 degree. We acquired 1000 projections over 360 degree rotation by continuous scanning. Photon energy was 17.5 keV and exposure time was 300ms per projection. Four focus-to-sample distances, giving 60 nm pixel size, were used in order to perform phase retrieval. The phase retrieval method was described in chapter 2.

6.2.3 Results

The reconstructed results are shown in Fig. 6.4. The image in gray scale (A) is a 2D cross section of the reconstructed volume. (B) is coloured 2D phase image of the same slice as in (A). The 2D images show that our technique allows inspection of inner cellular structure. Fig. 6.4 (C) shows a volume rendering of the cells.

This test imaging of cells has revealed three important factors: i) using phase contrast it is possible to get sufficient contrast to see structures inside the cells; ii) the dose to the sample is still small enough to enable good image quality without visible effects from radiation damage, and iii) the variable magnification and resolution can allow us to image an intercellular network, and then to focus on the most interesting details of the sample by zooming in the image at the particular area.
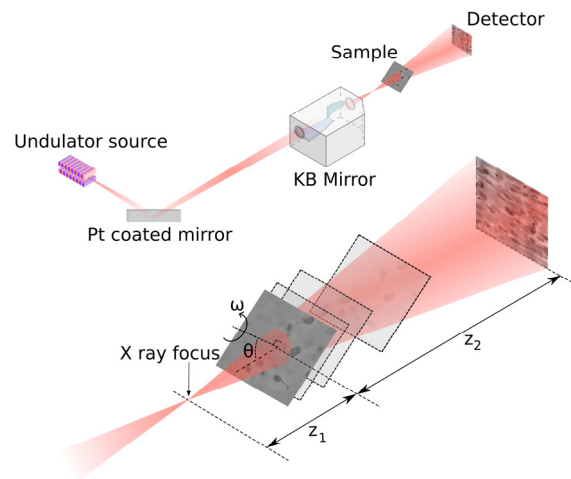
Fig. 6.3 Schematic layout of the setup used for the measurements of cells. The laminographic angle was 30 degree. Four sample focus distances were chosen for z1 to have pixel size of 60 nm.
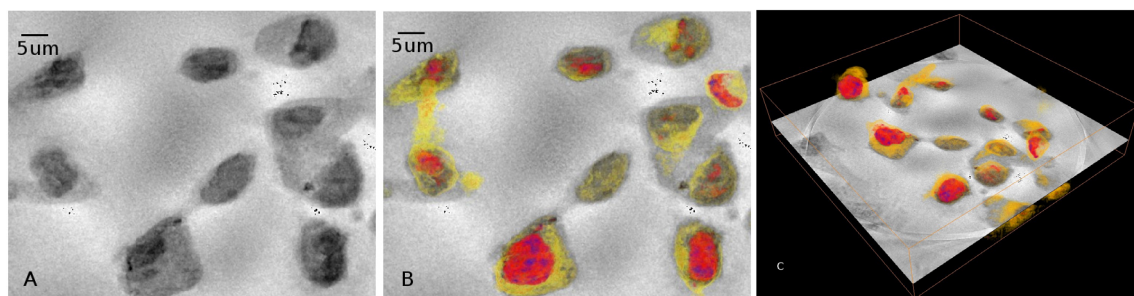
Fig. 6.4 (A) 2D reconstructed phase image in gray level of cells from laminography scan. (B) Coloured 2D phase image of the same slice as in (A) to make the detailed inner cellular structure visible (C) Volume rendering of the cells within a volume of size $90 \times 90 \times 21$ μm^3.

6.3 Photonic structures in insects - Phase contrast nano-imaging

6.3.1 Introduction

Visualization of inner structures in three dimensions is of significant importance for biological materials. Biological materials originate from biological processes, and are adapted to certain functions at various environments. Their structures are often optimized for a specific purpose via long process of evolution, exhibiting unique and interesting properties. The study of these materials is of great interest for the understanding of biology in general, and also for biomimetics, taking inspiration from the nature by understanding and copying the properties of biologic materials to fabricated materials.

Biological materials are often nanomaterials, i.e. having relevant features at length scales below 1 micron, and as such nanoimaging is required for the study. Due to very low density contrasts in most of biological materials, phase contrast imaging is essential for X-ray imaging. Since biologic materials are often not very resistant to high dose irradiation, low dose imaging with phase contrast is necessary for the imaging of such materials.

One particular case of environmental adaption is photonic structures in biological materials[148–151]. This is a nature's way of playing tricks by developing many intricate 3D structures to reflect light in particular ways. As an example, the wings of butterfly Argyrophorus argenteus have been studied. An argenteus has a broadband silvery reflection in the wing that is caused by the nanostructure inside the wings[152].
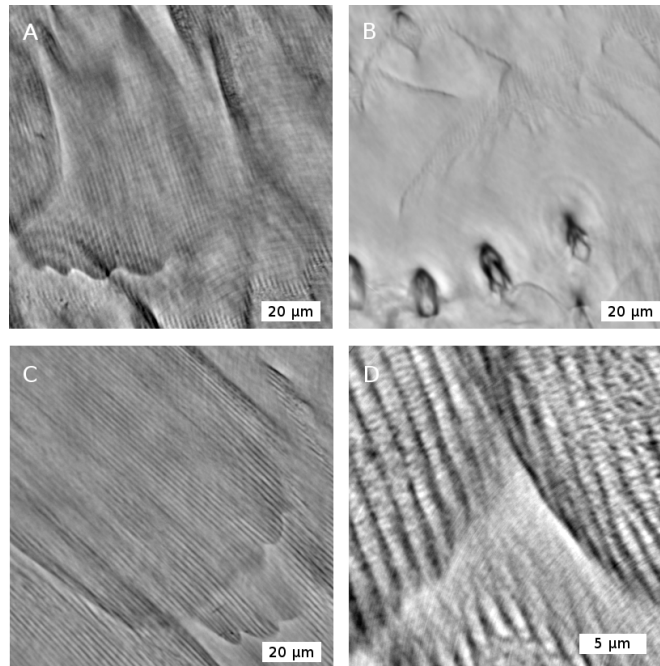
Fig. 6.5 2D cross sections from the phase contrast laminography of butterfly wing. A, B, C are from different positions of the butterfly wing. D is a close-up view of the periodic structure of a few hundred nm period which makes silver colour.

6.3.2 Experiment

Laminographic method was applied to image the inner structure. A rather large piece of the wing ($7{\times}7$ mm^2) was placed between two silicon nitride frames used as supports. The X-ray energy is 17.5keV. Pixel size was 60nm.

6.3.3 Results

A small region within the wing was imaged, and the reconstructed slices from the reconstructed results are shown in Fig. 6.5. Slices show the photonic nanostructure which results in the characteristic silvery colour of the Argenteus butterly. The periodic length in the axial direction is around 560 nm. Fig. 6.6 shows a 3D rendering of reconstructed volume from the butterfly wing. The photonic nanostructure could be thus viewed with negligible sample preparation (cutting a piece of the wing with scissors) using nanolaminography. We believe this successful demonstrative experiment will open up a new application field in natural photonic effect studies.
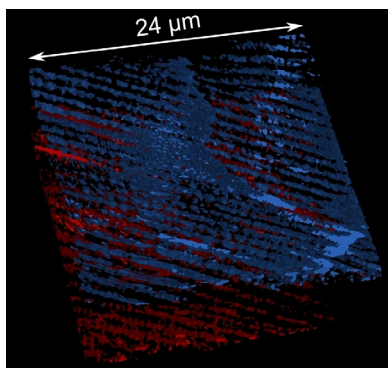
Fig. 6.6 3D rendering of butterfly wing reconstructed volume.

6.4 Structure and metal trace distribution in Zebrafish – nanolaminography and 2D fluorescence imaging

6.4.1 Background

Visualization of element distributions in animal organisms provides unique insights into the understanding of biological molecular networks. Zebrafish (*Danio rerio*) is in many ways a useful model for vertebrate development[153,154]. We applied X-ray fluorescence imaging at high spatial resolution to visualize distribution of metal and non-metal elements in the embryonic stage of zebrafish. We examined the correlation between anatomical structures and element distributions in the embryonic zebrafish retina and brain, at considerably higher spatial resolution than that has been reported before[155]. We conducted two separate studies: i) effect of toxic elements on the development, and ii) a study on genetically modified zebrafish that modeled a pigmentation disorder.

6.4.2 Experiments and results

Zebrafish at toxic stress

The zebrafish were exposed to a mixture of As/Cd/Hg/Pb solutions during the embryonic development (details of the preparation protocol are given in Appendix). The fish were embedded in EPON at 2 days post-fertilization (2dpf), and semi-thin sections (10 μm) were cut out for analysis with x-ray fluorescence. The results from the fish exposed to the elements were compared to control fish that had developed under similar conditions, except the additional four element solutions.

In the control fish, we found layer-specific distribution of elements in the development of the zebrafish retina. A spectrum of the fluorescence signal from zebrafish control sample is shown in Fig. 6.7. Interestingly, the element distribution seems to precede anatomically discernible layer formation. Sr (strontium) was localized in the inner layer of the retina, whereas Ni and Mn were found in the outer layer (Fig. 6.8). Fig. 6.9 shows different elements distribution in the 2dpf wild type zebrafish. Fig. 6.10 shows quantitative element composition of a zebrafish sample in different tissues in eye and brain regions.

In order to combine structural information with the elemental composition, we performed low resolution phase contrast laminography to inspect the whole sample (Fig. 6.11). Then we zoomed in the eye part to make high resolution phase contrast laminography (Fig. 6.12). Furthermore, we did 2D fluorescence projection on the same eye region where the high resolution 3D phase contrast laminography was done. We used a step size of 350 nm for 2D mapping. Distributions of elements such as Br, Ca, Cl, Cu, Fe, Ni, Mn, Se and Zn are mapped. We could correlate the reconstructed 3D phase contrast image with the 2D fluorescence mapping (Fig. 6.12). It shows that it is indeed feasible to detect the trace elements in the embryo at a sufficient sensitivity and a high spatial resolution, with some of the structures being less than one micron in size.
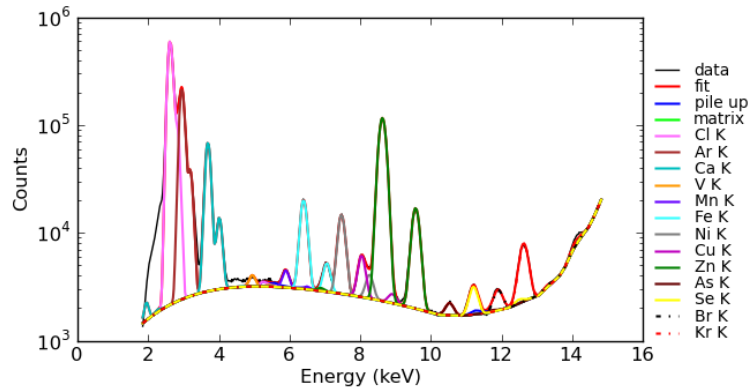
Fig. 6.7 Spectrum of the fluorescence signal from zebrafish control sample.
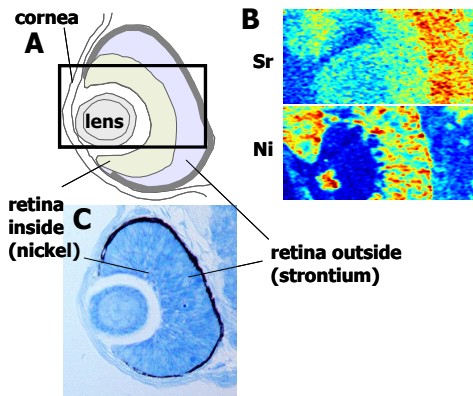
Fig. 6.8 (A) A scheme of zebrafish eye structure (B) 2D hard x-ray fluorescence images of a 2dpf zebrafish eye sample showing the mapping of Sr and Ni. (C) Light micrograph of a stained 5 μm thick 2dpf zebrfish eye sample.
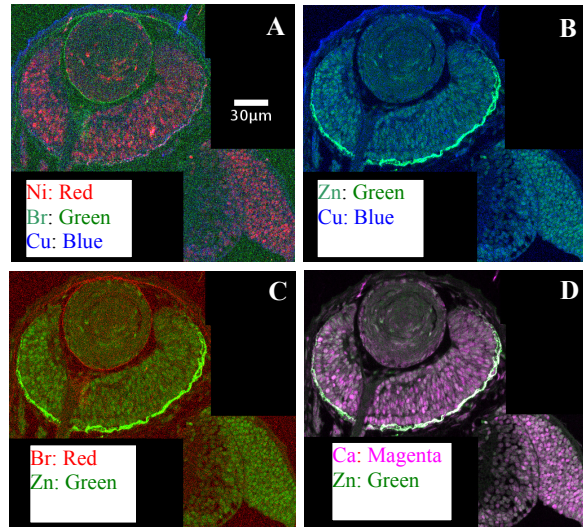
Fig. 6.9 Fluorescence overlaid images from wild type sample showing the mapping of Ni, Br, Zn and Cu. A, B C and D are overlaid images of different elements as indicated in each panel. Sample thickness was 5μm. Step size was 0.5μm. Dwell time was 100ms. Colour scales are independent.
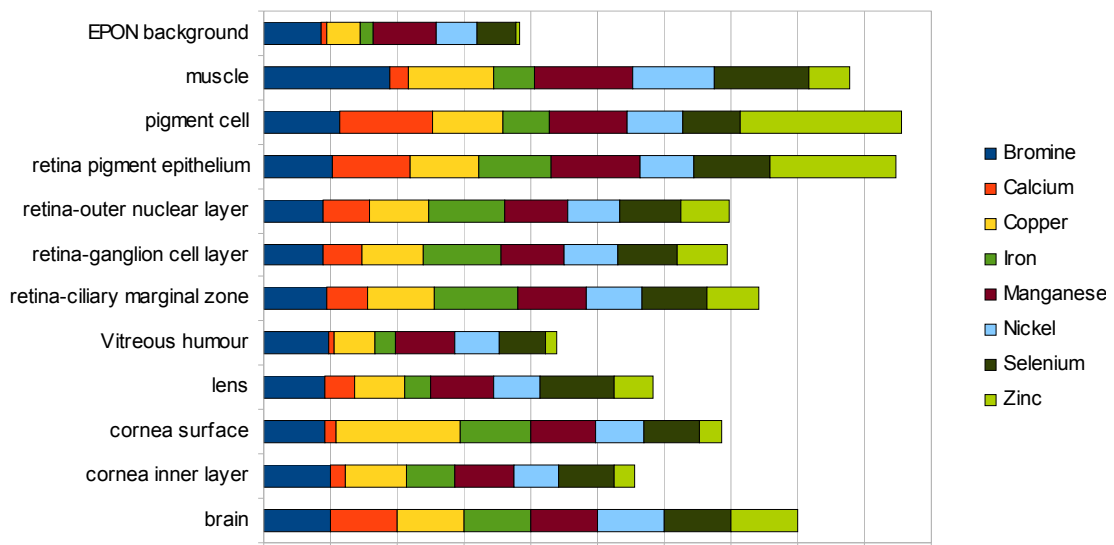
Fig. 6.10 Element composition of each tissue (relative to that of brain) from a control zebrafish sample.

Fig. 6.11 3D phase contrast cross section of 2dpf wild type zebrafish. The sample slice is 12.5 μm thick. Pixel size was 274nm.
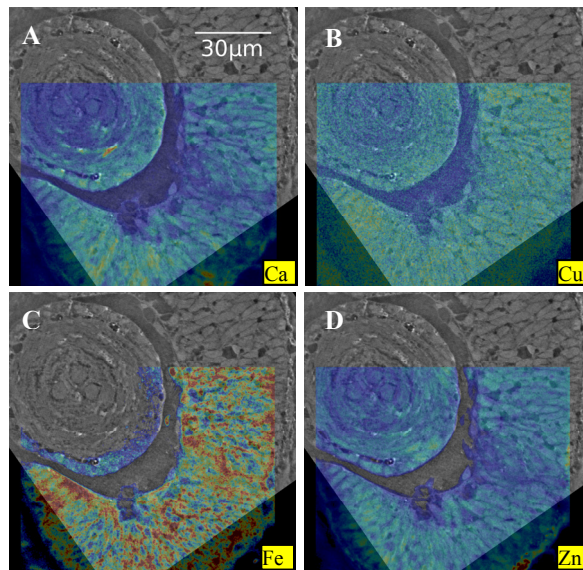
Fig. 6.12 Phase contrast (gray) and fluorescence image (colour) from the control fish sample. The thickness of sample slice was 12.5μm. For phase contrast laminography, the pixel size was 60 nm. For fluorescence imaging, the step size was 0.35μm and the dwell time was 100ms. Colour scales are independent.

The other group of zebrafish was exposed to environmental toxicants As_2O_3 /$CdCl_2$ /CH_3Hg /$PbCl_2$ during embryonic development. The heavy metals were specifically localized at some tissues. As, Cd, and Pb were mainly accumulated in the retinal pigment epithelium (Fig. 6.14), whereas Hg was seen in the lens. For the controls, eight

endeogeneous elements (Br, Ca, Cu, Fe, Mn, Ni, Se and Zn) were detected in the examined tissues, eye and brain. Each element localizes at different biological structures, and each biological structure shows a slightly different spectrum of elements. Considering the fact that tissues were extensively washed with solvents during embedding into the epoxy resin, these elements seem to be chemically bound with ligands from proteins or other extracellular components. Zn is found generally in the nucleus of the cell among the examined tissues (Fig. 6.13). This feature provides a good counter staining, and it can be used as a reference for determining the distribution of other elements that show structure dependent localization. Cu was found to accumulate in the epithelium surface of the embryonic skin and cornea. Retinal pigment epithelium, together with melanocytes, showed enriched localization of elements. Basement membrane is an acellular, thin layer of extracellular matrix fibers that underlies the epithelium of the surface structures (cornea and skin). Notably we found bromine localized specifically to the basal membrane of the skin, cornea, and lens, and copper accumulated on the surface epithelium of the skin and cornea (Fig. 6.13).
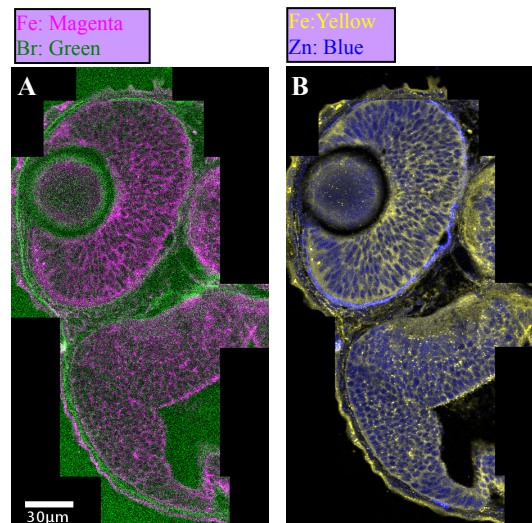
Fig. 6.13 Fluorescence images overlaid from sample type with As, Cd, Hg and Pb. Sample thickness was 5μm. Step size was 0.35μm. Dwell time was 100ms. Colour scales are independent.
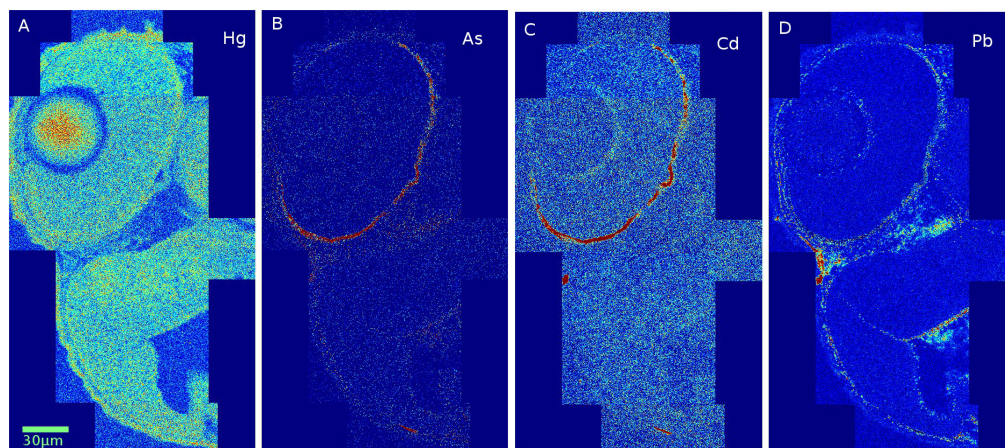
Fig. 6.14 Fluorescence images of the toxic elements from sample with As, Cd, Hg and Pb. Sample thickness was 5μm. Step size was 0.35μm. Dwell time was 100ms. Colour scales are

independent.

Tyrp1a/1b Gene knockout study

Genetic disorders have attracted worldwide attention in the biomedical research community. Genetic studies on zebrafish give links between the function of proteins and the corresponding manifestations in the phenotype[156–158]. The interaction of different genes and their development can be studied by altering the genetic expression in a controlled way. The fact that zebrafish embryos are transparent in visible light microscopy gives possibility to study them in more details during the development. Further studies can be made based on histology of thin slices cut from the specimens, showing for example localization of certain types of proteins. However, certain quantities remain elusive, such as the distribution of metal ions.

Metal ions have a large impact on biological processes via binding molecules together and acting as catalysts. Many metals are essential in small quantities, but harmful in large quantities, and the concentration of such metals in tissues must be between given limits to avoid deficiency and toxicity. Because of their high reactivity, metal ions may also pose a threat to tissues in the form of oxidative stress. Due to fast development times, and possibility to have a highly controlled environment, zebrafish is an ideal model organism for studying natural and genetically induced variations in metal distributions.

A model for oculocutanous albinism type 3 (OCA3) has been established in zebrafish[159]. OCA3 is a genetic disorder linked to the expression of single protein, Tyrosine related protein 1 (Tyrp1). The manifestations of OCA3 include reduced pigment production in the hair, eyes and the skin[160]. It is known that Tyrp1 has a role as an enzyme in the reaction pathway for eumelanin production, as well as in stabilizing tyrosine (TYR)[161]. Lack of Tyrp1 stops the eumelanin production after the first stage, leading to the fish without the desired pigmentary properties[162].

Melanin is a biopolymer that is produced by cells called melanocytes. Melanin comes packed in melanosomes that are small granules, typically less than 800 nm in size, and dark in color. Melanosomes are spread throughout tissues where darker color variations are needed. In the eye, melanosomes are accumulated in the retinal pigment epithelium (RPE) to absorb stray light coming into the eye. Melanin has been observed to have antioxidant properties in the RPE, by binding to reactive metal species[163]. This indicates that melanin has an important role in metal homeostasis in the eye.

We want to answer the following question: what is the impact of disrupted melanin production on the metal homeostasis in the zebrafish eye? We used high resolution x-ray fluorescence imaging to study the trace metal content in the eyes of two groups of zebrafish. One group was a control group with normal eye development, while the other group was a morpholino Tyrp1 knockdown group[164].
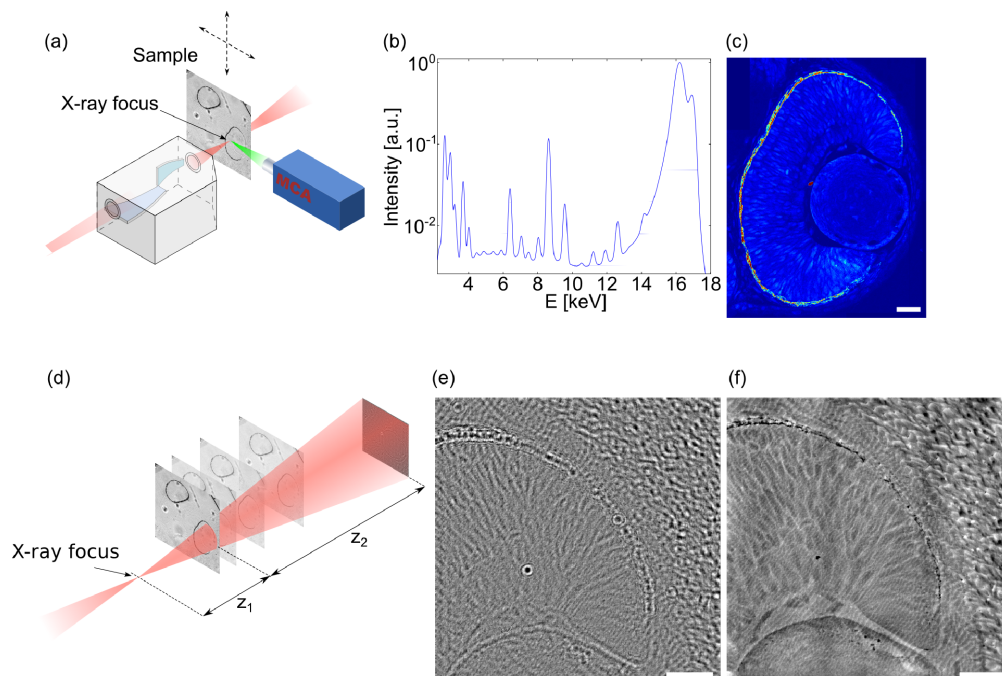
Fig. 6.15 Illustration of the experimental imaging techniques used. X-ray fluorescence imaging with focused x-rays (a). The fluorescence spectra recorded with energy resolving silicon drift diode detector showing characteristic fluorescence lines of elements in the sample (b). A map of Ca content in the sample (c) X-ray phase contrast imaging with the sample after the focus and image being recorded on a 2D detector downstream from the sample (d). An intensity image from a single sample to detector distance (e). A reconstructed phase map, based on using four different sample-to-detector distances (f). The scale bars in (c), (e) and (f) are 20 μm long.

The samples were imaged at the nanoimaging endstation ID22NI at ESRF. The x-ray beam with a focused spot well below 100 nm was used to characterize the elements in the sample by a raster scanning method (Fig. 6.15(a)). The X-rays excite the metal atoms in the sample. The atoms then emit fluorescent x-rays of specific energy depending on the atom. At each position in the sample a spectrum of photons was collected (Fig. 6.15(b)). The sample was raster scanned at chosen regions of interest, while collecting the spectra for each point. Medium resolution scans with a step size of 300 nm were used to cover the whole eye-region of the sample (Fig. 6.15(c)). A high resolution scan with 100 nm step size was then performed in chosen regions of interest that contained the RPE. Since the fluorescence imaging requires a high X-ray irradiation dose to the sample, the high and low resolution scans were done either on the two eyes on the opposite sides of the head or the same eye on adjacent slices. This avoided scanning the exact same region twice, and minimized the effects of irradiation damage.

The resulting spectra were treated on a pixel by pixel basis using the program PyMCA[107]. A calibration sample (NIST Standard reference material 1577b, bovine liver) containing known amounts of various elements was used to calibrate the analysis in order to get quantitative results. The analysis gave results in the quantification of element density, and mass fraction of each element. Due to the high Cl content in the EPON, a strong Cl peak is observed in the data. This high intensity peak overlaps with signal from P and S, making it impossible to quantify these elements properly. The variation of the sample thickness between the samples was taken into account by normalizing the results with the

mean scattered intensity.

Complementary to the fluorescence images, X-ray phase contrast images were obtained to show the structures in the sample. As described before, the sample was placed after the focus, and an image was recorded using a 2D detector placed further downstream (Fig. 6.15(d)). The free space propagation of X-rays forms a Fresnel diffraction pattern on the detector (Fig. 6.15(e)). By recording similar diffraction patterns at four different sample-to-detector distances, it was possible to retrieve the phase modulation induced by the sample on the X-ray wave (Fig. 6.15(f)). The reconstructed phase images show the variation of the projected electron density through the sample, and are very sensitive to small density variations in the microscopic sample.
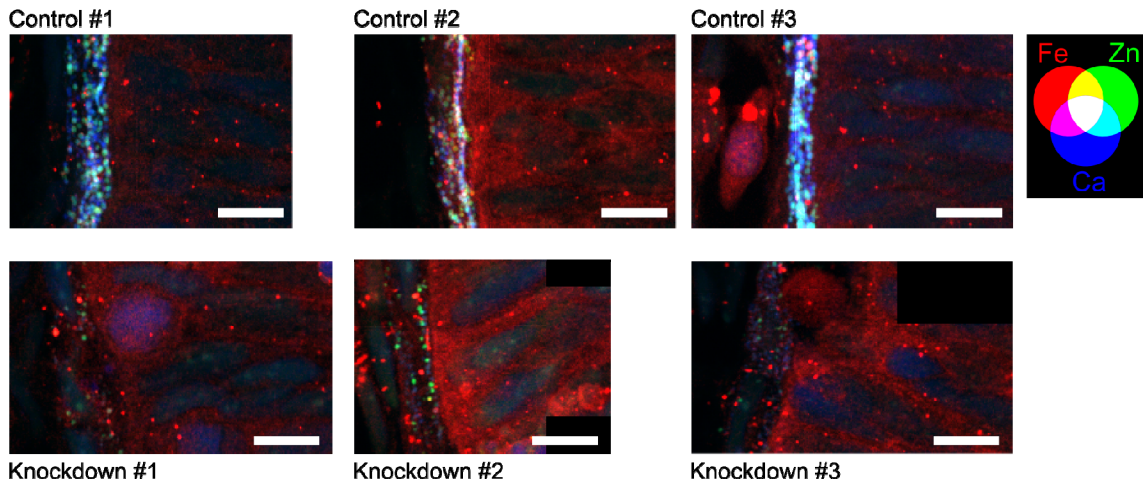
Fig. 6.16 High spatial resolution (step size 100 nm) trace element mapping for the RPE region of 2dpf zebrafish samples for Tyrp1a/b gene knock down studies. The top line shows the three studied fish in the control group, and the bottom row shows the three fish from the knockdown group. The elements Zn, Fe and Ni are shown in red, green and blue, respectively. The colour scales are equal for the two types of samples, showing the relative fractional concentrations. The scale bars are 5 μm.

High-resolution fluorescence images (100 nm step size) were taken for three animal specimens in the two groups. Each animal had a small region (roughly $10 \times 20 \ \mu m^2$) containing part of the RPE scanned. The results for the elements Fe, Zn, and Ca are displayed in Fig. 6.16. In the control group the RPE region shows number of particles with high intensity fluorescence from Ca and Zn, with varying compositions. The size of these particles is between 0.5 and 1 μm, by which they are very likely melanosomes that are present in the RPE. On the contrary, the RPE of the knockdown group lacks these high intensity spots, although some high intensity spots are present, especially those rich in Fe and Zn.

There is clear variation in the RPE even within the groups; the spots in the control group are mainly dominated by Ca and a mixture of Ca and Zn. In contrast, one of the controls displays markedly higher level of Fe in the overall retina and the RPE, and the spots contain also more Fe in this particular specimen. Likewise in the knockdown group the three fish present somewhat different overall levels of the elements.

Phase contrast nanolaminography in combination with 2D fluorescence imaging is able to resolve the structure and elemental distributions at subcellular level. For zebrafish

studies, we can explore the toxic effects from heavy metals and the gene-dependent development. Since the samples were prepared in thin sections, the 2D fluorescence allowed sufficient inspection of elemental distributions in different regions of the fish. In the future, the 3D fluorescence can be of interest to exam the intercellular elemental information intact.

6.5 Immune response of rat lungs to nanotube contamination – correlative nanolaminography

6.5.1 Background

Nanoparticles have become a big concern as environmental pollutants because of their increasing use in industry and daily life. Having high surface to volume ratio, high mobility, and easy penetration through membranes in biological systems, nanoparticles may have strong toxic effects even when the elemental composition of the particle is harmless to organism. In order to better understand the toxic effects of nanoparticles, the development of a capability to look directly into the pathways through which nanoparticles interact with cells and tissues is important. As airborne nanoparticles can easily enter animal lungs, deep to the alveolar level, ventilation is one of the key entry routes for nanoparticles[165–167].

Nanoparticles could be detected from the organic material if the elements of nanoparticles give off fluorescence signals with X-ray excitation. A combination of structural imaging with imaging of trace element distributions makes it possible to study the distribution of these nanoparticles inside the tissues. The distribution of exogeneous metals inside cell and tissue structures thus provides information on further understanding of toxic effects of nanoparticles, and can be used to study other forms of environmental pollutants as well.

Carbon nanotubes (CNT) have been shown to have highly toxic effects in lungs[168–170]. Electron microscopy studies have been used to localize CNTs inside cellular structures, but the field of view of such studies was limited[171]. With the multiple-scale approach of nanolaminography we are able to map the CNTs in a larger region, and then zoom in to select regions of interest.

An animal preparation protocol similar to that described in[171] was used (see Appendix) for preparing lung samples. Lung samples were embedded in paraffin and cut to slices of 30 µm in thickness. The nanotubes had irons as impurity (~7900 ppm), which can be used for fluorescence imaging to detect excess iron in the specimens.

6.5.2 Results and discussion

A lung specimen was first screened by a low resolution phase contrast imaging, and then a coarse resolution 2D fluorescence scan was made over an area of about 0.2×0.3 mm^2 with a step size of 1.8 µm. Areas of iron (hotspots) were found in the image (Fig. 6.17B), and we zoomed in one of these areas for high resolution imaging. A fluorescence data set with a step size of 500 nm, and a phase contrast data set a with pixel size of 60 nm were recorded in this ROI for laminographic 3D reconstruction.
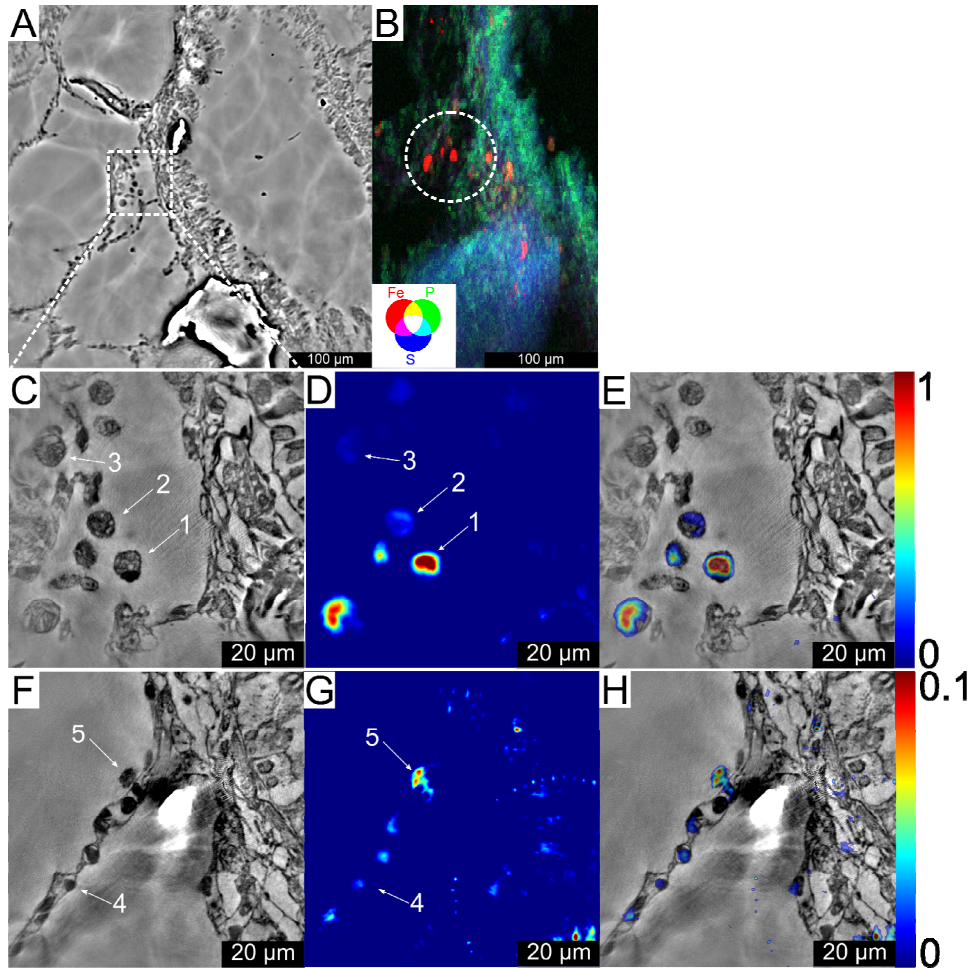
Fig. 6.17 Imaging of iron hotspots inside a lung specimen. (A) Slice from a low resolution phase contrast imaging volume. (B) Low resolution 2D fluorescence image of the specimen (the circle indicates the ROI that was chosen for higher resolution imaging). Phase contrast imaging (C), Fe fluorescence imaging (D) and correlated image of Fe and phase contrast (E) for slice 1 in the lung specimen. The arrows 1, 2, and 3 indicate alveolar macrophages. Phase contrast (F), Fe fluorescence imaging (G) and correlated image of Fe and phase contrast (H) for slice 2 in the lung specimen. Number 4 indicates a type 1 pneumocyte, while number 5 indicates an alveolar macrophage. Notice the factor of 10 difference in the fluorescence scale between parts (D,E) and (G,H).

The main results are shown in Fig. 6.17, where slices from the 3D volume are shown taken at two different positions in the lung specimen. In Fig. 6.17C, D, and E a single slice from the lung specimen is seen which contains an excess iron inside cellular structures. Based on the structural images, the size (about 12 µm), location (close to alveolar surface), and shape of the nucleus (single, round) indicate that the cells in question are alveolar macrophages (AM). The fact that excess iron is localized inside some of the AMs indicates the presence of nanotubes within the AMs, confirming the previous finding from electron microscopy that AMs are able to remove at least some of the nanotubes from the lungs[171]. Fig. 6.17E, F and G show part of the alveolar wall structure from the specimen. Hotspots of iron inside cellular structures of the wall are visible. From the shape of the cells, they can be identified as type-1 pneumocytes and one

AM. This iron has a concentration that is 10 times lower than that in the AMs of slice 1, but still higher than the surrounding tissues. Although the iron could be endogeneous, comparing the different cells in the lung wall shows that some of them have a much smaller quantity of iron than others. Therefore, from these images, it seems that nanotubes of small quantities could have entered some of the pneumocytes. Fig. 6.18 shows overlaid phase contrast and fluorescence contrast volume rendering.
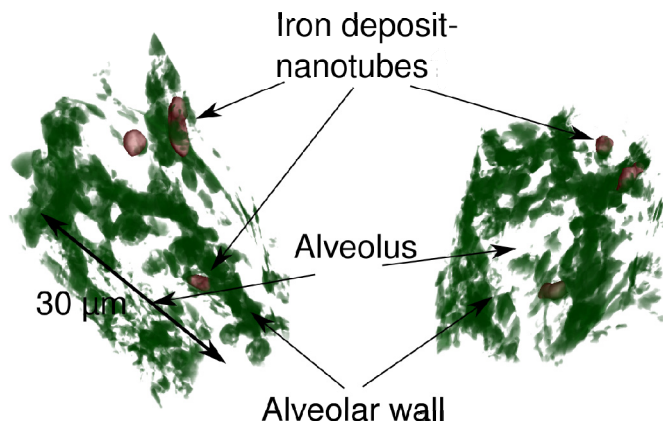
Fig. 6.18 3D rendering of the rat lung tissue sample. Green is phase contrast volume. Red is Fe fluorescence distribution.

Nanolaminography thus allowed us to focus on a region of the lung that was found to be highly different from the rest, based on the low resolution fluorescence scan. This approach brings benefits to biology and other subjects where the specimen's heterogeneity makes a single ROI unrepresentative of the entire specimen, and where the interesting regions may be far apart from each other. Correlative images allowed establishing correspondence between trace-metal excess content and the hosting cell types.

6.6 Conclusion and discussion

The ability to image large samples in 3D with high resolution has many payoffs in life sciences. The biggest advantage is the ability to do multiple scale imaging, focusing on the interesting regions after an initial low resolution scan. This is important because biological samples can be very heterogeneous in composition, and their features can be very dispersive from one part of the sample to the other.

In order to fully benefit from the possible advantages offered by laminography, online data analysis becomes necessary. To be able to image a sample in low resolution, and then to immediately look at the reconstructed images, is at the heart of being able to do multi scale imaging with good efficiency.

6.7 Appendix: Sample preparation protocols

6.7.1 SKOV3 Cells

The samples were made by cells included into epoxy resin and the thickness of the sample inside the frames is 80-100 microns (defined by the optical fibres used as spacers

between silicon nitride membranes). So cells are inside the glue between glasses (randomly distributed) and their dimension is around 10-20micron, depending on the cell size.

Here is sample preparation protocol for the cells:

Day 1: Plate SkOv3 cells on silicon nitride membrane (Silson).

Day 2:

1. Three times washes with 1ml of D-PBS pH 7.4;

2. Fix cells with 0.5 ml of 3.7% formaldehyde in D-PBS for 10 min at RT in the dark.

3. Three times washes with 1ml of D-PBS pH 7.4;

4. Block non specific sites with con 1 ml of blocking buffer (6% BSA in D-PBS, 0.22 mm filtered) for 1 h at RT;

5. Incubate with 0.5 ml of primary antibody (mouse monoclonal anti-HER2, Zymed Laboratories), 1:30 diluted in blocking buffer, for 1 h at RT; (without this step for control samples)

6. Three times washes with 1ml of D-PBS pH 7.4;

7. Incubate with 0.5 ml of secondary antibody goat anti-mouse IgG Qdot 605 conjugated (Molecular Probes by Invitrogen) 1:100 diluted in blocking buffer for 1 h at RT; (without this step for non Qdot samples)

8. Three times washes with 1ml of D-PBS pH 7.4;

9. Dehydrate in alcohol scale (1 ml):

    30% ethanol 2×5min

    50% ethanol 2×5min

    70% ethanol 2×5min

    85% ethanol 1×10min

    95% ethanol 1×10min

    100% ethanol 3×10min

10. Store o/n +4°C.

Day 3:

1. Substitute ethanol with resin:

    - ethanol 2: resin 1, 1×1h at RT;

    - ethanol 1: resin 1, 1×1h at RT;

    - ethanol 1: resin 2, 1×1h at RT;

2. Store o/n +4°C.

Day 4:

1. Substitute with absolute resin: resin 2×1h at RT;

2. Put 80 μm optic fibers on frames;

3. Cover with a second silicon nitride membrane;

4. Polymerize resin in oven (Poly/Bed 812-Araldite 502, Polysciences) at 60°C for 36h.

Note: Silicon nitride membrane have been sterilized by 20 min UV treatment under laminar flow hood.

6.7.2   Lung Tissue Sample preparation protocol

Animals. Male Sprague Dawley rats weighing 180-220 g were purchased from Charles River Laboratories (St Germain-sur-l'Arbresle, France). The rats were kept in a conventional animal facility and housed in positive-pressure air-conditioned units (228C, 60% relative humidity) on a 12:12 h light/dark cycle. The experimental protocol has been approved by the local ethical committee for animals in research.

MWCNT 3-10 (product number 636541) was purchased from Sigma -Aldrich (Lyon, France). These nanotubes were synthesized by Chemical Vapor Deposition method. Their diameter ranged from 3 to 10 nm, their wall thickness from 1 to 3 nm and their length from 0.1 to 10 μm. The purity is more than 90%). Catalyst used was Fe (data from the supplier).

Groups of 6 rats were anesthetized (0.5 mg/kg ketamine hydrochloride, 0.1 mg/kg atropine and 1 mg/kg xylazine) and were intratracheally instilled with MWCNT dispersed with bovine serum albumin (BSA) as previously described (Elgrabli et al. 2007) at a dose of 200 μg/rat in 150 μl. 7 days after the exposure, rats were sacrificed. Tissue specimens from the lung were fixed in 10% formaldehyde and processed routinely for embedding in paraffin. Tissue sections (5 μm) were cut and a part of them were stained with hematoxylin, eosin and saffron (HES) to examine general morphology of the lung and the presence of nanotubes. Slices of 40 μm thickness and 3×3 mm^2 cross section were cut from the paraffin block sections and were used to perform 3D imaging.

6.7.3   Zebrafish sample preparation protocol

1, Day one, 16:30 pm

> (1) In a water box, put in one male. Put a net in the water box and put one to two female zebrafish in the net.

> (2) Repeat to make eight boxes.

> (3) No light overnight.

2, Day two, 9:00 am (light on)

> (1) Take the male and put it to the net together with the female fish in the water.

> 10:00 am

> (2) Get the embryos. Then keep them in 29°C thermal place.

> 13:30 pm

> (3) Prepare Toxicity:

The original solutions: As_2O_3 80 mg/L; $Cdcl_2$ 15 mg/L; $PbCl_2$ 20 mg/L; MeHg 60 μg/L.

For samples which have two or three toxicants, we decreased the concentration to 10%.

For samples which have four toxicants, we decreased the concentration to 5%.

(4) Remove the dead, not fertilized, bad shaped embryos.

(5) Then separate the embryos by about 25 per container. Fill each container with different toxic solutions (for control samples, fill in water) and label them. (15:00 pm)

3, Day four, 9:00

(1) Take 10 embryos, three times rinse in salty water mixed with tricaine

Salty water: take 0.75 ml of 40 g/L sea salt water and add 500ml H_2O.

Tricaine: in stock, 400mg/10ml tricaine powder; Working: take 4.2ml from 400mg/10ml tricaine and mix to 100ml embryo culture.

(2) Fixing

Use Karnovsky's fixants: 0.4% PFA 400 μl + 1.25% GA 500 μl

Remove the water as much as possible and fill in 500 μl fixant/tube.

Keep the samples shaking on nutator at room temperature (RT) for two hours.

(3) Prepare EPON half full in embedding well, put the printed labels inside. Keep in 60°C for more than 2 hours or till solid.

(4) Rinsing to remove fixants by 2×5 mins PIPES buffer

(5) Dehydration

2×5 mins 50% Ethanol

2×5 mins 70% Ethanol

2×5 mins 95% Ethanol

4×5 mins 100% Ethanol

(6) Replace ethanol by EPON

2×5 mins Propylene oxide

(7) Propylene oxide 2 : EPON 1, 30mins RT

Propylene oxide 1 : EPON 2, 30mins RT

(8) EPON 30mins

(9) Put the fish in the well, keep in 60°C for more than 4 hours or over night.

4, Cut the samples by glass blade to 20 μm, 12 μm or 5 μm thick.

7 Conclusions

The aim of this work has been to enable and to improve computed laminography techniques using synchrotron radiation. This has consisted of optimizing imaging setups, techniques and data treatment methods for various purposes. Extending the techniques towards better resolution (both spatial and temporal) and towards new contrast modes in order to address new application fields has been the main driving factor of this work. During the course of the work we have used three different synchrotron beamlines for imaging experiments (ID15, ID19, and ID22, of the ESRF). By doing this we have been able to exploit the complementary characteristics of the different beamlines to cover a wide range of imaging modalities. We have thus enabled to pursue a wide variety of imaging applications, ranging from biology and medical studies to *in situ* and *ex situ* studies of materials and microelectronic devices.

The classification of the different results could be done based on the beamline used, on the achieved resolution, or on the application field (as was done in the previous two chapters). The main findings and conclusions on these applicative parts can be found at the end of the corresponding chapters of this work. From the methodological point of view, the advantages that are given by laminography over the existing tomography methods are important to be assessed. As computed laminography is directly competing with computed tomography, there has to be an advantage of laminography that justifies its use over tomography. Throughout this work we have developed the laminographic method for various purposes, and it turns out that in the different cases the advantages of laminography arise from different reasons.

Laminography is specialized to imaging of flat samples, but also CT can be used to study flat samples, albeit with some missing angles. As we saw in chapter 3, generally the image quality for the two methods is comparable if there is no physical limitation to what angular range can be achieved. Therefore one advantage of CL is in cases where the imaging geometry does not allow arbitrary angles between the sample and the beam. This is the case for most of the studies that were done at ID15 and ID19 using micron scale *in situ* imaging. A further advantage of CL in microimaging arises from the fact that large flat samples are mechanically more stable when lying flat on top of a rotation stage than when mounted vertically on top of a rotation stage.

In the nanoimaging experiments at ID22NI we did not approach *in situ* measurements, and the flat samples were generally so small that they could readily be mounted and kept stable on a vertical rotation axis and imaged with CT, thus removing many of the advantages present in laminography for larger samples. Here the advantages of laminography instead arise from reasons of optimizing the imaging contrast. One strong reason is that for the phase contrast imaging, laminography offers a similar contrast for each projection, allowing phase retrieval methods to work well. For CT scanning of the same sample, the phase contrast would change in a wide range in the different projections, making it difficult to do phase retrieval for all the projections using the same parameters for the phase retrieval algorithm (as regularization parameters in the phase retrieval have to be hand picked depending on the image contrast and noise levels). For fluorescence imaging the benefit of uniform contrast from laminography is even stronger. The strength of the fluorescence signal is approximately proportional to the length of the beam and sample intersection. When this path length varies (as in CT) it is difficult to

94

optimize the fluorescence detector position so that good signal would be recorded, while ensuring that the detector would saturate at no angle.

During the course of the work we found out following aspects that could still be improved for future developments:

(i) One issue is the sample alignment at the nanoimaging beamline. At this beamline the sample can be displaced only in one direction with respect to the rotation axis. This made it often time consuming to bring the required region of interest into the field of view. A method based on image correlation could be devised, where the actual ROI is brought into the field of view by moving the whole sample stage, and then the automatic method would put this field of view on the rotation axis by a combination of sample pushing movements and sample rotations. New beamline control macros need to be developed for this automation, but the method should be feasible for samples that exhibit sufficiently strong contrast.

(ii) Another issue related to sample alignment is the ability to have online data reconstruction for the phase contrast scans. This would be valuable from the point of view of knowing if the present scan has produced sufficiently good quality data, and in knowing in which direction to move the sample in cases where multiple ROIs are to be combined. Knowledge of the sample morphology would also help in the alignment of the ROI for fluorescence imaging. As the fluorescence imaging is by nature slower than the phase contrast imaging, a reasonably small ROI (or sampling density) has to be used. By knowing well the sample morphology around this ROI, we could possibly choose the ROI location better as well as limit the ROI size to the minimum.

(iii) One issue with the combination of multiple contrast methods is the automatic registration of the data. In the current work the data was aligned in the same orientation, and the scale factor between the data sets was known. Thus only the translation between the phase and fluorescence data set remained unresolved, and we proceeded to solve this by manually overlaying the volumes. While for small amount of data this technique is sufficient, we would benefit from an automated 3D registration method that can overlay volumes produced by different contrast methods.

(iv) The time requirements for laminographic fluorescence imaging are higher compared to similar imaging with CT. In CL we have to always obtain a full 3D volume, while in CT fluorescence we can obtain single slices by scanning a single line of the object. This is a fundamental limitation in the reconstruction, but arguably 3D data gives also a more complete picture of the sample than just a single slice. We expect that in the future with faster data acquisition (both due to improvements in detector technology and the X-ray sources) the 3D fluorescence imaging becomes more practical. The related issue of the sample dose is of concern for biological samples, but with the advent of cryogenic techniques for X-ray imaging we expect that this becomes less of a problem.

In summary: this work has pushed synchrotron radiation computed laminography towards becoming a routine technique for practical applications, and enabled correlative and nanoscale imaging for flat samples that would be otherwise difficult to image in 3D.

Bibliography

1. Blazek, J. & Gilbert, E. P. Application of small-angle X-ray and neutron scattering techniques to the characterisation of starch structure: A review. *Carbohydrate Polymers* **85**, 281–293 (2011).
2. Fenter, P. & Sturchio, N. C. Mineral–water interfacial structures revealed by synchrotron X-ray scattering. *Progress in Surface Science* **77**, 171–258 (2004).
3. Theyencheri, N. High brilliance small-angle X-ray scattering applied to soft matter. *Current Opinion in Colloid & Interface Science* **14**, 409–415 (2009).
4. Warren, B. E. & Physics *X-Ray Diffraction*. (Dover Publications: 1990).
5. Graham N., G. X-ray absorption spectroscopy of light elements in biological systems. *Current Opinion in Structural Biology* **3**, 780–784 (1993).
6. Richard D., D. X-ray fluorescence spectroscopy. *Nuclear Instruments and Methods in Physics Research* **208**, 655–658 (1983).
7. Hendee, W. R. X Rays in Medicine. *Physics Today* **48**, 51 (1995).
8. Hounsfield, G. N. Computerized transverse axial scanning (tomography): Part 1. Description of system. *Br J Radiol* **46**, 1016–1022 (1973).
9. Cecilia, A. *et al.* Characterisation of LSO:Tb scintillator films for high resolution X-ray imaging applications. *Nuclear Instruments and Methods in Physics Research Section A: Accelerators, Spectrometers, Detectors and Associated Equipment* **633, Supplement 1**, S292–S293 (2011).
10. Cha, B. K., Kim, J. Y., Kim, T. J., Sim, C. & Cho, G. Fabrication and imaging characterization of high sensitive CsI(Tl) and Gd2O2S(Tb) scintillator screens for X-ray imaging detectors. *Radiation Measurements* **45**, 742–745 (2010).
11. Kim, B.-J., Cho, G., Kyung Cha, B. & Kang, B. An X-ray imaging detector based on pixel structured scintillator. *Radiation Measurements* **42**, 1415–1418 (2007).
12. Olsen, U. L. *et al.* Structured scintillators for X-ray imaging with micrometre resolution. *Nuclear Instruments and Methods in Physics Research Section A: Accelerators, Spectrometers, Detectors and Associated Equipment* **607**, 141–144 (2009).
13. Philipp, H. T., Hromalik, M., Tate, M., Koerner, L. & Gruner, S. M. Pixel array detector for X-ray free electron laser experiments. *Nuclear Instruments and Methods in Physics Research Section A: Accelerators, Spectrometers, Detectors and Associated Equipment* **649**, 67–69 (2011).
14. Dinapoli, R. *et al.* A new family of pixel detectors for high frame rate X-ray applications. *Nuclear Instruments and Methods in Physics Research Section A: Accelerators, Spectrometers, Detectors and Associated Equipment* **617**, 384–386 (2010).
15. Toyokawa, H. *et al.* Single photon counting pixel detectors for synchrotron radiation experiments. *Nuclear Instruments and Methods in Physics Research Section A: Accelerators, Spectrometers, Detectors and Associated Equipment* **623**, 204–206 (2010).
16. Wilson, M. D. *et al.* Small pixel CZT detector for hard X-ray spectroscopy. *Nuclear Instruments and Methods in Physics Research Section A: Accelerators, Spectrometers, Detectors and Associated Equipment* **652**, 158–161 (2011).
17. Als-Nielsen, J. & McMorrow, D. *Elements of Modern X-ray Physics*. (Wiley: 2011).

18. Bordovitsyn, V. A., Bulenok, V. G. & Pozdeeva, T. O. On the coherence of synchrotron radiation. *Nuclear Instruments and Methods in Physics Research Section B: Beam Interactions with Materials and Atoms* **227**, 143–151 (2005).

19. Kohn, V., Snigireva, I. & Snigirev, A. Interferometric characterization of spatial coherence of high energy synchrotron X-rays. *Optics Communications* **198**, 293–309 (2001).

20. Cloetens, P., Barrett, R., Baruchel, J., Guigay, J. P. & Schlenker, M. Phase objects in synchrotron radiation hard x-ray imaging. *Journal of Physics D: Applied Physics* **29**, 133 (1996).

21. Momose, A., Takeda, T., Itai, Y. & Hirano, K. Phase–contrast X–ray computed tomography for observing biological soft tissues. *Nature Medicine* **2**, 473–475 (1996).

22. Snigirev, A., Snigireva, I., Kohn, V., Kuznetsov, S. & Schelokov, I. On the possibilities of x-ray phase contrast microimaging by coherent high-energy synchrotron radiation. *Review of Scientific Instruments* **66**, 5486–5492 (1995).

23. Di Michiel, M. *et al.* Fast microtomography using high energy synchrotron radiation. *Review of scientific instruments* **76**, 043702 (2005).

24. Bohic, S. *et al.* Synchrotron hard x-ray microprobe: Fluorescence imaging of single cells. *Applied Physics Letters* **78**, 3544 (2001).

25. Schaller, R. R. Moore's law: past, present and future. *Spectrum, IEEE* **34**, 52–59 (1997).

26. Henke, B., Gullikson, E. & Davis, J. C. X. X-ray interactions: photoabsorption, scattering, transmission, and reflection at E= 50-30,000 eV, Z= 1-92. *Atomic data and nuclear data tables* **54**, 181–342 (1993).

27. Hubbell, J. H. & Øverbø, I. Relativistic atomic form factors and photon coherent scattering cross sections. *Journal of Physical and Chemical Reference Data* **8**, 69 (1979).

28. Saloman, E., Hubbell, J. & Scofield, J. X-ray attenuation cross sections for energies 100 eV to 100 keV and elements Z= 1 to Z= 92. *Atomic Data and Nuclear Data Tables* **38**, 1–196 (1988).

29. James, R. W. *The Optical Principles of the Diffraction of X-rays*. (Ox Bow Press: 1982).

30. Paganin, D. M. *Coherent X-ray optics*. **6**, (Oxford University Press, USA: 2006).

31. Cloetens, P., Barrett, R., Baruchel, J., Guigay, J. P. & Schlenker, M. Phase objects in synchrotron radiation hard x-ray imaging. *Journal of Physics D: Applied Physics* **29**, 133 (1996).

32. Langer, M., Cloetens, P., Guigay, J. P. & Peyrin, F. Quantitative comparison of direct phase retrieval algorithms in in-line phase tomography. *Medical physics* **35**, 4556 (2008).

33. Guigay, J. Fourier transform analysis of Fresnel diffraction patterns and in-line holograms. *Optik* **49**, 121–125 (1977).

34. Paganin, D., Mayo, S., Gureyev, T. E., Miller, P. R. & Wilkins, S. W. Simultaneous phase and amplitude extraction from a single defocused image of a homogeneous object. *Journal of microscopy* **206**, 33–40 (2002).

35. Nugent, K., Gureyev, T., Cookson, D., Paganin, D. & Barnea, Z. Quantitative phase imaging using hard x rays. *Physical review letters* **77**, 2961–2964 (1996).

36. Guigay, J. P., Langer, M., Boistel, R. & Cloetens, P. Mixed transfer function and

transport of intensity approach for phase retrieval in the Fresnel region. *Optics letters* **32**, 1617–1619 (2007).

37. Neumaier, A. Solving ill-conditioned and singular linear systems: A tutorial on regularization. *Siam Review* 636–666 (1998).

38. Tertian, R. & Claisse, F. *Principles of quantitative X-ray fluorescence analysis*. (John Wiley & Sons: 1982).

39. Bohic, S. *et al.* Synchrotron hard x-ray microprobe: Fluorescence imaging of single cells. *Applied Physics Letters* **78**, 3544 (2001).

40. Paunesku, T., Vogt, S., Maser, J., Lai, B. & Woloschak, G. X-ray fluorescence microprobe imaging in biology and medicine. *Journal of cellular biochemistry* **99**, 1489–1502 (2006).

41. Hounsfield, G. N. Computerized transverse axial scanning (tomography): Part 1. Description of system. *Br J Radiol* **46**, 1016–1022 (1973).

42. Baruchel, J., Buffière, J. Y., Maire, E., Merle, P. & Peix, G. *X-ray tomography in material science*. (Hermes Science Paris: 2000).

43. Radon, J. Über die Bestimmung von Funktionen durch ihre Integralwerte langs gewisser Mannigfaltigkeiten. *Ber. Verh. S̈achs. Akad. Wiss. Leipzig, Math.-Nat. Kl* **69**, 262–277 (1917).

44. Kak, A. C. & Slaney, M. *Principles of Computerized Tomographic Imaging\Pp02071*. (Ieee: 1988).

45. Hsieh, J. *Computed tomography: principles, design, artifacts, and recent advances*. **114**, (Society of Photo Optical: 2003).

46. Ramachandran, G. & Lakshminarayanan, A. Three-dimensional reconstruction from radiographs and electron micrographs: application of convolutions instead of Fourier transforms. *PNAS* **68**, 2236–2240 (1971).

47. Moffat, A., Wright, P., Buffière, J. Y., Sinclair, I. & Spearing, S. M. Micromechanisms of damage in 0° splits in a [90/0] s composite material using synchrotron radiation computed tomography. *Scripta materialia* **59**, 1043–1046 (2008).

48. Ziedses des Plantes, B. G. Eine neue Methode zur Differenzierung in der Röntgenographie (Planigraphies). *Acta Radiologica* **13**, 182–192 (1932).

49. Zhou, J., Maisl, M., Reiter, H. & Arnold, W. Computed laminography for materials testing. *Applied physics letters* **68**, 3500 (1996).

50. Helfen, L. *et al.* High-resolution three-dimensional imaging of flat objects by synchrotron-radiation computed laminography. *Applied Physics Letters* **86**, 071915–071915 (2005).

51. Helfen, L., Baumbach, T., Cloetens, P. & Baruchel, J. Phase-contrast and holographic computed laminography. *Applied Physics Letters* **94**, 104103–104103 (2009).

52. Helfen, L. *et al.* On the implementation of computed laminography using synchrotron radiation. *Review of Scientific Instruments* **82**, 063702 (2011).

53. Hoshino, M., Uesugi, K., Takeuchi, A., Suzuki, Y. & Yagi, N. Development of an X-ray Micro-Laminography System at SPring-8. *AIP Conference Proceedings* **1365**, 250 (2011).

54. Hoshino, M., Uesugi, K., Takeuchi, A., Suzuki, Y. & Yagi, N. Development of x-ray laminography under an x-ray microscopic condition. *Review of Scientific Instruments* **82**, 073706 (2011).

55. Watanabe, N. *et al.* X-ray fluorescence micro-tomography and laminography using an x-ray scanning microscope. *Journal of Physics: Conference Series* **186**, 012022 (2009).

56. Dobbins, J. T. & Godfrey, D. J. Digital x-ray tomosynthesis: current state of the art and clinical potential. *Physics in Medicine and Biology* **48**, R65–R106 (2003).

57. Helfen, L. *et al.* Investigation of hybrid pixel detector arrays by synchrotron-radiation imaging. *Nuclear Instruments and Methods in Physics Research Section A: Accelerators, Spectrometers, Detectors and Associated Equipment* **563**, 163–166 (2006).

58. Helfen, L. *et al.* Synchrotron-radiation computed laminography for high-resolution three-dimensional imaging of flat devices. *physica status solidi (a)* **204**, 2760–2765 (2007).

59. Krug, K. *et al.* Relics in medieval altarpieces? Combining X-ray tomographic, laminographic and phase-contrast imaging to visualize thin organic objects in paintings. *Journal of Synchrotron Radiation* **15**, 55–61 (2007).

60. Moffat, A. J. *et al.* In situ synchrotron computed laminography of damage in carbon fibre–epoxy [90/0]s laminates. *Scripta Materialia* **62**, 97–100 (2010).

61. Matsuo, H., Iwata, A., Horiba, I. & Suzumura, N. Three-dimensional image reconstruction by digital tomo-synthesis using inverse filtering. *Medical Imaging, IEEE Transactions on* **12**, 307–313 (1993).

62. Di Michiel, M. *et al.* Fast microtomography using high energy synchrotron radiation. *Review of scientific instruments* **76**, 043702 (2005).

63. Weitkamp, T. *et al.* Status and evolution of the ESRF beamline ID19. *AIP Conference Proceedings* **1221**, 33 (2010).

64. Xu, F., Helfen, L., Baumbach, T. & Suhonen, H. Comparison of image quality in computed laminography and tomography. *Optics Express* **20**, 794–806 (2012).

65. Gordon, R., Bender, R. & Herman, G. T. Algebraic reconstruction techniques (ART) for three-dimensional electron microscopy and X-ray photography. *Journal of theoretical Biology* **29**, 471–481 (1970).

66. Wang, G. & Jiang, M. Ordered-subset simultaneous algebraic reconstruction techniques (OS-SART). *Journal of X-ray Science and Technology* **12**, 169–178 (2004).

67. Siltanen, S. *et al.* Statistical inversion for medical x-ray tomography with few radiographs: I. General theory. *Physics in medicine and biology* **48**, 1437 (2003).

68. Gordon, R., Bender, R. & Herman, G. T. Algebraic reconstruction techniques (ART) for three-dimensional electron microscopy and X-ray photography. *Journal of theoretical Biology* **29**, 471–481 (1970).

69. Mueller, K. FAST AND ACCURATE THREE-DIMENSIONAL RECONSTRUCTION FROM CONE-BEAM PROJECTION DATA USING ALGEBRAIC METHODS. (1998).

70. Andersen, A. H. Algebraic reconstruction in CT from limited views. *Medical Imaging, IEEE Transactions on* **8**, 50–55 (1989).

71. Herman, G. T. & Meyer, L. B. Algebraic reconstruction techniques can be made computationally efficient [positron emission tomography application]. *Medical Imaging, IEEE Transactions on* **12**, 600–609 (1993).

72. Herman, G. T. Image reconstruction from projections. *Real-Time Imaging* **1**, 3–18

(1995).

73. Andersen, A. & Kak, A. Simultaneous algebraic reconstruction technique (SART): a superior implementation of the ART algorithm. *Ultrasonic imaging* **6**, 81–94 (1984).

74. Jiang, M. & Wang, G. Convergence of the simultaneous algebraic reconstruction technique (SART). *Image Processing, IEEE Transactions on* **12**, 957–961 (2003).

75. Wang, G. & Jiang, M. Ordered-subset simultaneous algebraic reconstruction techniques (OS-SART). *Journal of X-ray Science and Technology* **12**, 169–178 (2004).

76. Zhou, J., Maisl, M., Reiter, H. & Arnold, W. Computed laminography for materials testing. *Applied physics letters* **68**, 3500 (1996).

77. Bleuet, P., Guillemaud, R., Desbat, L. & Magnin, I. An adapted fan volume sampling scheme for 3-D algebraic reconstruction in linear tomosynthesis. *Nuclear Science, IEEE Transactions on* **49**, 2366–2372 (2002).

78. Gonzalez, R. C. & Woods, R. E. Digital image processing. 1992. *Reading, Mass.: Addison-Wesley* **16**, 8 (1996).

79. Lewis, J. Fast normalized cross-correlation. *Vision Interface* **10**, 120–123 (1995).

80. Bing, P., Hui-min, X., Bo-qin, X. & Fu-long, D. Performance of sub-pixel registration algorithms in digital image correlation. *Measurement Science and Technology* **17**, 1615–1621 (2006).

81. Press, W. H., Flannery, B. P., Teukolsky, S. A., Vetterling, W. T. & others *Numerical recipes*. **547**, (Cambridge Univ Press: 1986).

82. Baumeister, W., Grimm, R. & Walz, J. Electron tomography of molecules and cells. *Trends in Cell Biology* **9**, 81–85 (1999).

83. Brunetti, A., Golosio, B. & Cesareo, R. A correction procedure for the self-absorption artifacts in x-ray Compton tomography. *X-Ray Spectrometry* **31**, 377–382 (2002).

84. Golosio, B. *et al.* Internal elemental microanalysis combining x-ray fluorescence, Compton and transmission tomography. *Journal of applied physics* **94**, 145 (2003).

85. Golosio, B. *et al.* Nondestructive three-dimensional elemental microanalysis by combined helical x-ray microtomographies. *Applied physics letters* **84**, 2199 (2004).

86. Performance — ESRF. at <http://www.esrf.eu/Accelerators/Performance>

87. Snigirev, A., Kohn, V., Snigireva, I. & Lengeler, B. A compound refractive lens for focusing high-energy X-rays. *Nature* **384**, 49–51 (1996).

88. Schroer, C. G. *et al.* Hard X-ray full field microscopy and magnifying microtomography using compound refractive lenses. *Nuclear Instruments and Methods in Physics Research Section A: Accelerators, Spectrometers, Detectors and Associated Equipment* **467**, 966–969 (2001).

89. Als-Nielsen, J. & McMorrow, D. *Elements of Modern X-ray Physics*. (Wiley: 2011).

90. Barrett, R. *et al.* Dynamically-figured mirror system for high-energy nanofocusing at the ESRF. *Proceedings of SPIE* **8139**, 813904 (2011).

91. KIRKPATRICK, P. & BAEZ, A. V. Formation of Optical Images by X-Rays. *J. Opt. Soc. Am.* **38**, 766–773 (1948).

92. Hignette, O., Cloetens, P., Rostaing, G., Bernard, P. & Morawe, C. Efficient sub 100 nm focusing of hard x rays. *Review of scientific instruments* **76**, 063709 (2005).

93. Warren, B. E. *X-Ray Diffraction*. (Courier Dover Publications: 1969).

94. Predecki, P. K. *et al. Advances in X-Ray Analysis*. (Springer: 1995).

95. Glassner, A. S. *An introduction to ray tracing*. (Morgan Kaufmann: 1989).

96. Ando, M. & Hosoya, S. *An attempt at x-ray phase-contrast microscopy*. (Inst. for Solid State Physics: 1971).

97. Momose, A. Demonstration of phase-contrast X-ray computed tomography using an X-ray interferometer. *Nuclear Instruments and Methods in Physics Research Section A: Accelerators, Spectrometers, Detectors and Associated Equipment* **352**, 622–628 (1995).

98. Zanette, I., Weitkamp, T., Donath, T., Rutishauser, S. & David, C. Two-dimensional x-ray grating interferometer. *Physical review letters* **105**, 248102 (2010).

99. Förster, E., Goetz, K. & Zaumseil, P. Double crystal diffractometry for the characterization of targets for laser fusion experiments. *Kristall und Technik* **15**, 937–945 (1980).

100. Ingal, V. & Beliaevskaya, E. X-ray plane-wave topography observation of the phase contrast from a non-crystalline object. *Journal of Physics D: Applied Physics* **28**, 2314 (1995).

101. Dilmanian, F. *et al.* Computed tomography of x-ray index of refraction using the diffraction enhanced imaging method. *Physics in medicine and biology* **45**, 933 (2000).

102. Cloetens, P. *et al.* Hard x-ray phase imaging using simple propagation of a coherent synchrotron radiation beam. *Journal of Physics D: Applied Physics* **32**, A145 (1999).

103. Cloetens, P. *et al.* Holotomography: Quantitative phase tomography with micrometer resolution using hard synchrotron radiation x rays. *Applied Physics Letters* **75**, 2912–2914 (1999).

104. Cloetens, P. *et al.* Quantitative phase contrast tomography using coherent synchrotron radiation. *Proceedings of SPIE* **4503**, 82 (2002).

105. Labiche, J.-C. *et al.* Invited article: The fast readout low noise camera as a versatile x-ray detector for time resolved dispersive extended x-ray absorption fine structure and diffraction studies of dynamic problems in materials science, chemistry, and catalysis. *Review of Scientific Instruments* **78**, 091301–091301–11 (2007).

106. Mokso, R., Cloetens, P., Maire, E., Ludwig, W. & Buffière, J. Y. Nanoscale zoom tomography with hard x rays using Kirkpatrick-Baez optics. *Applied physics letters* **90**, 144104 (2007).

107. Solé, V., Papillon, E., Cotte, M., Walter, P. & Susini, J. A multiplatform code for the analysis of energy-dispersive X-ray fluorescence spectra. *Spectrochimica Acta Part B: Atomic Spectroscopy* **62**, 63–68 (2007).

108. Requena, G. *et al.* Sub-micrometer synchrotron tomography of multiphase metals using Kirkpatrick–Baez optics. *Scripta Materialia* **61**, 760–763 (2009).

109. Sihn, S., Kim, R. Y., Kawabe, K. & Tsai, S. W. Experimental studies of thin-ply laminated composites. *Composites Science and Technology* **67**, 996–1008 (2007).

110. Yashiro, S., Okabe, T. & Takeda, N. Damage identification in a holed CFRP laminate using a chirped fiber Bragg grating sensor. *Composites science and technology* **67**, 286–295 (2007).

111. Emery, T. & Dulieu-Barton, J. M. Damage monitoring of composite materials using pulsed phase thermography and thermoelastic stress analysis. *Key Engineering Materials* **347**, 621–626 (2007).

112. Xu, F. *et al.* Synchrotron radiation computed laminography for polymer

composite failure studies. *Journal of Synchrotron Radiation* **17**, 222–226 (2010).

113. Labiche, J. C. *et al.* Invited article: The fast readout low noise camera as a versatile x-ray detector for time resolved dispersive extended x-ray absorption fine structure and diffraction studies of dynamic problems in materials science, chemistry, and catalysis. *Review of scientific instruments* **78**, 091301 (2007).

114. Martin, T. & Koch, A. Recent developments in X-ray imaging with micrometer spatial resolution. *Journal of synchrotron radiation* **13**, 180–194 (2006).

115. Faulkner, K. & Moores, B. Analysis of x-ray computed tomography images using the noise power spectrum and autocorrelation function. *Physics in Medicine and Biology* **29**, 1343 (1984).

116. Supanich, M. *et al.* Radiation dose reduction in time-resolved CT angiography using highly constrained back projection reconstruction. *Physics in Medicine and Biology* **54**, 4575–4593 (2009).

117. Wisnom, M. Size effects in the testing of fibre-composite materials. *Composites science and technology* **59**, 1937–1957 (1999).

118. Chen, C. & Knott, J. Effects of dispersoid particles on toughness of high-strength aluminium alloys. *Metal Science* **15**, 357–364 (1981).

119. Dumont, D., Deschamps, A. & Brechet, Y. A model for predicting fracture mode and toughness in 7000 series aluminium alloys. *Acta materialia* **52**, 2529–2540 (2004).

120. Zerbst, U., Heinimann, M., Donne, C. D. & Steglich, D. Fracture and damage mechanics modelling of thin-walled structures – An overview. *Engineering Fracture Mechanics* **76**, 5–43 (2009).

121. Bron, F., Besson, J. & Pineau, A. Ductile rupture in thin sheets of two grades of 2024 aluminum alloy. *Materials Science and Engineering: A* **380**, 356–364 (2004).

122. Bron, F. & Besson, J. Simulation of the ductile tearing for two grades of 2024 aluminum alloy thin sheets. *Engineering fracture mechanics* **73**, 1531–1552 (2006).

123. Moffat, A. J. *et al.* In situ synchrotron computed laminography of damage in carbon fibre-epoxy [90/0] s laminates. *Scripta Materialia* **62**, 97–100 (2010).

124. Morgeneyer, T. *et al.* Ductile crack initiation and propagation assessed via in situ synchrotron radiation-computed laminography. *Scripta Materialia* **65**, 1010–1013 (2011).

125. Morgeneyer, T., Starink, M. & Sinclair, I. Evolution of voids during ductile crack propagation in an aluminium alloy sheet toughness test studied by synchrotron radiation computed tomography. *Acta Materialia* **56**, 1671–1679 (2008).

126. Morgeneyer, T., Besson, J., Proudhon, H., Starink, M. & Sinclair, I. Experimental and numerical analysis of toughness anisotropy in AA2139 Al-alloy sheet. *Acta Materialia* **57**, 3902–3915 (2009).

127. Cannis, J. Green IC packaging. *Advanced Packaging* **8**, 33–38 (2001).

128. Zeng, K. & Tu, K. N. Six cases of reliability study of Pb-free solder joints in electronic packaging technology. *Materials Science and Engineering: R: Reports* **38**, 55–105 (2002).

129. Blech, I. Electromigration in thin aluminum films on titanium nitride. *Journal of Applied Physics* **47**, 1203–1208 (1976).

130. Tu, K. N. Recent advances on electromigration in very-large-scale-integration of interconnects. *Journal of Applied Physics* **94**, 5451–5473 (2003).

131.	Yeh, E. C. C., Choi, W., Tu, K., Elenius, P. & Balkan, H. Current-crowding-induced electromigration failure in flip chip solder joints. *Applied physics letters* **80**, 580 (2002).

132.	Lin, Y., Hu, Y., Tsai, C., Kao, C. & Tu, K. In situ observation of the void formation-and-propagation mechanism in solder joints under current-stressing. *Acta materialia* **53**, 2029–2035 (2005).

133.	Gan, H. & Tu, K. Polarity effect of electromigration on kinetics of intermetallic compound formation in Pb-free solder V-groove samples. *Journal of applied physics* **97**, 063514 (2005).

134.	Schaller, R. R. Moore's law: past, present and future. *Spectrum, IEEE* **34**, 52–59 (1997).

135.	Tu, K. Reliability challenges in 3D IC packaging technology. *Microelectronics Reliability* **51**, 517–523 (2011).

136.	Tian, T. *et al.* Rapid diagnosis of electromigration induced failure time of Pb-free flip chip solder joints by high resolution synchrotron radiation laminography. *Applied Physics Letters* **99**, 082114–082114 (2011).

137.	*Handbook of 3D Integration: Technology and Applications of 3D Integrated Circuits*. (2008).at <http://onlinelibrary.wiley.com/book/10.1002/9783527623051>

138.	Ponchut, C. *et al.* Photon-counting X-ray imaging at kilohertz frame rates. *Nuclear Instruments and Methods in Physics Research Section A: Accelerators, Spectrometers, Detectors and Associated Equipment* **576**, 109–112 (2007).

139.	Lau, J. H. *Flip chip technologies*. **1**, (McGraw-Hill: 1996).

140.	Lee, N. C. *Reflow soldering processes and troubleshooting: SMT, BGA, CSP, and flip chip technologies*. (Newnes: 2002).

141.	Merken, P., John, J., Zimmermann, L. & Van Hoof, C. Technology for very dense hybrid detector arrays using electroplated indium solderbumps. *IEEE Transactions on Advanced Packaging* **26**, 60–64 (2003).

142.	Fiederle, M. *et al.* Development of flip-chip bonding technology for (Cd, Zn) Te. *Nuclear Science Symposium Conference Record, 2003 IEEE* **1**, 232–236 (2003).

143.	Lak, M. *et al.* Phase contrast X-ray synchrotron imaging: opening access to fossil inclusions in opaque amber. *Microscopy and Microanalysis* **14**, 251–259 (2008).

144.	Pradel, A. *et al.* Skull and brain of a 300-million-year-old chimaeroid fish revealed by synchrotron holotomography. *Proceedings of the National Academy of Sciences* **106**, 5224 (2009).

145.	Tafforeau, P. *et al.* Applications of X-ray synchrotron microtomography for non-destructive 3D studies of paleontological specimens. *Applied Physics A: Materials Science & Processing* **83**, 195–202 (2006).

146.	Houssaye, A. *et al.* Three-dimensional pelvis and limb anatomy of the Cenomanian hind-limbed snake Eupodophis descouensi (Squamata, Ophidia) revealed by synchrotron-radiation computed laminography. *Journal of Vertebrate Paleontology* **31**, 2–7 (2011).

147.	Corezzi, S. *et al.* Synchrotron-based X-ray fluorescence imaging of human cells labeled with CdSe quantum dots. *Analytical biochemistry* **388**, 33–39 (2009).

148.	Bria, D. *et al.* Band structure and omnidirectional photonic band gap in lamellar structures with left-handed materials. *Physical Review E* **69**, 066613 (2004).

149.	Lousse, V. & Vigneron, J. P. Self-consistent photonic band structure of dielectric

superlattices containing nonlinear optical materials. *Physical Review E* **63**, 027602 (2001).

150. Vukusic, P. Photonic structures in biology. *Diffractive Optics and Micro-Optics* (2004).

151. Vigneron, J. P., Colomer, J. F., Vigneron, N. & Lousse, V. Natural layer-by-layer photonic structure in the squamae of Hoplia coerulea (Coleoptera). *Physical Review E* **72**, 061904 (2005).

152. Vukusic, P., Kelly, R. & Hooper, I. A biological sub-micron thickness optical broadband reflector characterized using both light and microwaves. *Journal of The Royal Society Interface* **6**, S193–S201 (2009).

153. Dooley, K. & Zon, L. I. Zebrafish: a model system for the study of human disease. *Current opinion in genetics & development* **10**, 252–256 (2000).

154. Driever, W., Stemple, D., Schier, A. & Solnica-Krezel, L. Zebrafish: genetic tools for studying vertebrate development. *Trends in Genetics* **10**, 152–159 (1994).

155. Korbas, M., Blechinger, S. R., Krone, P. H., Pickering, I. J. & George, G. N. Localizing organomercury uptake and accumulation in zebrafish larvae at the tissue and cellular level. *Proceedings of the National Academy of Sciences* **105**, 12108 (2008).

156. Briggs, J. P. The zebrafish: a new model organism for integrative physiology. *American Journal of Physiology-Regulatory, Integrative and Comparative Physiology* **282**, R3 (2002).

157. Fetcho, J. R. & Liu, K. S. Zebrafish as a Model System for Studying Neuronal Circuits and Behaviora. *Annals of the New York Academy of Sciences* **860**, 333–345 (1998).

158. Lieschke, G. J. & Currie, P. D. Animal models of human disease: zebrafish swim into view. *Nature Reviews Genetics* **8**, 353–367 (2007).

159. Braasch, I., Liedtke, D., Volff, J. N. & Schartl, M. Pigmentary function and evolution of tyrp1 gene duplicates in fish. *Pigment cell & melanoma research* **22**, 839–850 (2009).

160. TOYOFUKU, K. *et al.* Oculocutaneous albinism types 1 and 3 are ER retention diseases: mutation of tyrosinase or Tyrp1 can affect the processing of both mutant and wild-type proteins. *The FASEB Journal* **15**, 2149–2161 (2001).

161. Kobayashi, T. & Hearing, V. J. Direct interaction of tyrosinase with Tyrp1 to form heterodimeric complexes in vivo. *Journal of Cell Science* **120**, 4261–4268 (2007).

162. Marks, M. S. & Seabra, M. C. The melanosome: membrane dynamics in black and white. *Nature Reviews Molecular Cell Biology* **2**, 738–748 (2001).

163. Wang, Z., Dillon, J. & Gaillard, E. Antioxidant properties of melanin in retinal pigment epithelial cells. *Photochemistry and photobiology* **82**, 474–479 (2006).

164. Hernández, P. P. & Allende, M. L. Zebrafish (Danio rerio) as a model for studying the genetic basis of copper toxicity, deficiency, and metabolism. *The American journal of clinical nutrition* **88**, 835S (2008).

165. Borm, P. J. A. & Kreyling, W. Toxicological hazards of inhaled nanoparticles-potential implications for drug delivery. *Journal of Nanoscience and nanotechnology* **4**, 521–531 (2004).

166. Mills, N. L. *et al.* Do inhaled carbon nanoparticles translocate directly into the circulation in humans? *American journal of respiratory and critical care medicine*

173, 426 (2006).

167.   Mossman, B. T. *et al.* Mechanisms of action of inhaled fibers, particles and nanoparticles in lung and cardiovascular diseases. *Particle and Fibre Toxicology* **4**, 4 (2007).

168.   Lam, C. W., James, J. T., McCluskey, R. & Hunter, R. L. Pulmonary toxicity of single-wall carbon nanotubes in mice 7 and 90 days after intratracheal instillation. *Toxicological Sciences* **77**, 126 (2004).

169.   Muller, J. *et al.* Respiratory toxicity of multi-wall carbon nanotubes. *Toxicology and Applied Pharmacology* **207**, 221–231 (2005).

170.   Warheit, D. B. *et al.* Comparative pulmonary toxicity assessment of single-wall carbon nanotubes in rats. *Toxicological Sciences* **77**, 117 (2004).

171.   Elgrabli, D. *et al.* Biodistribution and clearance of instilled carbon nanotubes in rat lung. *Particle and Fibre Toxicology* **5**, 20 (2008).

Acknowledgements